

## University of Groningen

### Verification of a novel calorimeter concept for studies of charmonium states

Guliyev, Elmaddin

**IMPORTANT NOTE:** You are advised to consult the publisher's version (publisher's PDF) if you wish to cite from it. Please check the document version below.

*Document Version*

Publisher's PDF, also known as Version of record

*Publication date:*  
2011

[Link to publication in University of Groningen/UMCG research database](#)

*Citation for published version (APA):*

Guliyev, E. (2011). Verification of a novel calorimeter concept for studies of charmonium states University of Groningen: s.n.

**Copyright**

Other than for strictly personal use, it is not permitted to download or to forward/distribute the text or part of it without the consent of the author(s) and/or copyright holder(s), unless the work is under an open content license (like Creative Commons).

**Take-down policy**

If you believe that this document breaches copyright please contact us providing details, and we will remove access to the work immediately and investigate your claim.

*Downloaded from the University of Groningen/UMCG research database (Pure): <http://www.rug.nl/research/portal>. For technical reasons the number of authors shown on this cover page is limited to 10 maximum.*

RIJKSUNIVERSITEIT GRONINGEN

**Verification of a Novel Calorimeter Concept for  
Studies of Charmonium States**

Proefschrift

ter verkrijging van het doctoraat in de  
Wiskunde en Natuurwetenschappen  
aan de Rijksuniversiteit Groningen  
op gezag van de  
Rector Magnificus, dr. E. Sterken,  
in het openbaar te verdedigen op  
maandag 31 oktober 2011  
om 12:45 uur

door

Elmaddin Guliyev  
geboren op 4 mei 1981  
te Kurdamir, Azerbaijan

Promotor: Prof. dr. H. Löhner

Copromotor: Dr. M. Kavatsyuk

Beoordelingscommissie:  
Prof. dr. T. Johansson  
Prof. dr. N. Kalantar-Nayestanaki  
Prof. dr. W. Kühn

ISBN (printed version): 978-90-367-5102-5

ISBN (electronic version): 978-90-367-5099-8

**Verification of a Novel Calorimeter Concept for  
Studies of Charmonium States**

*To my uncle Yusif and daughter Deniz*

# Contents

<b>1. Introduction</b>	1
<b>2. Charmonium and exotic hadronic states</b>	5
2.1 Charmonium spectroscopy	6
2.2 Exotic hadronic states	8
2.3 Conclusion	9
<b>3. The PANDA detector</b>	11
3.1 Target spectrometer	11
3.2 Forward spectrometer	13
<b>4. The PANDA Electromagnetic Calorimeter</b>	15
4.1 Photon interactions with matter	16
4.2 Electromagnetic shower	17
4.3 PbWO <sub>4</sub> crystals as detector material	19
4.4 Large Area Avalanche Photo Diode	20
<b>5. Signal analysis for PANDA EMC</b>	23
5.1 General EMC readout scheme	23
5.1.1 Charge sensitive preamplifier	24
5.1.2 SADC readout	27
5.2 Data Acquisition	28
5.3 The feature extraction algorithm	29
<b>6. Performance studies</b>	35
6.1 Timing performance studies	35
6.1.1 Setup with LED light pulser	35
6.1.2 The results with LED light pulser	35
6.1.3 Time precision studies	37
6.2 Single crystal performance with Li ion beam	45
6.2.1 The experimental setup	45
6.2.2 Results of the ion beam	45
6.3 Measurements with the EMC prototype	50
6.3.1 Proto60 setup	50
6.3.2 Experiment at MAMI accelerator at Mainz	50
6.3.3 Readout electronics of Proto60	54
6.3.4 Cosmic muon calibration	54
6.3.5 The results with high-energy photons	57
6.4 GEANT simulation study of timing properties	63
6.5 Conclusion	67

<b>7. Implementation of feature-extraction algorithm in FPGA</b>	71
7.1 Introduction	71
7.2 Xilinx Spartan-3A development board	72
7.3 VHDL coding of the feature-extraction algorithm	72
7.4 Results obtained with the FPGA implementation	78
7.5 Conclusion	86
<b>8. Evaluation of PANDA EMC performance</b>	87
8.1 Single photon simulations	87
8.2 Simulations of the $h_c$ charmonium state	91
8.3 Conclusion	94
<b>Outlook and valorization</b>	95
<b>Bibliography</b>	97
<b>List of abbreviations</b>	101
<b>Summary</b>	103
<b>Samenvatting</b>	109
<b>Acknowledgment</b>	115

## 1. Introduction

The Standard Model (SM) of elementary particles and fields has been very successful in describing the fundamental constituents of matter and their interactions. According to the theory, the particles and force carriers are divided into three families as shown in Figure 1.1 [1].

The Standard Model has been extensively tested by various experiments at high energies and it has shown a remarkable predictive power which helped to observe yet undiscovered particles. However, it leaves us with many unsolved questions [2].

Recently the Large Hadron Collider (LHC) has started to run and it accelerates two beams of particles of the same kind (protons or ions up to Pb ions). The collision energy for protons will go up to 14 TeV.

LHC experiments at these high energies may help to understand some of the yet unsolved questions of the SM. In the Standard Model the origin of mass of the fundamental constituents of matter is explained by the Higgs mechanism: the whole space is filled with a ‘Higgs field’ and by interacting with this field, particles like leptons and quarks can acquire mass. The Higgs field is mediated by the Higgs boson [2, 3]. If such a particle exists, experiments at the LHC should be able to detect it and determine its properties. However, the Higgs mechanism does not explain, why some particles are heavy and others are light or extremely light, like the neutrinos. Nor does the Higgs mechanism explain how particles composed of light quarks can acquire a large mass.

According to the current theories, the Universe born from the Big Bang went through a stage during which matter existed as a sort of extremely hot, dense soup, called quark-gluon plasma (QGP) composed of the elementary building blocks of matter [3]. As the Universe cooled, the quarks became trapped into composite particles such as protons and neutrons. This phenomenon is called the confinement of quarks. The LHC is able to reproduce the QGP by colliding two beams of heavy ions (Pb ions). In the collisions, the temperature will exceed 100 000 times that of the center of the Sun.

Quantum chromodynamics (QCD) is a main component of the SM together with the electroweak theory [1, 2] and plays a key role in describing the strong interaction between quark and gluon constituents of matter.

In the past decades QCD has been extensively tested at high energies, where the strong coupling constant becomes small and perturbation theory applies. However, in the low-energy regime QCD starts to become non-perturbative. This situation requires the development of approximate theoretical models based on effective field theories which are rooted on the symmetries of QCD and are formulated in terms of the more relevant low-energy (i.e. hadronic) degrees of freedom. The exact formulation of an effective field theory depends on the energy range of interest.

In a more direct approach, based on first principles, the problem of solving non-perturbative QCD is treated by numerical calculations on a space-time lattice. However, computational limitations may lead to systematic errors that may require a comparison to results of an effective field theory. Such approaches need to be scrutinized by confrontation with precise experimental data e.g. on hadron masses, hadron decay rates and information

---

on the structure of hadrons. The Fermilab Lattice Collaboration [4] calculated the mass value of the hadrons and was able to reduce the uncertainty in the mass value from the 10% level to about 2% [5].

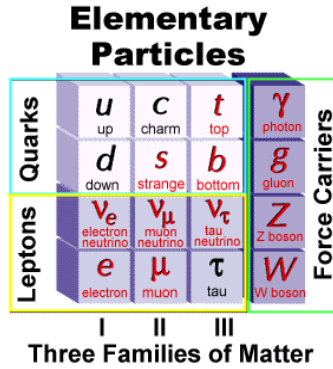


**Figure 1.1:** Elementary particles and the gauge bosons carrying the forces in the Standard Model.

The PANDA (antiProton ANnihilation at DArmstadt) experiment at the recently founded Facility for Antiproton and Ion Research (FAIR) in Darmstadt, Germany, will address the yet unresolved questions of nonperturbative QCD [6] with antiproton beams in the 1.5 – 15 GeV/c momentum range. The realization of this experiment to study QCD in the non-perturbative regime can therefore be considered as one of the most important events in recent years for hadron physics. One of the main purposes is to study hadrons containing a charm quark or consisting of a charm  $c$  and anti-charm  $\bar{c}$  quark. Such systems are particularly suited for comparisons with theory since the charm quark allows a non-relativistic approximation due to its large mass. The rich spectrum of charmonium ( $c\bar{c}$ ) states and the transitions between these states can be accessed directly in proton – antiproton annihilations. This is a great advantage over electron-positron annihilation experiments where only states with the photon quantum numbers can be accessed directly.

PANDA will be a unique experiment providing precise data for the understanding of hadronic bound states and resonances, the generation of exotic quark-gluon structures, and the importance of QCD symmetries. The physics program of the PANDA experiment focuses on charmonium spectroscopy and the search for hybrid states (i.e. mesons with an explicit gluon component) and glueballs (i.e. states consisting merely of gluons). Moreover, a large variety of other physics topics such as the study of hypernuclei, in particular those with two  $\Lambda$  hyperons, and measurements of the timelike form factor of the proton [6] will be addressed.

The study of the spectrum of charmonium states is an important research topic and a powerful tool for the understanding of the strong interaction [6]. Precision measurements of mass, width and decay branches of all charmonium states will provide information on the quark-confining potential and its spin dependence. Such a broad physics program of the PANDA experiment requires a multi-purpose detector with the important component of a high-resolution Electromagnetic Calorimeter (EMC) [7].

For high precision charmonium spectroscopy a low photon energy threshold is required.

One of the crucial issues is to optimize the energy resolution for studying narrow resonances with high precision. Another important requirement is the minimization of the time resolution to less than 1 ns for a clean event correlation and background suppression. These above-mentioned requirements demand a state-of-the-art development of the PANDA EMC front-end electronics and extensive performance studies.

This thesis will focus on research and development of the front-end electronics for the PANDA Electromagnetic Calorimeter.

- Chapter 2 gives a brief introduction to charmonium and exotic hadronic states. The physics program of the PANDA experiment is described.
- Chapter 3 provides an overview of the PANDA detector. The most important detector components are briefly discussed.
- The working principle and technical details of the PANDA EMC are explained in Chapter 4.
- Chapter 5 provides a description of the readout electronics for the PANDA EMC. It gives an overview of the employed preamplifiers, digitizer modules and the developed data acquisition and analysis scheme.
- In Chapter 6 the three different test measurements with LED light pulser, high-energy ion and photon beam and their analysis results are described.
- Chapter 7 assesses the implementation details of the online-analysis algorithm into a commercial XILINX Spartan FPGA development-board and SIS3302 Sampling ADC.
- Chapter 8 provides a simulation study for the PANDA EMC. Results will be discussed for single photons hitting a  $3 \times 3$  crystal array and for the decay of the  $h_c$  charmonium into  $7\gamma$  detected with the PANDA EMC.



## 2. Charmonium and exotic hadronic states

The PANDA experiment in the High Energy Storage Ring (HESR) at FAIR in Darmstadt will investigate proton - antiproton annihilations. The physics program of PANDA contains topics of high current interest like the study of charmonium states, the search for glueballs, hybrids, exotic mesons, and hypernuclei. Figure 2.1 compiles the focus topics of the PANDA experiment for the accessible antiproton momentum range from 1.5 – 15 GeV/c and interactions with protons from a hydrogen cluster jet or frozen pellet target.

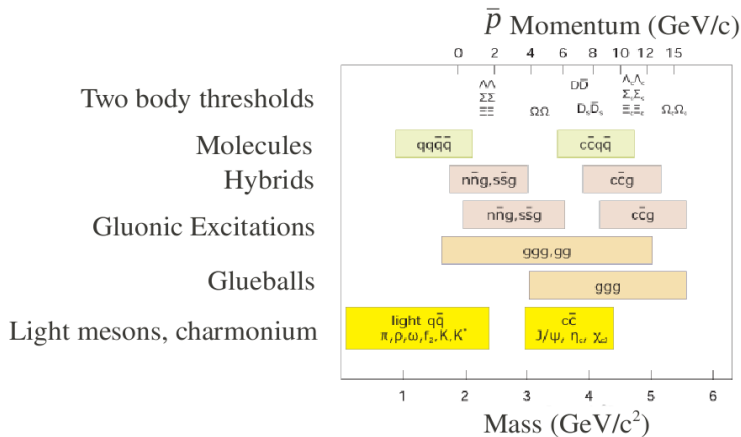


**Figure 2.1:** Mass range of hadrons that will be accessible by PANDA in the HESR with 1.5 to 15 GeV/c antiprotons. The upper scale indicates the corresponding antiproton momenta required in a fixed-target experiment. The accessible mass range will allow charmonium spectroscopy, the search for charmed hybrids and glueballs, the production of D-meson pairs, baryon pairs, and the production of hypernuclei [6].

The research goals of PANDA experiments aim at a clear understanding of QCD in the non-perturbative regime, which governs the formation and structure of hadrons. Here we will discuss two main topics of physics investigations in the PANDA experiment:

- Charmonium spectroscopy;
- Exotic hadronic states.

## 2.1 Charmonium spectroscopy

In 1974, the  $J/\Psi$  charmonium state was discovered in electron-positron collisions [8]. Subsequently, in electron-positron collisions also other states of the charmonium spectrum,  $\Psi'$  and  $\Psi(3770)$  resonances, were found and the quantum numbers  $J^{PC} = 1^-$  could be assigned, which are the quantum numbers of the photon. Charmonium states (see Figure 2.2) are bound states of a  $c$  and a  $\bar{c}$  quark and the  $J^{PC} = 1^-$  states can be formed in electron-positron collisions via the coupling to a virtual photon.

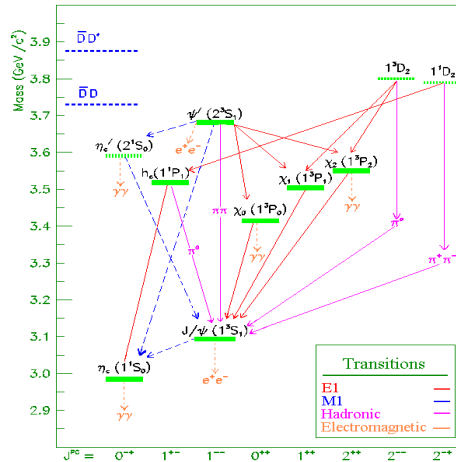


**Figure 2.2:** Spectrum of charmonium states [6] and transitions according to the given legend. Dashed-line transitions need further confirmation. The thresholds for  $D\bar{D}$  states are indicated.

Since their discovery, the charmonium states played a key role in understanding the nature of the strong interaction. The high mass ( $\approx 1.5$  GeV/c $^2$ ) of the charm quark allows to describe the charmonium bound states rather well in a non-relativistic potential model.

In  $e^+e^-$  collisions only states of charmonium with the quantum numbers of the photon can be directly formed. Meanwhile, a number of experiments (e.g. CLEO [9], BELLE [10], BES [11]) have produced charmonium states and rather well completed the charmonium spectrum (Figure 2.2). Charmonium can be produced e.g. in B-meson decays, two photon collisions, or  $p\bar{p}$  interactions. In  $p\bar{p}$  annihilations, all possible states of charmonium can be directly excited. Exploiting the precise knowledge of the beam momentum and the momentum scanning technique, the masses and widths of all charmonium states can be determined with excellent accuracy, limited by the very precise knowledge of the initial  $p\bar{p}$  state and not limited by the detector resolution, unlike the situation of charmonium production in  $e^+e^-$  collisions. The concept of the resonance scan is illustrated in Figure 2.3. The mass distribution that should be determined for the particle of interest is indicated by the green dotted curve. The nominal beam momentum is adjusted to several discrete values. Due to the finite momentum distribution of the beam, each of the nominal settings of the beam momentum excites a distribution of the center-of-mass energy  $E_{CM}$  as indicated by the

red dotted curves. The measured yield distribution for a given final state is the convolution of these two types of distributions, as indicated by the filled points along the blue solid line. The power of this method is clearly recognized by comparing measurements of the total decay width of the  $\chi_{c1}$ . Measurements from the Crystal Ball were only able to achieve a precision better than 3.8 MeV [12] and newer measurements from the BES collaboration achieved a precision of  $\Gamma = 1.39 \pm 0.40 \pm 0.26$  MeV [13]. In contrast, the E835 experiment was able to achieve uncertainties which are about one order of magnitude smaller resulting in a width  $\Gamma = 0.876 \pm 0.045 \pm 0.026$  MeV [14]. In the spectrum of charmonium states, shown in Figure 2.2, the  $c\bar{c}$  states below the  $D\bar{D}$  threshold are well established. The properties of the triplet-P states  $\chi_{c0}$ ,  $\chi_{c1}$  of and  $\chi_{c2}$  are studied well. However, the width of the charmonium ground state  $\eta_c$  is determined very poorly.

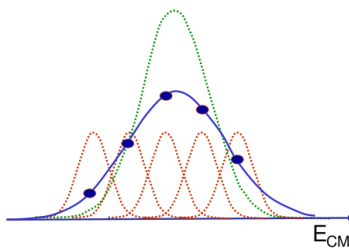


**Figure 2.3:** Scheme of the resonance scan technique [15]. The mass distribution that should be determined for the particle of interest is indicated by the green dotted curve. The nominal beam momentum is adjusted to several discrete values (red curves). The measured values (blue dots) need to be corrected for the beam resolution to obtain the true mass distribution.

The  $\eta_c'$  state, the first excitation of the  $\eta_c$  ground state, was discovered by BELLE [16] and was observed as an  $8\sigma$  deviation from the initial claims of the Crystal Ball [17]. Furthermore, different values of mass and width were established. However, the existing data on the mass only have a precision of 4 MeV and there is a 50% uncertainty in the width. These results are only marginally consistent with most predictions.

The singlet-P resonance ( $h_c$ ) is of extreme importance to determine the spin-dependent component of the  $q\bar{q}$  potential. For this state only two decay channels have been seen [18], but due to the narrow width of this state ( $\Gamma < 1$  MeV) only  $p\bar{p}$  formation experiments, as are proposed for PANDA, will allow measuring the width and systematically investigating the decay modes.

A rich spectrum of states may be expected in the energy region above the  $D\bar{D}$  threshold, but up to now, this region is poorly explored. Since 2003 a number of narrow states in this mass region have been observed by the BELLE [10], BABAR [19] and CLEO [9] experiments. Many basic parameters of these states have yet to be determined. Furthermore, precision measurements of all  $^1D$  and  $^3D$  states are required to distinguish between models that provide different interpretations of the nature of these states.

## 2.2 Exotic hadronic states

The confrontation of QCD-based theoretical predictions for exotic hadronic states with experimental data will provide a deeper understanding of the QCD dynamics. On the theory side, two different approaches are generally used: (i) lattice calculations (LQCD) [20], which attempt to solve non-perturbative QCD by numerical calculations, and (ii) effective field theories [6], either with quark-gluon or with hadronic degrees of freedom, which obey the symmetries of QCD and the existence of hierarchies of scales to provide predictions from effective Lagrangians. The exotic hadronic states are classified in three main categories:

Hybrid states: Such states differ from conventional mesons by an explicit gluon contribution. In the simplest scenario, the quantum numbers of such states may be found by adding the quantum numbers of a gluon to those of a simple  $q\bar{q}$  pair. This procedure creates e.g. for S-wave mesons eight lowest-lying hybrid states. Exotic charmonia are expected to exist in the 3–5 GeV/c<sup>2</sup> mass region. Predictions are provided mainly by calculations based on the bag model, flux tube model, constituent gluon model, and recently by LQCD [4, 5] calculations. These predictions qualitatively agree, and all models expect [21] that the lightest exotic state would be a  $J^{PC} = 1^+$  state. Predictions for the mass and the width estimate values around 4.3 GeV/c<sup>2</sup> and 20 MeV/c<sup>2</sup>, respectively. In addition, there are seven other hidden charmed hybrids [22] to be discovered. Therefore, the main goal would be to measure the whole pattern of charmonium exotic states. The PANDA program aims to search for charmonium-hybrid states in production experiments at the highest antiproton energy available ( $E_p = 15$  GeV,  $\sqrt{s} = 5.46$  GeV). Such measurements allow studying all possible channels, exotic and conventional. The next step would consist of formation measurements to scan the antiproton energy in small steps in the regions where promising hints of hybrids have been observed in the production phase.

Glueballs: Such states are composite particles consisting of gluons without any valence quarks. States of pure glue are possible since gluons carry color charge and can interact with each other according to QCD. LQCD calculations can provide predictions for the glueball mass spectrum (Figure 2.4). The glueballs are experimentally [23] hard to identify since they may mix with ordinary mesons. Therefore, glueballs with exotic quantum numbers (“odd-balls”) would be narrower and easier to be detected. LQCD predicts the presence of about fifteen glueballs in the mass range accessible to the PANDA experiment, some with exotic quantum numbers. The lightest odd-ball, with  $J^{PC} = 2^+$ , has been predicted with a mass of 4.3 GeV/c<sup>2</sup>.

Like charmonium hybrids, glueballs can either be formed directly in the  $p\bar{p}$ -annihilation process, or produced together with another particle. In both cases, the glueball decay into final states like  $\phi\phi$  or  $\phi\eta$  would be the most favorable decay below 3.6 GeV/c<sup>2</sup>, while  $J/\Psi\eta$  and  $J/\Psi\phi$  are the first choices for the more massive states. The indication for a tensor state around 2.2 GeV/c<sup>2</sup> was found in the experiment JETSET at LEAR [25]. The acquired statistics was not sufficient for the complementary reactions to be determined. Accordingly, the PANDA collaboration is planning to measure the  $p\bar{p} \rightarrow \phi\phi$  channel with two orders of magnitude better statistics than in the previous experiments.

Multiquark states: These are mesonic excitations of  $q\bar{q}$  states. These mesonic excitations are expected to be loosely bound, thus resulting in states having a large width. Nevertheless, in the vicinity of a strong threshold, this property may change, and states with a potentially large additional mesonic component can become narrower if they appear sub-threshold. This for example could be the case for the ( $a_0(980)$ ,  $f_0(975)$ ) system, which has a

large (may be dominant)  $K\bar{K}$  component in the wave function. In the case of the extremely narrow X(3872) state [26] the  $D\bar{D}$  threshold could have a similar impact on the mass of this state and could explain why it is not fitting into the conventional systematic of the charmonium spectrum.

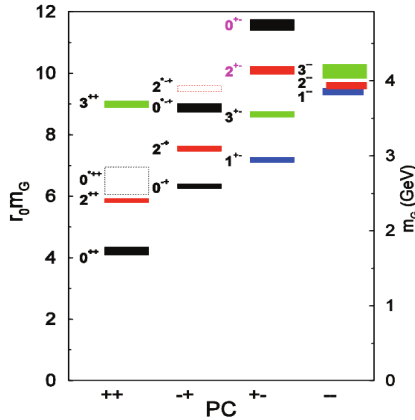


**Figure 2.4:** Predictions from LQCD calculations [24] for glueball masses with various PC quantum numbers. The masses are given in terms of the hadronic scale  $r_0$  on the left vertical axis and in terms of GeV on the right vertical axis.

## 2.3 Conclusion

In conclusion, the main scientific research topics of the PANDA experiment are charmonium spectroscopy, the search for exotic hadronic states, such as hybrid states, glueballs, and multiquark states. In order to underline the importance of an excellent electromagnetic calorimeter, we discuss as an example of hybrid states the charmonium hybrid state  $\tilde{h}_c$  [6]. The charmonium hybrid states are expected to decay mainly to charmonium final states, like in this reaction channel  $p\bar{p} \rightarrow \tilde{h}_c \eta \rightarrow J/\psi \pi^0 \pi^0 \eta$ . For this decay channel, the EMC is crucial to detect the complete final state because  $J/\psi$  decays electromagnetically, the  $\eta$  meson decays to three  $\pi^0$  which in turn decay each to two photons. In the search for glueballs, the experiment will study final states including  $\phi\phi$  or  $\phi\eta$  for states below 3.6 GeV/c<sup>2</sup> and  $J/\psi \eta$  and  $J/\psi\phi$  for higher-mass states. As an example of charmonium spectroscopy we mention here one of the charmonium states, the  $h_c$  state (see Figure 2.2). Precise information about this state will give more insight to determine the spin-dependent component of QCD bound states. One of the cleanest ways to identify the  $h_c$  state is to detect its decays into the  $7\gamma$  final state. This decay is discussed in Chapter 8, in order to evaluate the performance of the PANDA EMC.



### 3. The PANDA Detector

The physics program of the PANDA experiment demands a detector with challenging requirements, which are described as follows [27]:

The detector must

- cover  $4\pi$  solid angle;
- be capable of operation with high rates ( $2 \cdot 10^7$  annihilations/s);
- have a good particle identification and momentum resolution for  $\gamma$ , e,  $\mu$ ,  $\pi$ , K and p;
- have a good vertex reconstruction and excellent calorimetry.

The PANDA detector consists of two parts, namely the target spectrometer and the forward spectrometer. The combination of these two spectrometers provides the full angular coverage. The target spectrometer surrounds the interaction point and will be placed inside a 2 T solenoid magnet. The forward spectrometer will host a 2 T dipole magnet for tracking of charged particles under small angles with respect to the beam direction. A three-dimensional illustration of the PANDA detector including all sub-detectors is shown in Figure 3.1.

The most important sub-detector and infrastructure systems are discussed briefly in the following sections.

#### 3.1 Target Spectrometer

The target spectrometer is designed to detect particles with scattering angles larger than  $22^\circ$  and is placed inside the 2 T solenoidal field of a superconducting magnet. The most important sub-detector components of the target spectrometer are [28]:

**Target System:** The target will be brought into the beam-line by a vertical pipe structure as shown in Figure 3.1. There are two options for the target system: a cluster-jet target and a pellet target. Both target systems fulfill the requirement of a target thickness of roughly  $4 \cdot 10^{15}$  hydrogen atoms per  $\text{cm}^2$  in order to cope with the design luminosity of  $2 \cdot 10^{32} \text{ s}^{-1} \text{ cm}^{-2}$ . The cluster-jet target will be realized by a narrow jet of hydrogen-clusters with  $10^3 - 10^6$  hydrogen molecules per cluster. The pellet target would feature a stream of frozen hydrogen micro-spheres (“pellets”). Such type of pellet target is presently in use in the WASA experiment at the COoler SYnchrotron (COSY) accelerator at the Forschungszentrum Jülich, Germany [29].

**Solenoid Magnet:** The solenoid coil surrounds the electromagnetic calorimeter and the inner tracking detectors inside the calorimeter barrel. The solenoid produces a 2 T magnetic field in the target spectrometer. To achieve optimum tracking performance the magnetic field homogeneity is required to be better than  $\sim 1\%$  [31].

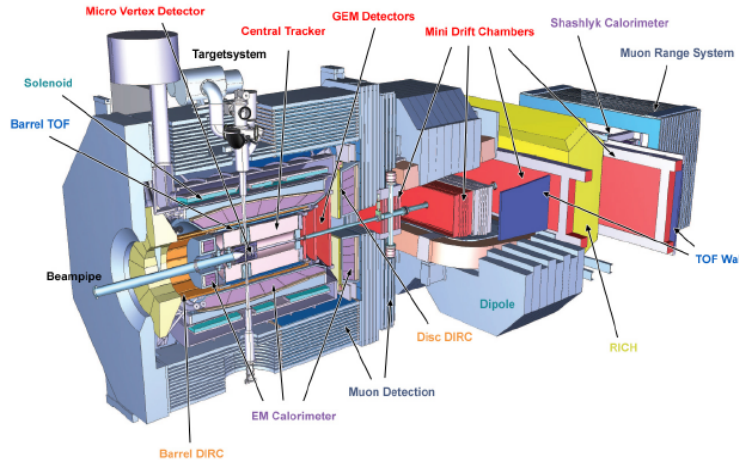


**Figure 3.1:** The PANDA detector including the sub-detector systems. The beam enters from the left. The length of the whole detector system is  $\sim 12$  m [30].

**Central Tracker and MVD:** The Micro-Vertex Detector (MVD) directly surrounds the interaction region with a radiation-hard silicon pixel and silicon-strip detector system. The current design of the MVD uses a four-layer barrel detector and eight additional layers perpendicular to the beam direction. It has a very good spatial resolution, which can improve the momentum resolution of the whole detector setup. The MVD is able to detect secondary vertices, such as D-meson decays, kaon and hyperon decays. The Central Tracker surrounds the MVD and has a good detection efficiency for secondary vertices which can occur outside the inner vertex detector [28]. The detectors foreseen for the Central Tracker of PANDA are either a Time Projection Chamber (TPC) or a Straw Tube Tracker (STT), depending on the prototype performances. The tracks of particles emitted below  $22^\circ$  in the forward direction will be covered by a Gas Electron Multiplier (GEM) detector layer: The high particle flux and the magnetic field forbid the employment of traditional drift chambers.

**Cherenkov Detector:** Particle identification (PID) is a very important aspect of the event reconstruction in order to obtain reliable physics information. PID requires the determination of velocity or energy loss in addition to the particle momentum. Above momenta of  $1\text{ GeV}/c$  the PID will be provided by Cherenkov Detectors. Below the Cherenkov threshold the tracking system will provide information on the energy loss of particles. The Cherenkov detector for the target spectrometer contains a barrel and a forward endcap component.

**ElectroMagnetic Calorimeter:** The crucial part of the PANDA detector is a ElectroMagnetic Calorimeter (EMC) [7], which is placed in the magnetic field and surrounds the interaction point. The PANDA EMC of the target spectrometer consists of three parts: the Barrel, Backward and Forward Endcap EMC. The PANDA EMC employs very dense scintillation crystals with a short radiation length. Lead tungstate ( $\text{PbWO}_4$  or PWO) crystals were already chosen for the CMS (Compact Muon Solenoid) [32] and the

ALICE (A Large Ion Collider Experiment) experiments at CERN [33]. In addition, the very fast scintillation decay time and the radiation-hardness, verified also at low temperatures [33], make the PWO crystals an excellent choice for the PANDA EMC. Recent developments of PWO-II crystals [34], as foreseen for the PANDA EMC, provide a two times higher light yield than achieved for CMS crystals [32]. The roughly 20 cm long crystals will be cooled down to a temperature of -25 °C in order to improve the light yield by a factor of four. To achieve the ultimate energy resolution, a temperature stability of 0.1 ° is required [34].

**Time Of Flight:** As already mentioned above, the Cherenkov detector will detect particles with momenta higher than 1 GeV/c. To identify the particles with lower momentum, a Time Of Flight (TOF) detector will be used providing a time resolution of about 100 ps. The TOF detector will be placed in front of the Barrel and the Forward Endcap EMC and consists of  $\sim 2 \times 2\text{cm}^2$  scintillation tiles coupled to silicon photomultipliers. Such a construction provides fast timing, position sensitivity, and easy handling of multiple-hit events, and allows minimizing the  $\gamma$  conversion in front of the EMC due to the low material budget.

**Muon detector:** Muons in the final state of interesting decay channels (e.g.  $J/\Psi$  decays, semi-leptonic decay of D mesons) and muons from background pion decays require proper tracking and separation. Therefore, the PANDA detector incorporates muon detectors, which will be installed in the outer layers of the detector setup and consist of the inner barrel and the outer barrel components.

## 3.2 Forward Spectrometer

The forward spectrometer is also equipped with a charged-particle tracking system, particle identification, calorimetry, and muon detector. Tracking of high-energy particles is done by a set of wire chambers. For the PID and the p/K and K/ $\pi$  separation a Cherenkov detector and a time-of-flight wall detector will be employed.

For the detection of photons and electrons with moderate energy resolution and high efficiency, the forward spectrometer will be equipped with a Shashlyk-type [7] calorimeter. The detection is based on lead-scintillator sandwiches read out with optical fibers which are coupled to photomultipliers. The last detection system of the forward spectrometer in downstream direction is a muon detector built as a multi-layer muon-range detection system.



## 4. The PANDA Electromagnetic Calorimeter

One of the important components of the PANDA spectrometer is the Electromagnetic Calorimeter (EMC). The PANDA detector consists of target and forward EMC. The target EMC surrounds the interaction point and provides an almost  $4\pi$  coverage. It consists of three parts - Barrel, Forward and Backward Endcaps. The EMC of the forward spectrometer will employ a Shashlyk type calorimeter. Figure 4.1 displays the main parts of the EMC in the target spectrometer on the left side and the forward-spectrometer EMC on the right side.

The EMC was designed to achieve an almost  $4\pi$  coverage for the detection of photons, electrons, and positrons in the target spectrometer. The forward spectrometer is located 7 m downstream of the target and will cover an area of about  $3 \text{ m}^2$ .

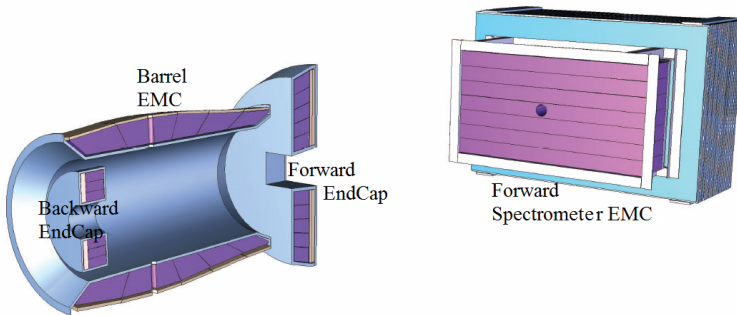


**Figure 4.1:** The layout of the PANDA Electromagnetic Calorimeters.

Due to the expected high annihilation rate of  $2 \cdot 10^7$  annihilations/s, a calorimeter with a fast signal response is required. Further, the calorimeter needs to cover a wide dynamic range for energy deposition in individual crystals from 10 MeV up to 10 GeV. This range is dictated by the physics program of the PANDA experiment, which aims at precision spectroscopy of charmonium states and of exotic hadrons in the charmonium region. These demanding requirements impose the deployment of fast and high-density crystals such as lead-tungstate ( $\text{PbWO}_4$  or briefly PWO) inorganic scintillator crystals as detector material in the target EMC [7]. The scintillation light from these crystals will be measured by Large-Area Avalanche Photo Diodes (LAAPDs) and Vacuum Photo Triodes (VPT) as photo sensors and specially designed front-end electronics. In comparison to the LAAPDs the VPTs have lower gain and lower quantum efficiency. However, the VPTs are more radiation hard, have lower dark current and lower capacitance, which provides advantages for operation in a high hit-rate environment. Therefore, VPTs will be used in the regions where high hit rates are expected, i.e. in the most-forward region of the target EMC.

The target electromagnetic calorimeter of PANDA will consist of about 17000 PWO

crystals. The optimization of the front-end electronics is the focus of this thesis and will be described in the following chapters.

This chapter will review the physics of photon interactions with matter, the properties of the detector material and the characteristics of the LAAPD photo sensors which were used for all the measurements described and evaluated in this thesis. The readout chain will employ the same preamplifiers for the VPTs and the LAAPDs, which results in the same waveform for both types of photo sensors. Therefore, the obtained results with LAAPDs can be applied as well to evaluate the performance of the VPTs.

## 4.1 Photon interactions with matter

When a high-energy photon interacts with matter it likely produces a pair of an electron and a positron with still high energies. The generated electron and positron interact with matter and can cause bremsstrahlung [35] of considerable energy. The bremsstrahlung photon again gives rise to electron-positron pair production. Thus, a cascade of many electromagnetic particles with gradually lower energy will build up until the energy of the particles falls below the threshold for pair production. The remaining energy is dissipated by excitation and ionization. Figure 4.2 shows the cross section of different processes of photons and electrons as a function of their energy. The main physics of photon interaction with matter is described briefly below:

**Bremsstrahlung:** The principal source of energy loss of high-energy electrons or positrons passing through matter is bremsstrahlung resulting from Coulomb interactions with the electric field of atomic nuclei. The energy spectrum of the radiated photons behaves like  $1/E$  – where  $E$  is the energy of the bremsstrahlung photon. In the limit of very hard bremsstrahlung the entire kinetic energy of an electron can be emitted as a photon but this is a very rare case. In general, the bremsstrahlung photons carry only a small fraction of the kinetic energy of the charged particle. The direction of the initial particle changes slightly during such a process. The energy loss of an electron by bremsstrahlung is approximately proportional to the electron kinetic energy. The interaction of photons with matter can be explained by three basic processes – the photoelectric effect, Compton scattering, and pair production [35, 36].

**Photoelectric effect:** At low energies, an atom absorbs a photon and emits an inner-shell electron. The atom is put into an excited state by this process and will return into its ground state by emission of Auger electrons or X-rays. The cross section for the photoelectric effect depends strongly on the electron density and thus on the  $Z$  of the absorber material.

**Compton scattering:** When a photon undergoes Compton scattering it transfers part of its energy and momentum to an atomic electron that is freed into an unbound state. The process will result in a free electron and a scattered photon. For most absorber materials, Compton scattering is by far the most likely process for photons with energies between a few hundred keV and a few MeV.

**Pair production:** Photons with energy of at least twice the electron rest mass (1.02 MeV) can produce an electron-positron pair in the Coulomb field of an atomic nucleus or an electron. The cross section for this process rises with energy and reaches an asymptotic value at very high energies ( $> 1$  GeV). For energies above a few MeV (depending on the absorber material), pair production becomes the dominant photon interaction process.

**Radiation length:** The appropriate length scale to describe the development of an electromagnetic shower is the radiation length  $X_0$ . One radiation length is the mean distance over which the electron energy is reduced to  $1/e$  of its original value due to radiation loss

only. The mean free path of a high energy photon for pair production is 9/7 of a radiation length [35]. The radiation length is, therefore, a characteristic distance for the two processes that shape the electromagnetic cascade. The radiation length in a material is usually measured in g/cm<sup>2</sup>. It can be approximated by [35]:

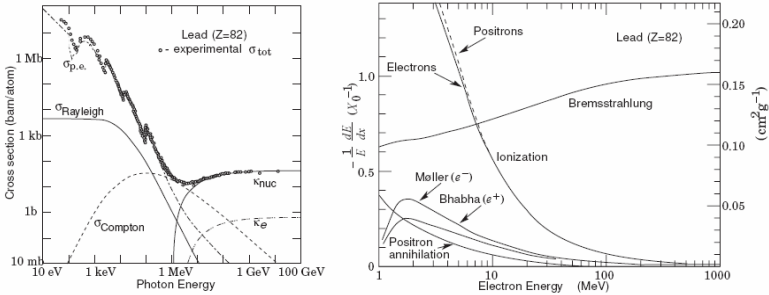


**Figure 4.2:** Left: Photon cross section as a function of the photon energy in lead. Right: Fractional energy loss of electrons per radiation length as a function of energy [37].

$$X_0 = \frac{A \cdot 716.4 \text{ g} \cdot \text{cm}^{-2}}{Z \cdot (Z + 1) \cdot \ln(287/\sqrt{Z})} \quad (4.1)$$

where  $A$  is the atomic mass and  $Z$  is the atomic number of the material. To measure the energy of an incoming particle the calorimeter must be thick enough in terms of radiation lengths to fully contain the electromagnetic shower. To achieve this for the PANDA EMC, the high- $Z$ , high-density lead-tungstate material was chosen with a crystal depth (i.e. length) of at least 22 radiation lengths [7].

The following equation describes the amount of energy loss by bremsstrahlung:

$$-\frac{dE}{dx} = \frac{E}{X_0} \quad (4.2)$$

where  $dE/dx$  is the specific energy loss,  $E$  is the energy of the particle, and  $X_0$  is the radiation length given in (4.1). On the contrary, charged particles in the electromagnetic shower loose energy continuously by ionizing the traversed material.

## 4.2 Electromagnetic Shower

If the incoming photons have high energy, it is most likely that pair production occurs. In this process, the photon converts into an electron-positron pair. The electron and the positron undergo bremsstrahlung and are therefore deflected. Subsequently, a photon is emitted which again can produce an electron-positron pair if the energy is high enough. The shower process may spread in all directions, but is mainly focused in the longitudinal direction because of the high incoming longitudinal momentum. Figure 4.3 illustrates the development of such a cascade as a function of the radiation length. The shower continues

until the critical energy  $E_c$  is reached.  $E_c$  is the electron energy at which the cross section of bremsstrahlung becomes equal to that of pure ionization [36]. Therefore, the shower development is stopped and no further secondary particles are produced. The equation below shows that the critical energy depends on the atomic number  $Z$  of the detector material:

$$E_c \approx \frac{550\text{MeV}}{Z} \quad (4.3)$$

It is obvious that a material with a high  $Z$  value corresponds to a low critical energy and is thus more sensitive to the full energy deposition.

In this context, the Moliere radius should also be mentioned. It is a characteristic constant of a calorimeter material and is related to the radiation length:

$$R_M = 0.0265 \cdot X_0(Z + 1.2) \quad (4.4)$$

The Moliere radius  $R_M$  is a good scaling variable for describing the transverse dimension of an electromagnetic shower.

**Fluctuations:** The number of electrons and positrons in a shower produced by a photon with a given energy fluctuates statistically. Since the total ionization signal is proportional to the number of charged particles, the reconstructed energy fluctuates in the same way. The relative width of the distribution is equal to  $\frac{\sqrt{n}}{n} = \frac{1}{\sqrt{n}}$  where  $n$  is the number of charged particles. Therefore, the relative precision of the energy measurement with a calorimeter can be expressed as

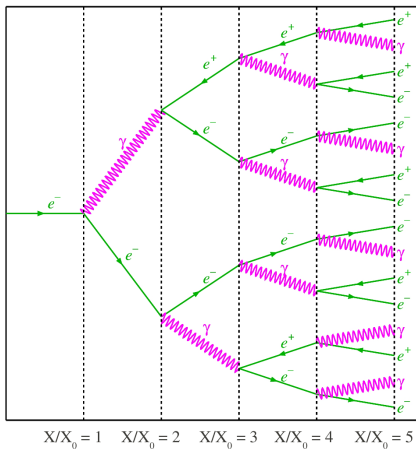


**Figure 4.3:** Illustration of an electromagnetic shower [38].

$$\frac{\sigma_E}{E} = \frac{b}{\sqrt{E}} \quad (4.5)$$

One can see from this formula that the relative energy resolution of a calorimeter improves with the energy. Therefore, calorimeters are very attractive instruments for high-energy particle physics experiments.

The energy resolution of a calorimeter can be expressed in terms of the parameter  $b$ , which is a stochastic term related to intrinsic shower fluctuations and photo-electron (phe) statistics. In practice, equation 4.5 has to be extended by adding a noise term  $c$  and a constant term  $a$  to account for instrumental effects independent of the shower development like non-uniform absorber thickness. This leads to [37]:

$$\frac{\sigma_E}{E} = a + \frac{b}{\sqrt{E}} + \frac{c}{E} \quad (4.6)$$

At moderately high energies, the noise term  $c$  becomes small and can be safely neglected. For very high energies, the stochastic (sampling) term becomes small and the resolution of the calorimeter is determined by instrumental effects represented by the parameter  $a$ .

### 4.3 PbWO<sub>4</sub> crystals as detector material

To detect high-energy photons, the EMC detector material should have the following properties. A high density and a short radiation length are required to allow for small size crystals and a compact EMC; a high light yield is needed to obtain the best energy resolution. Therefore, to detect high-energy photons, electrons and positrons with high energy-, time- and position-resolutions, the PANDA EMC will employ lead-tungstate crystals PbWO<sub>4</sub> (PWO) [39]. PWO material is being used in the electromagnetic calorimeters of the CMS (ECAL) [32] and ALICE (PHOS) [33] experiments at CERN. However, in the meantime, through continued development efforts the PWO material has been improved to achieve the PWO-II material for the PANDA EMC. PWO-II has two times higher light yield [7] compared with PWO applied in the CMS experiment.

One of the key features of PWO is the fast scintillation process with a short decay time. Due to the short decay time, the PWO material is advantageous at high event rates as they are expected in PANDA at high antiproton annihilation rates. The short decay time is useful to get precise timing information as well. The PWO material has a short radiation length of about 0.89 cm [7] and the Moliere radius is 2.2 cm [7].

The main properties of PWO-II crystals are presented in table 4.1. The light luminescence yield compared to NaI(Tl) is very low, only about 1%. However, cooling PWO down to -25 °C improves the light yield by a factor 4 [7]. Full-size 200 mm long crystals deliver a light yield of 17-20 phe/MeV at 18 °C measured with photomultiplier [7] with bi-alkali photocathode (quantum efficiency ~20%). Figure 4.4 shows a photograph of lead-tungstate crystals used in the test measurements.



**Figure 4.4:** Two samples of PWO-II crystals with dimensions ca.  $20 \times 20 \times 200$  mm $^3$ .

Parameter	PbWO <sub>4</sub>
Density	8.28 g/cm <sup>3</sup>
Radiation length	0.89 cm
Moliere radius	2 cm
Luminescence peak wavelength	420 nm
Decay time	5 - 15 ns
Relative light output (NaI(Tl))	0.6% at RT 2.5% at -25 °C

**Table 4.1:** Main properties of PbWO<sub>4</sub> (PWO-II) [7].

#### 4.4 Large-Area Avalanche Photo Diode

The operation of the electromagnetic calorimeter in the magnetic field of the target-spectrometer solenoid excludes the use of photomultiplier tubes for the readout of the PWO crystals. For that reason, a photo sensor is required which is insensitive to magnetic fields. Due to the low light yield of lead-tungstate the photo sensor should have internal gain. Large Area silicon Avalanche Photo Diodes (LAAPDs) satisfy these requirements and are therefore an ideal solution for the PANDA calorimeter.

**Photo diode operation:** When a photon enters a photo diode, an electron-hole pair is generated, if the energy of the incident photon is higher than the band-gap energy. The band-gap of silicon is 1.12 eV at room temperature and silicon becomes sensitive to wavelengths shorter than 1100 nm. Two terms, needed to describe this sensitivity, are called the photo-sensitivity  $S$  and the quantum efficiency  $QE$ .  $S$  is given by the photo current divided by the incident radiant power and  $QE$  is the ratio of generated electron-hole pairs over the number

of incident photons (%). The following equation connects these two terms:

$$QE = \frac{S \cdot 1240}{\lambda} \cdot 100 [\%] \quad (4.7)$$

where  $\lambda$  is the wavelength of the incoming photon. Figure 4.5 shows a schematic view of a silicon APD with reverse-bias structure. The photons enter the APD via the  $p^{++}$  layer. They are absorbed in the  $p^+$  layer where the electron-hole pairs are generated. Due to the electric field, the electrons drift towards the  $n^{++}$  side and the holes towards the  $p^{++}$  side. If the electric field is sufficiently high, these charge carriers will likely collide with the crystal lattice where ionization takes place. Due to the ionization process, new electron-hole pairs are generated. These electron-hole pairs again create additional pairs. A chain reaction occurs which is called avalanche multiplication. The avalanche multiplication starts when the electric field reaches a strength of about  $2 \cdot 10^5$  V/cm. The charge collection of all the produced electrons takes place in the  $n^{++}$  region. A passivated layer made of silicon nitride ( $Si_3N_4$ ) is mounted in front of the  $p^{++}$  layer to reduce the decrease of quantum efficiency caused by reflection losses.

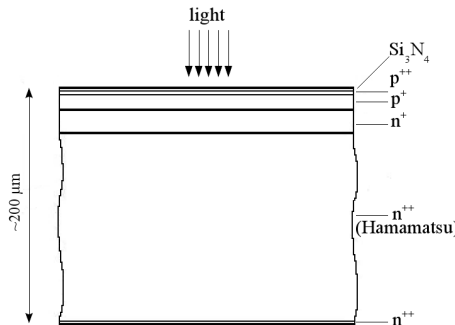


**Figure 4.5:** Schematic view of an APD with reverse-bias structure [7].

The internal current gain of an APD becomes higher, when the applied reverse voltage increases. There are various expressions for the multiplication factor  $M$  of an APD. An informative equation is given below [40]:

$$M = \frac{1}{1 - \int_0^L \alpha(x) dx} \quad (4.8)$$

where  $L$  is the space charge boundary for electrons and  $\alpha$  is the multiplication coefficient for electrons. The  $\alpha$  has a strong dependence on the applied field strength, doping profile and temperature.

An important noise factor is the excess noise, which describes the statistical noise that is inherent with the stochastic multiplication process. It is denoted by  $F(M)$  and can be expressed as [40]:

$$F = kM + \left(2 - \frac{1}{M}\right) \cdot (1 - k) \quad (4.9)$$

where  $k$  is the ratio of the hole impact ionization rate to that of electrons.  $F(M)$  is one of the main factors which limit the best possible energy resolution.

**Large-Area Avalanche Photo Diode developments:** APDs for the readout of PWO crystals have already been developed for the CMS experiment at CERN [32]. These APDs have several advantages: compactness with an overall thickness of about 200  $\mu\text{m}$ , low cost, insensitivity to magnetic fields and a high quantum efficiency of approximately 70%. A disadvantage of these APDs is their relatively small active area of  $5 \times 5 \text{ mm}^2$  compared to the area of the crystal end faces. For that reason, the development of large-area avalanche photo-diodes by Hamamatsu [41] with an active area of  $10 \times 10 \text{ mm}^2$  was initiated by the PANDA collaboration. The LAAPDs for PANDA will have the same internal structure as the APDs for CMS (see Figure 4.5). In the final PANDA setup there will be two rectangular LAAPDs attached to one end-face of the PWO crystal. Figure 4.6 shows a picture of standard APDs and LAAPDs to compare the different sizes of the active areas.

The crystals used for the test measurement at the MAMI accelerator, Mainz, Germany, have an end face area of  $4 \text{ cm}^2$  and were covered with one square LAAPD of  $1 \text{ cm}^2$ . Cooled down to  $-25^\circ\text{C}$  PWO-II crystals yield about 500 photons per MeV. The applied square LAAPDs have a quantum efficiency of 75%. Therefore, the resulting signal of the LAAPD is generated by 94 electron-hole pairs per MeV [7].

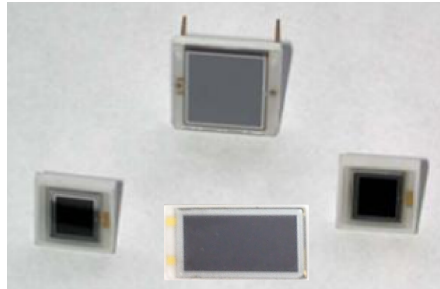


**Figure 4.6:** Photograph of two standard ( $5 \times 5 \text{ mm}^2$ ) APDs, one square LAAPD ( $10 \times 10 \text{ cm}^2$ ), and one rectangular ( $7 \times 14 \text{ mm}^2$ ) LAAPD [41].

## 5. Signal analysis for the PANDA EMC

As mentioned in the previous chapter, the PANDA EMC in the target spectrometer will be built with PbWO<sub>4</sub> (PWO) crystals [7]. The photo sensors are directly attached to the end face of the individual crystals and the preamplifier will be placed close to the photo sensor for optimum performance. To improve the light yield of PWO scintillators the EMC will be operated at a low temperature of -25 °C. Operation at low temperature also improves the noise performance of the preamplifiers. This helps to achieve the required large dynamic range of the front-end electronics. However, a placement of the electronics in the cold detector volume requires to minimize the power-dissipation of the preamplifiers.

The challenging requirements for the PANDA detector (Chapter 3) can only be met by a new approach to the data acquisition system (DAQ): the "trigger-less DAQ": the analog preamplifier signals will be continuously digitized by Sampling ADCs (SADCs). The system must be able to detect events and pre-process them on-line to extract and transmit only the physically relevant information. Due to mechanical constraints it is impossible to bring all analog signals outside the calorimeter volume, since the solenoid magnet only allows a limited space for feed-throughs. Therefore, the digitization module which digitizes the preamplifier signal will be placed inside the calorimeter volume but outside the low-temperature region [7]. Optical links will be employed to transfer the digitized data via a multiplexing stage in a fast and compact manner to the computer node.

It is impossible to store all the data produced by the digitizer modules. Therefore, only reduced information should be reported and stored, namely the energy and the time-stamp of each hit. To derive this information reliably and fast during data taking, i.e. "on-line", for each incoming event, the so-called feature-extraction algorithm was developed in this work. This data-processing algorithm will be applied to the digitized data. Compared to an analog signal treatment by filtering and noise suppression, such a digital treatment allows more flexibility. By tuning the parameters of the digital signal-processing algorithm one can provide better results. This chapter will focus on the main readout electronics chain for the PANDA EMC, the preamplifiers, and the feature-extraction algorithm.

### 5.1 General EMC Readout Scheme

The readout scheme of the electromagnetic calorimeter contains the low-noise charge-sensitive preamplifier and shaper units, the digitizer module, and the data multiplexer (MUX). The concept of the readout scheme is depicted in Figure 5.1.

The low-noise charge-sensitive preamplifier, combined with a shaper stage, is placed in the cold area of the calorimeter and directly attached to the photo sensor. The digitizer modules are located at a distance of 20-30 cm and 90-100 cm for the Barrel EMC and the Forward Endcap EMC, respectively, [7] from the analog circuits and outside the cold volume. The digitizer modules consist of high frequency, low-power pipelined ADC chips

---

[7], which continuously sample the amplified and shaped signals. The features of the individual signals are extracted in the digitizer module. The digital data are further transferred by optical-link connections to Data Multiplexer units which combine information from a few EMC-digitizers and transfer the data to a Compute Node. This is a FPGA-based processing unit for on-line data processing, e.g. cluster finding for the EMC and particle identification.

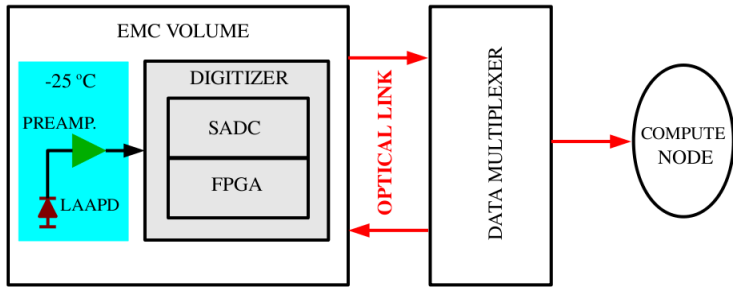


**Figure 5.1:** The layout of the readout electronics for the PANDA EMC.

### 5.1.1 Charge-sensitive preamplifier

As already mentioned in the previous Chapter, when an incident photon interacts with the detector material a shower of charged particles is produced which generates scintillation light and subsequently a charge signal in the photo sensor. For e.g. a Geiger-Müller tube and many scintillation counters, the amount of produced charge is large and the corresponding large voltage pulse can drive a long cable. In a semiconductor detector, however, the produced charge is small and it needs amplification. The first-step amplification element is called “preamplifier” [42]. The preamplifier is located close to the detector to prevent a capacitive loading. One function of the preamplifier is to terminate the capacitance quickly and, therefore, to maximize the signal-to-noise ratio. For this reason, the preamplifiers should be placed as close as possible to the detector. The rise time of the output pulse should be kept as short as possible, equivalent to the charge collection time in the detector. The decay time of the pulse is relatively long (20 - 100  $\mu$ s) to allow full collection of the charge from the detector [42].

Preamplifiers can be either of the voltage-sensitive or charge-sensitive type. A schematic diagram of a voltage-sensitive configuration is shown in Figure 5.2. If the time constant of the input circuit is large compared to the charge collection time, then the input pulse amplitude is equal to

$$V_{\max} = \frac{Q}{C} \quad (5.1)$$

where  $C$  is the input capacitance and  $Q$  is the produced charge. For most detectors the input capacitance is fixed, for example, in the case of a voltage-sensitive preamplifier the output pulse is proportional to the charge  $Q$  liberated by the incident radiation. However, in semiconductor detectors, the detector capacitance can change with the operating parameters.

In these situations, a voltage-sensitive [42, 43] preamplifier is undesirable since the fixed relationship between  $V_{max}$  and  $Q$  is not applicable anymore. For this case the charge-sensitive preamplifier is the best option.

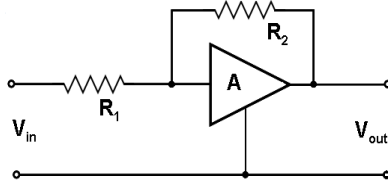


**Figure 5.2:** Schematic diagram of a simplified voltage-sensitive preamplifier with amplification  $A$  of the operational amplifier.  $R_1$  is the input resistance and  $R_2$  is the feedback resistance. If  $A \gg R_2/R_1$  then  $V_{out} = -V_{in} \cdot R_2/R_2 \cdot R_1$ .

The elements of a charge-sensitive configuration are shown in Figure 5.3. For this circuit, the output voltage is proportional to the total integrated charge in the pulse. The rise time of the pulse produced by the preamplifier is determined only by the charge collection time in the detector and is independent of the capacitance of the detector or preamplifier input.

For the PANDA EMC two different charge-sensitive preamplifiers have been developed: an ASIC (Application-Specific Integrated Circuit) preamplifier and a discrete-component preamplifier including a shaper unit, developed at GSI Darmstadt, Germany, and at University of Basel, Switzerland, respectively [7]. Here, we give a short functional description of these preamplifiers.

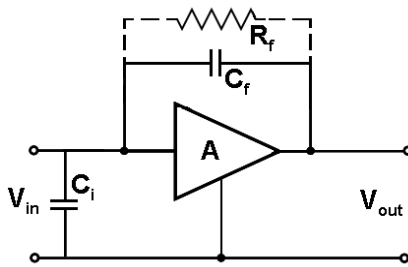


**Figure 5.3:** Schematic diagram of a simplified charge-sensitive preamplifier with amplification  $A$  of the operational amplifier. The time constant given by the product  $C_f R_f$  determines the decay rate of the tail of the output pulse.  $C_i$  is the input capacitance,  $C_f$  the feedback capacitance, and  $R_f$  is the feedback resistance [42]. If  $A \gg (C_i + C_f)/C_f$  then  $V_{out} = -Q/C_f$ .

The **Low-Noise Low-Power Consumption (LNP)** preamplifier is a discrete charge-sensitive preamplifier [7], which was primarily designed for the LAAPD readout. The design was further developed for the readout of the vacuum photo-triode (VPT) for the

Forward Endcap EMC. The LNP was implemented in the prototype of the Barrel EMC for the readout of the Large-Area Avalanche Photo Diodes to study the performance in beam experiments. The LNP has excellent noise performance in combination with low power consumption. The LNP has a power consumption of 45 mW in the idle state, but the power dissipation is dependent on the event rate and the photon energy [7]. A reasonable maximum power consumption of  $\sim 100$  mW can be presumed. To reach a low detection threshold, the noise performance of the preamplifier is very important. The noise of the LNP preamplifier with an input capacitance of 22 pF at  $-25^{\circ}\text{C}$  has a typical equivalent noise-charge (ENC) of 235 e<sup>-</sup> [44].

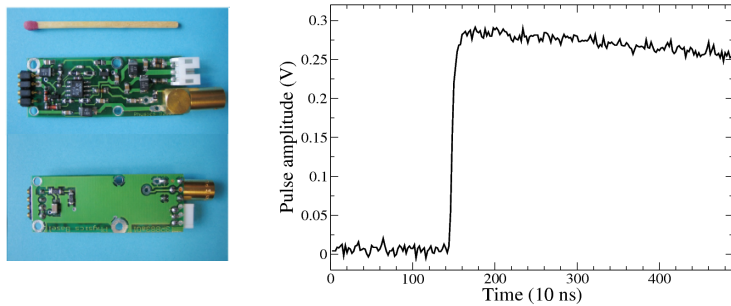


**Figure 5.4:** The single-channel LNP preamplifier prototype circuit board and a typical output pulse shape. The pulse shape is recorded with a 100 MHz sampling rate and 16-bit resolution SADC.

The LNP preamplifier is designed for a single-pulse charge input of maximum 4 pC. The single-ended output of the preamplifier is designed to drive a signal on a  $50\ \Omega$  line. The rise time and fall time (change of the signal from the 10% level to the 90% level) of the LNP preamplifier signals are 10 ns and 55  $\mu\text{s}$ , respectively. Figure 5.4 shows a photograph of the preamplifier and the output pulse shape.

**ASIC APFEL preamplifier:** This charge-sensitive preamplifier and shaper ASIC APFEL (Asic Panda Front-End Electronics) was developed for the readout of the avalanche photo diodes with a capacitance of 300 pF [45]. It has two independent channels with dual-gain output per channel. The gain ratio of 1:32 per single LAAPD was chosen to cover a large dynamic range from 10 MeV up to 12 GeV.

An overview of the readout stages is shown in Figure 5.5. A channel consists of a charge-sensitive amplifier (CSA), a pulse shaper and an output stage. The ASIC preamplifier and shaper will be placed in the Barrel EMC. The bulk of particles produced in the antiproton annihilations will be emitted in the forward direction and the hit rate in the Barrel EMC will be much less in comparison with the Forward Endcap EMC.

Therefore, the charge sensitive preamplifier output in the ASIC is connected to a shaper unit with 250 ns peaking time [46], in order to reach a better energy resolution due to a better charge collection. The ASIC chip will be placed on a specially designed Printed-Circuit Board (PCB) which is directly soldered to the LAAPD. The ASIC chip itself is protected by a  $2\times 2\ \text{cm}^2$  large capsule made from PEEK material. The capsule will be attached to the end face of the PWO crystal. The output signal of the ASIC chip is connected via flat cable to a driver board. To get maximum performance, 10 cm length has been found

as optimal length. The driver board has channels with different gain to cover the required dynamic range. The test board and the corresponding output pulse shape are shown in Figure 5.6.

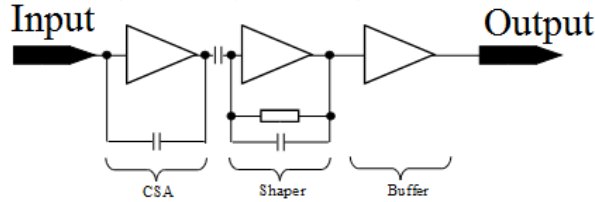


**Figure 5.5:** Concept of the ASIC preamplifier [46].

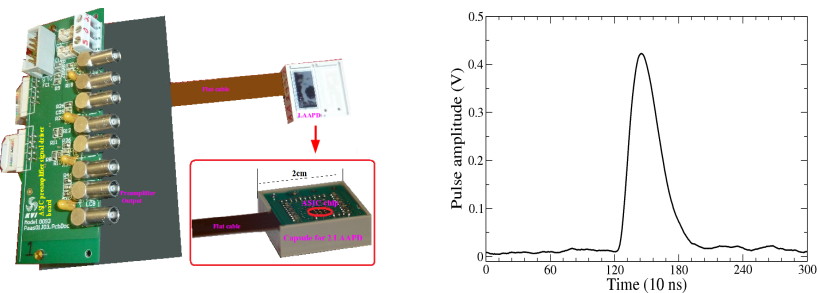


**Figure 5.6:** Left: The ASIC-chip preamplifier board; Right: a voltage signal with the typical pulse shape [47].

### 5.1.2 SADC readout

For the data acquisition, the preamplifier output signals are digitized by Sampling Analog-to-Digital Converters (SADCs). The SADC takes samples of the continuous analog signal and converts these to a time series of digital values.

The application of an SADC is the best choice to prevent a high dead time of the detector, which might occur due to the expected high annihilation rate of  $2 \cdot 10^7$  annihilations/s. The digitized signal traces are stored to a buffer in a FPGA (Field-Programmable Gate Array) which is part of the digitizer module. The program-code, the so-called firmware loaded to the FPGA, can process the digitized signal and will provide the detected pulse features. An implementation of the feature extraction into an FPGA will be described in Chapter 7. For all test experiments, we have used a commercial SADC, the STRUCK SIS3302 module [48]. The SIS3302 module is an 8-channel ADC/digitizer board with a sampling rate up to 100 MHz for an individual channel and a resolution of 16 bit [48].

The SADC contains 5 SPARTAN FPGA from the Xilinx family. Four FPGAs process data from 8 ADC channels and one FPGA is controlling the VME interface. The main features of the SADC are the following:

- 8 channels;
- 16-bit resolution;
- 32 MSamples/channel memories;
- External clock range 1 - 100 MHz;
- Input bandwidth of 50 MHz;
- +5, +12V and -12 V VME standard voltages.

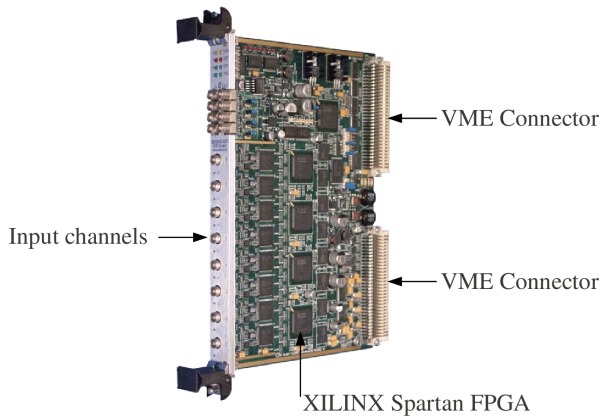


**Figure 5.7:** SIS 3302 8-channel sampling ADC with 100 MHz sampling rate and 16-bit resolution.

## 5.2 Data Acquisition

The VME-based Data AcQuisition system (DAQ) applied for the test experiments consists of a single “branch” within the GSI Multi-Branch System (MBS) framework [49].

The data sender is a RIO-3 [50] processor, which resides in the VME crate. The RIO-3 handles the readout of the digitizers (SADCs, Time-to-Digital Converters) and then passes the data via TCP/IP (transmission control protocol/internet protocol) to a Lynx-OS PC, which acts as data receiver. The latter formats the events and makes these available to analysis clients (e.g. via a remote event server) and controls taping or disk storage. For on-line visualization of the data stream, several different software packages can be used. For all our test measurements, we have used the GO4 program package for data analysis and visualization [51].

### 5.3 The feature-extraction algorithm

The charge-sensitive preamplifier output is directly digitized by the SADC. The direct digitization has some advantages in comparison with an analog signal-filtering approach in between. Applying digital signal processing tools to the digitized signal can provide a better performance, as already discussed above. Another disadvantage of analog filtering components is that they could be sensitive to environmental influences, e.g. temperature changes or magnetic fields, but the digital filter remains unaffected by such environmental influences [52].

To extract energy and time information of a digitized signal data-stream, digital filter processes are applied such as the Moving-Window Deconvolution (MWD), the Moving Averaging (MA), and the Constant-Fraction Timing (CFT). These are explained in the following:

**Moving Window Deconvolution:** The particle energy or energy deposition corresponding to the measured signal is usually obtained from the signal amplitude which is generated by an analog shaping preamplifier with a combination of integrating and differentiating circuits with time constants of a few  $\mu\text{s}$ . Equivalently, to extract the pulse amplitude from a digitized preamplifier signal, the MWD process is applied [53]. The MWD filter transforms the fast rising pulse with a long exponential tail into a rectangular shaped signal [54].

As mentioned above, the output of a charge-integrating preamplifier has a fast rise time of 10 ns and an exponential tail (fall time) of about 55  $\mu\text{s}$ . The pulse provided by an ideal charge-integrating preamplifier should have a step-like shape, where the height of the step corresponds to the accumulated charge. However, the resistor in the feedback loop of the preamplifier continuously discharges the integrating capacitor. Therefore, the output pulse is a convolution of a step-like function with an exponential decay. To restore the original height of the step one needs to apply a deconvolution procedure. Let us consider a convoluted pulse  $f(t)$  starting at time of  $t_0$  which is the time  $t = 0$ ,

$$f(t) = \begin{cases} 0, & t < 0 \\ -\frac{1}{\tau}t \\ A \cdot e^{-\frac{1}{\tau}t}, & t \geq 0 \end{cases} \quad (5.6)$$

where  $\tau$  is the signal decay constant and  $A$  the pulse amplitude. The amplitude  $A$  at time  $t_0$  can be derived from

$$\begin{aligned} A &= f(t_n) + A - f(t_n) = f(t_n) + A \cdot (1 - e^{-\frac{1}{\tau}t_n}) = \\ &= f(t_n) + \frac{1}{\tau} \int_0^{t_n} f(t) dt = f(t_n) + \frac{1}{\tau} \int_{-\infty}^{t_n} f(t) dt \end{aligned} \quad (5.7)$$

where  $n$  is the sample number. Since we are going to apply the MWD filter digitally to the digitized pulse it is useful to change from the continuous to the discrete expression:

$$A[n] = x[n] + \frac{1}{\tau} \sum_{k=-\infty}^{n-1} x[k] = x[n] - (1 - \frac{1}{\tau})x[n-1] + A[n-1] \quad (5.8)$$

The deconvolution equation 5.7 transforms the continuous-discharge preamplifier signal into a signal from a transistor-reset preamplifier, which is a stair-case signal. Applying a numerical differentiation to the discrete form of the deconvolution equation 5.7, we obtain the MWD equation

$$\begin{aligned} MWD_m[n] &= A[n] - A[n-m] = \\ &x[n] - x[n-m] + \frac{1}{\tau} \sum_{k=n-m}^{n-1} x[k] \end{aligned} \quad (5.9)$$

where  $m$  is the output pulse length given as the number of sample points<sup>1)</sup>. The process of MWD filtering is illustrated in Figure 5.8. A deconvolution operation does not improve the signal-to-noise ratio [55]. Therefore, the noise contribution to the MWD signal is reduced by a subsequent low-pass filter.

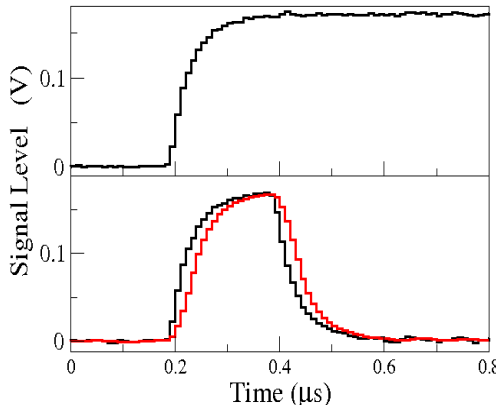


**Figure 5.8:** Top: the raw preamplifier signal with a total pulse length of 55  $\mu$ s, but for the MWD only a few sample points are needed after the rising edge. Bottom: pulse shapes obtained after the MWD (black histogram) and the combined filters MWD and MA (red histogram).

The **Moving Average (MA)** procedure is a filter algorithm in digital signal processing. A number of sample points from the input signal are averaged to produce each point of the output signal. This averaging action can remove the high-frequency components in the signal and it plays the role of a low-pass filter. The MA equation for this filter procedure reads as follows [55]

$$MA[n] = \frac{1}{L} \sum_{j=0}^{L-1} A[n+j] \quad (5.10)$$

---

<sup>1)</sup> For convenience,  $m$  is also occasionally used to indicate the deconvolution differentiation length in [ns], i.e. the number of sample points is multiplied by the length of the sampling interval.

where  $L$  is the number of sample points in the average<sup>2)</sup>. The parameter  $L$  is usually equal to the integration time of the analog filter. Increasing the number of averaged samples can cause a decrease of the noise level. Figure 5.9 shows the variation of the noise level for different averaging lengths. We observe that the RMS width of the noise level can be reduced from 1 MeV (for the conventional electronics) down to 0.3 MeV.

The MWD procedure together with the MA filter provides the pulse shaping and the noise reduction of a digitized preamplifier signal. Tuning of the parameters of the MWD and MA algorithms can influence the obtained pulse shape. For an averaging length  $L$  equal to the deconvolution differentiation length  $m$  a triangular shape is generated, and if  $L \neq m$  a trapezoidal signal shape is generated. Defining  $\oplus$  as the operator for the combined application of MWD and MA filter, we obtain:

$$T_L^m[n] = MA_L[n] \oplus MWD_m[n] \quad (5.11)$$

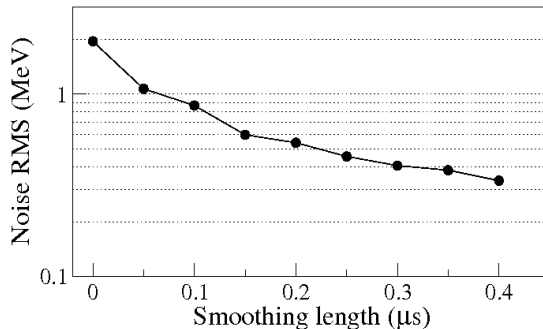


**Figure 5.9:** The dependence of the noise level on the smoothing length  $L$ .

The Forward Endcap EMC [7] will operate at high single-hit rates, up to 500 kHz. To avoid pile-up of different signals it is extremely important to keep the hit response of the single-crystal detector as short as possible. In order not to loose efficiency of the PANDA detector, the pileup probability of the PANDA EMC needs to be limited to 1% [7]. For the 500 kHz hit rate, this requirement demands a very short response time of the detector of about 20 ns. With the optimal shaping parameters for the highest energy resolution, namely with a differentiation time-constant of 200 ns, the pile-up probability will be  $\sim 14\%$ , which is unacceptably high. Therefore, the detector response should be shortened while keeping the EMC energy resolution within the requirements defined by the physics program, namely below about 3%. The pulse shape of the LNP preamplifier, used in the Forward Endcap EMC, is shown in Figure 5.10. As described above, the MWD digital filter differentiates the incoming pulse and compensates for the exponential discharge of the integrating capacitor in the preamplifier. It was found that the resulting tail of the LNP preamplifier pulse, shaped by the MWD filter, has an exponential behavior.

<sup>2)</sup> For convenience,  $L$  is also occasionally used to indicate the smoothing length in [ns], i.e. the number of sample points is multiplied by the length of the sampling interval.

Therefore, such tail can be compensated by applying a second MWD filter with the corresponding decay constant. The resulting double MWD shaping of an LNP preamplifier trace is shown in Figure 5.10.

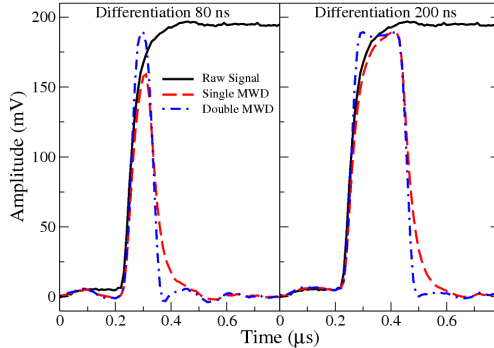


**Figure 5.10:** LNP preamplifier pulse shape before (black solid line) and after single (red dashed line) and double (blue dash-dotted line) MWD filtering for 80 ns length (left) and 200 ns (right) differentiation time constants of the MWD filter [56].

The double MWD filtering allows obtaining a much shorter pulse and recover its original amplitude for short differentiating time-constants without increasing the noise level. Figure 5.11 shows the recovery of the pulse amplitude after a second MWD filtering as a function of the differentiation time-constant of the first MWD filter. Only for the very short differentiation time-constants, below 80 ns, the pulse amplitude can not be completely recovered even though it provides a much higher amplitude than the single MWD filtering. Such a signal recovering technique allows to efficiently achieving a low triggering threshold while reducing the pulse width. In order to exploit this advantage, it is preferable to keep the pulse-amplitude recovery at the level of minimally 95%. The usage of the double MWD

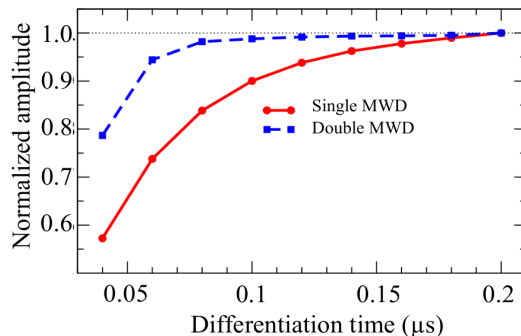


**Figure 5.11:** The pulse amplitude after single (red solid line) and double (blue dashed line) MWD filtering as a function of the differentiation time-constant of the first MWD filter [56].

filtering does not influence the resulting energy resolution of the detector. Using signals from the tagged-photon measurements at 1 GeV (see Chapter 6.3.5), we observe in Figure 5.12 that the cluster energy resolution for  $\gamma$  rays is the same for the single and double MWD filtering [56]. For the Forward Endcap EMC, taking into account the above mentioned criteria for the energy resolution and the pulse-amplitude recovery, the double MWD filtering with the differentiation time-constant of about 60 ns will provide the best performance in terms of low pile-up probability without compromising the energy resolution of the detector.

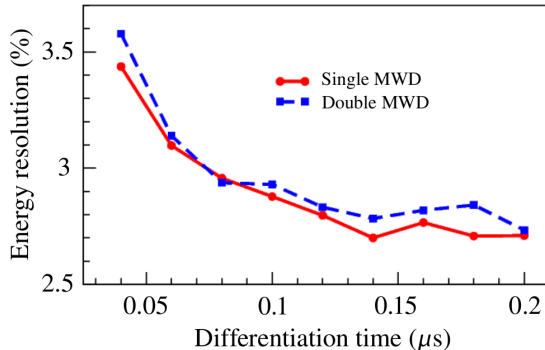


**Figure 5.12:** Measured cluster energy resolution for tagged photons of 1 GeV energy obtained using the single (red solid line) and double (blue dashed line) MWD filtering method. The energy resolution is plotted as a function of the differentiation time-constant of the first MWD filter [56].

The **Constant Fraction Timing (CFT)** algorithm is applied to extract the precise time information from the measured signal. This signal time-stamp can be used to correlate particle signals to specific events. As mentioned before [7], for the precise event-time determination and random background suppression the timing performance of the EMC was considered an important issue. A good time resolution (better than 1 ns) is required for the suppression of random coincidences. The timing performance of scintillation detectors is mainly limited by variations of the signal shape and the signal-to-noise ratio. The variation of the signal shape is caused by the scintillation mechanism in the detector crystals [57, 58, 59].

Traditionally, a constant-fraction time pick-off is performed by producing a trigger at the zero-crossing level of a bipolar pulse [57], which is created by subtracting an attenuated copy of the input pulse from a delayed copy of the same pulse [57]. In our signal processing procedure the CFT algorithm is implemented digitally after the MWD operation:

$$CFT[n] = MWD[n] - k \cdot MWD[n+d] \quad (5.12)$$

where  $n$  is the sample number,  $k$  is an attenuation coefficient (giving the “constant fraction”), and  $d$  is a delay. In our measurements, the  $k$  value was set to  $\sim 40\%$  of the original pulse amplitude and the delay was set equal to the signal rise time. When we digitally transform the unipolar preamplifier signal to the bipolar CFT signal, the bipolar signal crosses the time axis and this zero-crossing is considered a well-defined time-stamp.

Figure 5.13 shows the process to obtain the CFT signal by applying digital signal processing techniques. The signal is analyzed by a linear interpolation to determine the zero-crossing time. This time stamp defines the arrival time of the pulse (or the event).

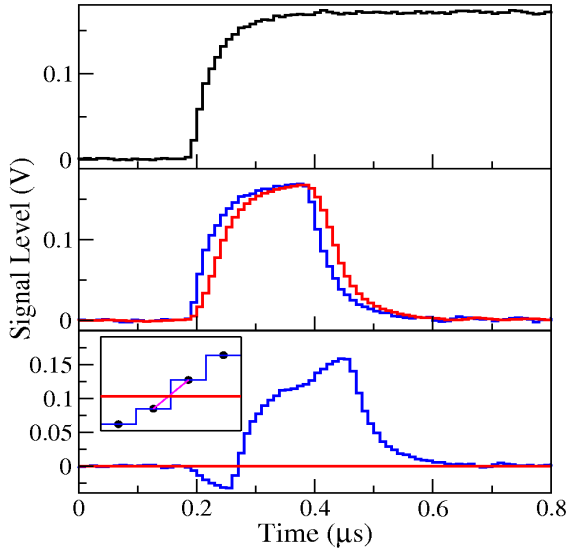


**Figure 5.13:** The signal processing sequence to obtain the CFT signal and the time stamp. Top: the raw LNP preamplifier signal, middle: the resulting MWD (blue histogram) and smoothed MWD (red histogram) pulses; bottom: the CFT signal.

## 6. Performance studies

In this chapter, the performance of the PANDA EMC front-end readout system is investigated. Three different test measurements and their analysis results are described. Two of these measurements were performed with a single PWO crystal and the third one with a matrix of 60 PWO crystals.

The setup with a single crystal consisted of two LAAPD photo sensors, attached to opposite end faces of the PWO crystal bar and coupled to LNP discrete component preamplifiers. This setup was applied in measurements with a light pulser and in test measurements with a high-energy ion ( ${}^6\text{Li}$ ) beam. Further details of these experiments are described in the first and second section of this chapter.

The third section describes the details of a test measurement with a high-energy tagged photon beam. The aim of this experiment was twofold: in order to obtain precise energy information the beam was directed onto the central crystal of a matrix of 60 PWO crystals; to obtain precise relative time information the beam was directed between the central and one of its neighboring crystals, which provided us with two crystals detecting an about equal amount of energy.

### 6.1 Timing performance studies

#### 6.1.1 Setup with LED light pulser

The light pulser [60] generates fast light pulses with 14 ns rise time and the same wavelength as the mean of the scintillation light distribution (420 nm or blue light) of the PWO crystal. Bundles of optical fibers [61] guide the light from the pulser to the crystal. The LAAPD and LNP preamplifiers are attached at both end faces of the PWO crystal.

The light is injected at both end faces of the crystal bar. The complete experimental setup is placed in an air-tight and light-tight aluminum box and measurements were done at room temperature and at -25 °C. Cooling was achieved by flowing cooled methanol through pipes in an aluminum block and placing the crystal and attached sensors into a central cavity of this block. To prevent ice forming on the crystal and the electronics, the humidity in the measurement box was kept at a low level by flushing with dry nitrogen through an attached tube. The setup inside the measurement box is shown in Figure 6.1.

#### 6.1.2 The results with LED light pulser

Using the LED light pulser, we have studied the performance of both the LNP and the ASIC preamplifiers. In this way, we obtained important results on the time resolution for different light intensities or the correspondingly produced charge in the LAAPD. For this purpose, we studied the coincidence time, i.e. the difference of the time stamps of the two LAAPDs which were coupled to both end faces of the PWO crystal. The time stamp was

---

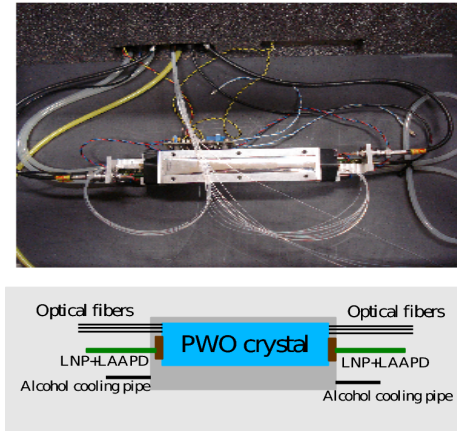


**Figure 6.1:** Experimental setup. Top: a photograph of the setup with the crystal in the aluminum block, attached LNP preamplifiers, fibers and pipes for the cooling liquid and nitrogen. Bottom: a sketch of the experimental setup.

determined from the zero-crossing point [57] after a linear interpolation (see Figure 5.13). The results of the obtained time resolution for different produced charge values are shown in Figure 6.2. The time resolution  $\Delta t_{RMS}$  for a single LAAPD sensor is determined from the RMS width of the coincident time distribution, divided by  $\sqrt{2}$ . We observe that the time resolution improves strongly for higher values of the collected charge and thus with the signal-to-noise ratio. At small values of the collected charge, the time resolution deteriorates due to the influence of the noise level.

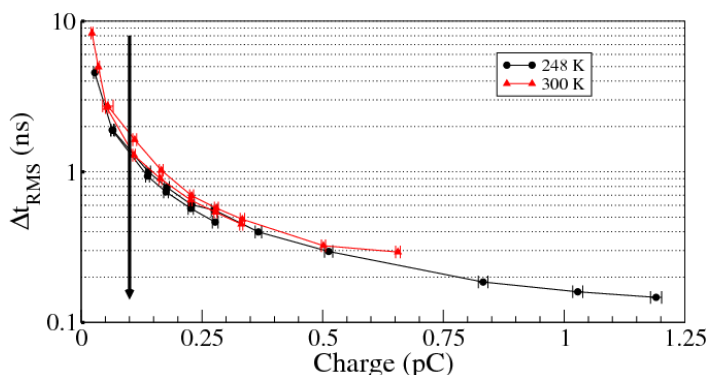


**Figure 6.2:** The dependence of the time resolution on the charge collected at the LAAPD. The black arrow indicates the position of cosmic muon energy deposition. The solid black lines show two measurement series at -25 °C and the solid red lines represent two measurement series at room temperature.

In order to confirm the constant fraction timing (CFT) algorithm we did parallel timing measurements and compared the results obtained by a VME-based Time-to-Digital Converter (TDC) and the sampling ADC readout. The test setup and the result are presented in Figure 6.3. The signal from one end face of the PWO crystal is split and sent to the SADC and the TDC, the signal from the other end face is delayed before splitting. By varying the delay, we could change the relative time between the two LAAPDs. In Figure 6.3 (bottom), we observe a linear correlation between the absolute times determined by the SADC, using the CFT method, and the TDC. The linearity confirms that the digital implementation of the CFT algorithm is working well.

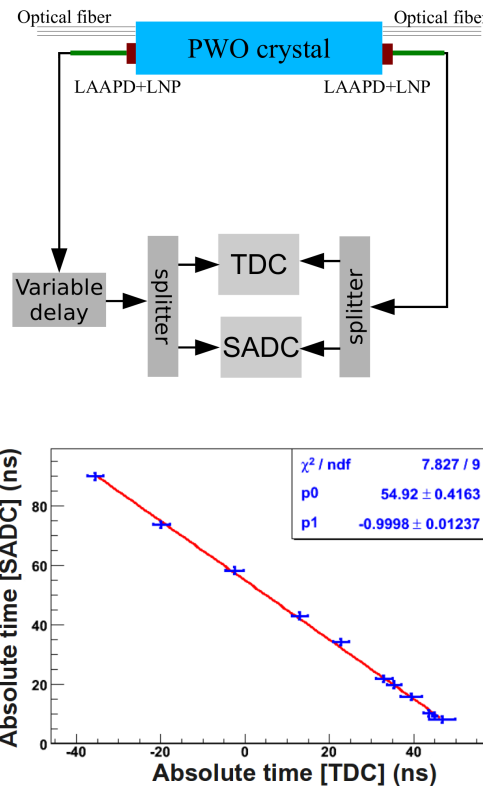


**Figure 6.3:** Comparison of timing measurements with Sampling ADC running at 100 MHz sampling rate and TDC. Top: Sketch of the experimental setup. Bottom: Correlation of the absolute time measured by the SADC and the TDC for different applied delay values. The delayed and non-delayed signals are split into two parts via signal splitters.

### 6.1.3 Time precision studies

The time resolution is defined by the digital implementation of the CFT timing method. Here we study the precision of this method. Figure 6.4 shows the coincidence time between 2 LAAPDs for 100 MHz (top) and 50 MHz sampling rate (bottom).

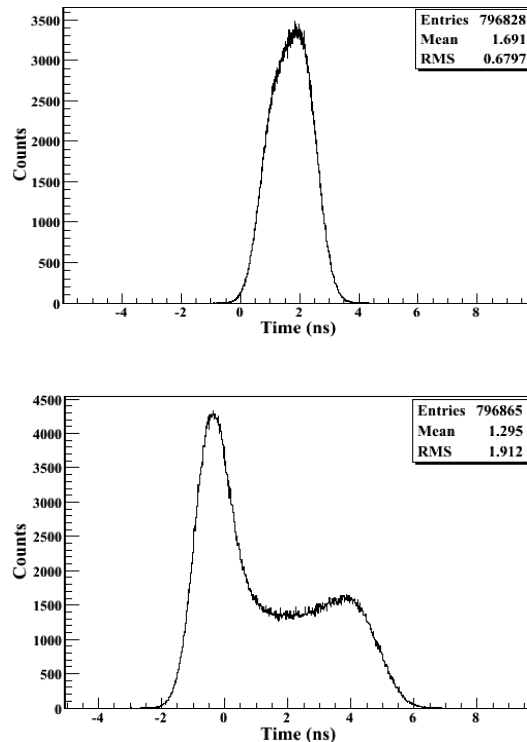


**Figure 6.4:** Coincidence time between 2 LAAPDs measured with LNP preamplifiers. Top: measurement at 100 MHz sampling rate. Bottom: measurement at 50 MHz sampling rate.

The observed shape of the distributions is not symmetric and the asymmetry becomes worse at 50 MHz sampling rate. As mentioned before (Chapter 6.1.2) the coincidence time is defined as the difference of time stamps of individual LAAPDs and the time stamp itself is determined from a linear interpolation to the zero-crossing point of the CFT signal (see Figure 6.5). The linear interpolation is done between two nearest sampling points, one below and one above the zero line. If the true zero-crossing point can not be determined by linear interpolation, the distribution of the coincidence time will be smeared by the corresponding uncertainty. To clarify this problem, we introduce the phase. At a given sampling frequency  $f$  the sampling interval is  $\Delta t_f = 1/f$ . The phase  $p$  is defined by the relative time  $\Delta t_p$  between the time-stamp of the pulse and the preceding sampling point of the SADC time:  $p = \Delta t_p/\Delta t_f$ , thus  $p$  varies in the range  $[0, 1]$ . The phase determines the phase slope of the linear interpolation of the zero-crossing time. In the graph at the bottom of Figure 6.5 the black-line CFT signal is shifted by a phase  $\tilde{p}$  relative to the blue-line signal. This variation clearly affects the position of the zero-crossing point.

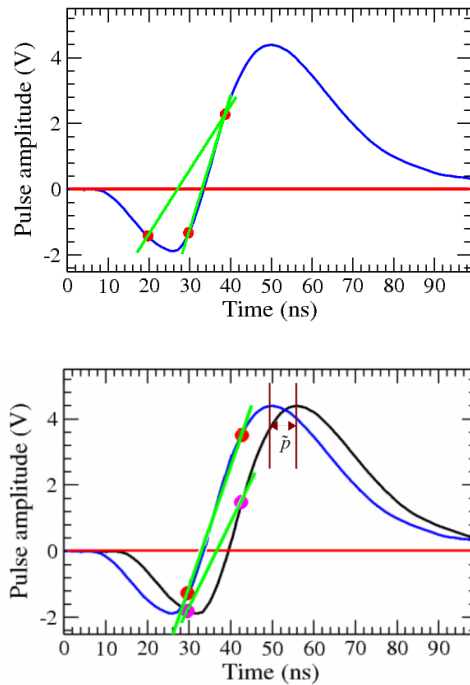


**Figure 6.5:** Top: Illustration of the linear interpolation to the zero-crossing point for a CFT signal measured with 100 MHz and 50 MHz sampling frequency. Bottom: Illustration of the shift in the interpolated zero-crossing for a CFT signal shifted in the sampling interval for 100 MHz sampling frequency by a relative phase  $\tilde{p}$ .

Systematic experiments were performed to study the dependence of the time determination on the phase. The experimental setup is shown in Figure 6.6. The pulse generator provides the trigger for two LED light pulsers. One of the LED light-pulser trigger signals was delayed with respect to the other one. The summed signal of both LED light pulsers provides a double-pulse which is injected into the LAAPD sensor via an optical fiber bundle. The LAAPD output is directly connected to a preamplifier/shaper unit. The preamplifier/shaper output is split via an impedance-matched resistor splitter into two equal signals which are fed simultaneously into the TDC and the SADC for digitization. The TDC provides a precise time measurement and will be used as an accurate reference for the time measurement of the SADC.

In order to determine the relative timing between the TDC and the SADC, the delay module varied the time between the two signals of the double-pulse. The double-pulse structure obtained from the preamplifier was digitized by the SADC. Figure 6.7 shows an example of the digitized signal shape obtained directly after the preamplifier (right) and after the shaper unit (left). The time between the two pulses is 700 ns in this example. The generated double pulse is characterized by the two time stamps  $t1$  and  $t2$ .

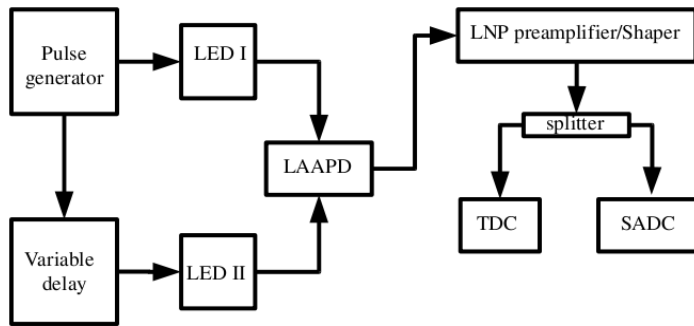


**Figure 6.6:** Scheme of the experimental setup with LNP preamplifier and shaper for investigating the CFT timing precision.

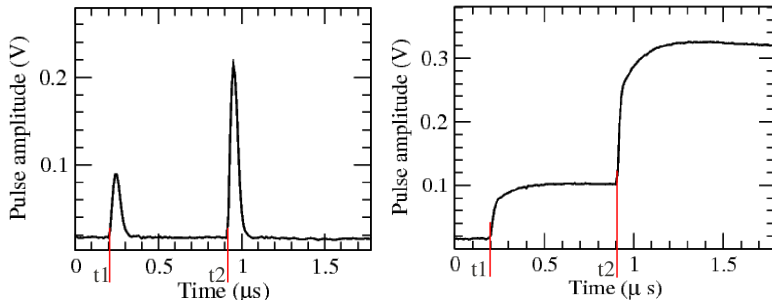


**Figure 6.7:** Signal trace of a double-pulse recorded by the SADC. Left: the shaper output signal. Right: the unshaped LNP preamplifier signal.

The time difference  $\Delta t$  is determined as the difference between the time differences  $\Delta t_{TDC} = t1_{TDC} - t2_{TDC}$  and  $\Delta t_{SADC} = t1_{SADC} - t2_{SADC}$  of  $t1$  and  $t2$ , measured by the TDC and by the SADC applying the CFT method, respectively:

$$\Delta t = \Delta t_{TDC} - \Delta t_{SADC}$$

The error in this measurement will be dominated by the error in the precision of the CFT method, as the TDC resolution (12-bit resolution) is much better. The TDC measures the relative time but no absolute time. The CFT algorithm can provide the absolute time with respect to the preceding SADC sampling point. The absolute time is determined for the SADC from the mean value of the  $\Delta t_{SADC}$  distribution. Figure 6.8 shows the correlation obtained for the time difference measured by TDC and SADC. Using this correlation we can calibrate the measured time of the SADC according to the precisely measured TDC time.

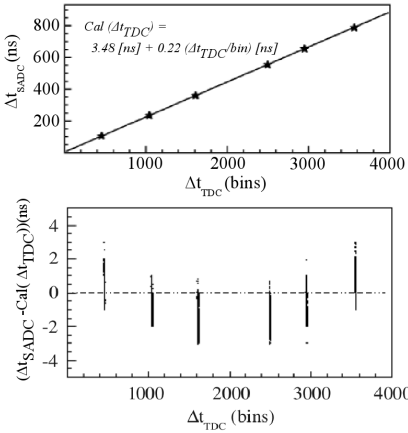


**Figure 6.8:** Top: The correlation between the time differences measured by TDC and SADC. The obtained calibration of the SADC time will be used for corrections of the measured SADC time. The uncertainty is smaller than the symbol size. Bottom: The residual plot of the calibration curve shown in the upper panel.

Figure 6.8 reveals a linear timing correlation. If the time determination by the CFT method is misbehaving, we ought to observe a deviation from the linear correlation. According to the result shown in Figure 6.8 the calibration between the TDC time and SADC time is given:  $\text{Cal}(\Delta t_{TDC}) = 3.48 \text{ [ns]} + 0.22 (\Delta t_{TDC}/\text{bin}) \text{ [ns]}$ . It can be seen that the calibration curve, presented in Figure 6.8 is not perfect and that there is a slight deviation from the linear behavior. This slight non-linearity effect is caused by the setting chosen for the TDC in order to achieve the maximum possible range of the TDC. All the measurements, described below, were done in a rather narrow  $\Delta t$  range around the value of  $\Delta t$  about 800 ns. Therefore, the above described non-linearity can be compensated by changing the constant term in the calibration from 3.48 ns to 4.78 and 5.18 ns for 50 and 100 MHz data, respectively. This modification of the calibration was defined such that the mean values of the distributions shown in Figure 6.4 became zero. Using this modified calibration function we recalibrated the SADC time according to the TDC time [62]. Figure 6.9 shows the resulting  $\Delta t$  as a function of the phase of the signal for 100 MHz and 50 MHz sampling rates. The phase dependence was determined for the direct LNP preamplifier signal and the shaped signal. The phase of the first pulse was fixed and the second pulse varied in phase in the range  $[0, 1]$ , as presented on the x-axis of Figure 6.9. According to the calibration obtained from Figure 6.8 we expect the data points to be scattered along the zero-line in Figure 6.9. However, we observe a strong deviation for 50 MHz and some deviation for 100 MHz sampling frequency. The phase of the signal does not depend on the pulse amplitude (Chapter 5), however, it depends on the CFT parameters for fraction and delay. For the reported measurements we have used the optimum fraction and delay values. Therefore, we need to apply a correction according to the measured time (the true time). For this reason, the x-profiles of the two-dimensional histograms have been generated and are shown in Figure 6.10. The distributions are fitted by 2<sup>nd</sup> and 3<sup>rd</sup> order polynomials to obtain the respective correction coefficients.

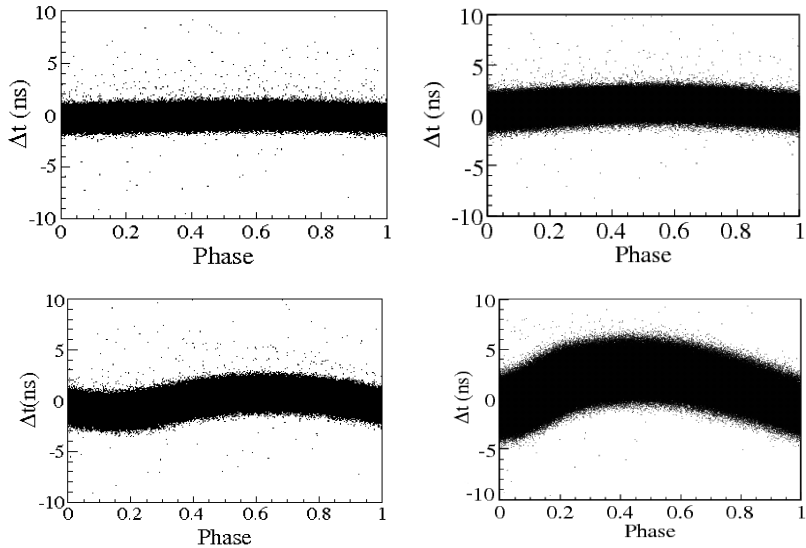


**Figure 6.9:** Scatter plot of time differences  $\Delta t$  for each event as function of the phase [62]. Top and bottom rows: 100 MHz and 50 MHz sampling rate, respectively. Left and right columns: time determined from shaped signal and LNP signal, respectively.

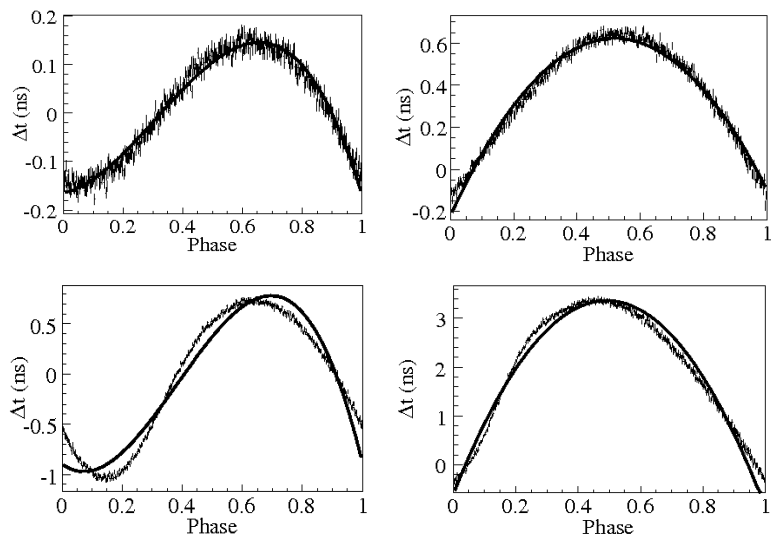


**Figure 6.10:** x-profile of the distribution of mean values in time difference for different values of the phase. Top and bottom rows: 100 MHz and 50 MHz sampling rate, respectively. Left and right columns: time determined from shaped signal and LNP signal, respectively.

The order of the polynomials has been limited for simplicity. Higher orders provide even better fits but the resulting functions cause difficulties for the implementation of the correction method into the Field-Programmable Gate Array (FPGA) for on-line applications.

Applying the resulting correction functions for the LNP preamplifier to the distributions of Figure 6.9 we observe improved distributions in Figure 6.11. The variation of the time differences around the zero line is decreased. If we apply the obtained correction functions to the coincidence time distributions as presented in Figure 6.4 for 100 MHz and 50 MHz sampling rate, we observe in Figure 6.12, that the asymmetric shape has disappeared. The widths of the distributions clearly have improved, which demonstrates the potential of this correction method.

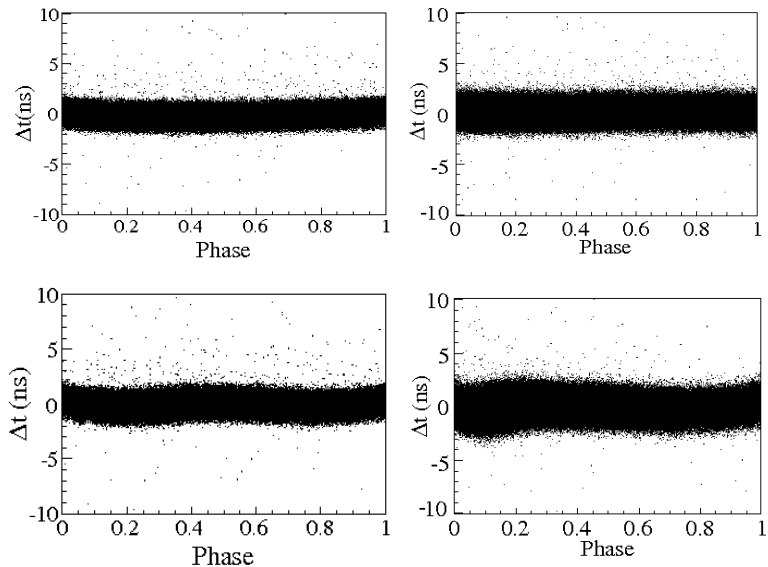


**Figure 6.11:** Same as Figure 6.9 after applying the correction functions obtained from Figure 6.10. Top and bottom rows: 100 MHz and 50 MHz sampling rate, respectively. Left and right columns: time determined from shaped signal and LNP signal, respectively.

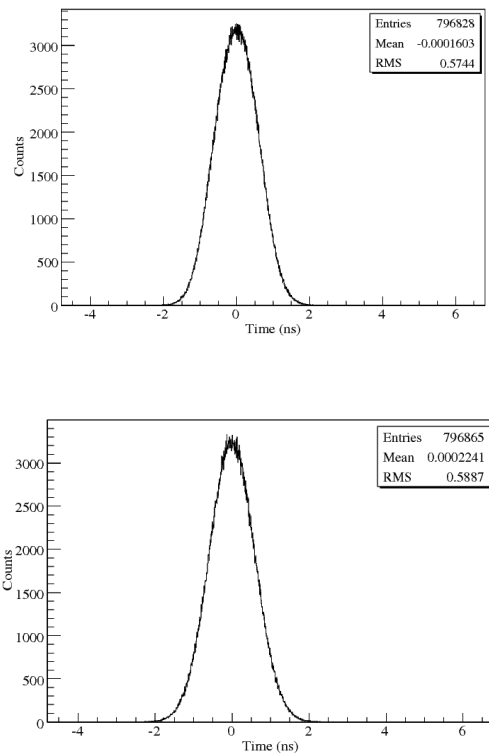


**Figure 6.12:** Same as Figure 6.4 after applying the correction function for the time shift in dependence of the signal phase. Top: measurement at 100 MHz sampling rate; Bottom: measurement at 50 MHz sampling rate.

## 6.2 Single-crystal performance with ${}^6\text{Li}$ ion beam

### 6.2.1 The experimental setup

The performance of the readout electronics chain based on the Sampling ADC technique was studied using the 2 AGeV  ${}^6\text{Li}$  ion beam at GSI, Darmstadt, Germany. The main goal of the shared experiment was to study hypernuclei production in 2 AGeV  ${}^6\text{Li}$  ion beam interactions with a light target, in this case  ${}^{12}\text{C}$  [63]. We exploited this ion beam arrangement to test our setup employing a single PWO crystal with prototype readout electronics. The experimental setup is sketched in Figure 6.13.

The diameter of the beam-spot, measured by the pair of scintillating fiber detector planes, was about 0.4 cm. The applied beam intensities were  $\sim 10^3$  ions/cm $^2$  and  $10^6$  ions/cm $^2$ . The start detector was a plastic scintillator and was included in the event trigger. In front of the start detector, a carbon target was placed. The thickness of the target was 8 g/cm $^2$  [63].

The PWO setup was placed at a distance of  $\sim 2$  m from the target. The setup employed a PWO crystal with dimensions  $20 \times 20 \times 200$  mm $^3$ , two LNP preamplifiers, and one  $10 \times 10$  mm $^2$  LAAPD at either of the two end faces of the PWO crystal bar.

Measurements were done at a crystal temperature of -25 °C for improved light yield of the PWO crystal. During the measurements we kept dry nitrogen flowing continuously to prevent ice forming inside the experimental box.

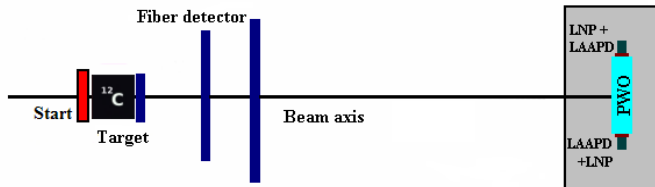


**Figure 6.13:** Experimental setup (top view) used for test measurements with the 2 AGeV  ${}^6\text{Li}$  ion beam. The PWO setup was our light-tight detector box with a single crystal inside and on both small end faces coupled to a LAAPD + LNP preamplifier combination.

### 6.2.2 Results of the ion beam experiment

The preamplifier output signals were directly digitized by the SADC and the digitized traces were stored on disk for further analysis. Figure 6.14 compares a digitized trace of a Li ion-beam event with a light-pulser event. The rise times of the traces for the LED light pulser and the ion beam are clearly different and are 20 ns and 90 ns, respectively. The longer rise time in the case of a  ${}^6\text{Li}$  event is caused by the PWO scintillation mechanism and the integrating nature of the preamplifier.

The data acquisition (DAQ) was triggered when the beam fired the start detector in front of the carbon target. After applying the feature-extraction algorithm (Chapter 5), we extracted the energy and time information from the events. After applying the Moving-Window Deconvolution (MWD) to the signal and using the Moving Average (MA) procedure for smoothing, we took the maximum of the obtained pulse to obtain information

about the energy. The energy deposition for 2 AGeV  ${}^6\text{Li}$  ions in the 20 mm thick PWO crystal is about 180 MeV, calculated by the SRIM [64] software package. When the ion beam passes the carbon target, there is a probability to fragment the primary beam particles. In Figure 6.15, the energy deposition spectrum of different fragments is shown. The various peaks indicate the production of different lighter ions, such as protons and alpha particles,

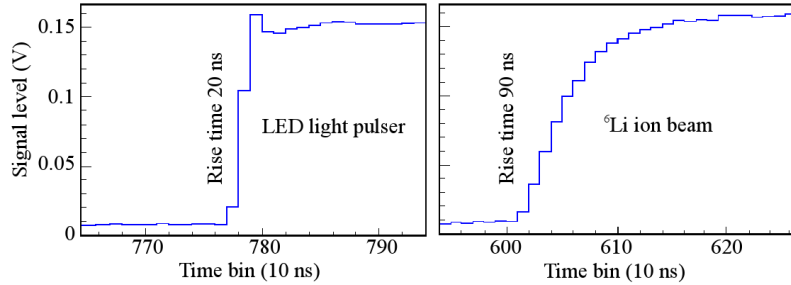


**Figure 6.14:** Measured pulse shapes of a LED light-pulser event (left) and a Li-ion beam-event (right). The increase of the rise time is due to the light production mechanism in the crystal.

by beam fragmentation, next to the Li ion signal. For the identification of the peaks we assume that the fragment velocity was the same as the velocity of the  ${}^6\text{Li}$  beam particles. According to the Bethe-Bloch [42] equation the deposited energy will vary with the charge number  $Z$  of the fragment as  $Z^2$  for the same fragment velocity. The peak position for  ${}^6\text{Li}$  ions is found at 102 mV, for alpha particles at 45 mV and for protons at 10 mV. Following the Bethe-Bloch equation the ratio of deposited energy for  ${}^6\text{Li}$  and alpha particles should be  $dE/dx_{^6\text{Li}} : dE/dx_{\text{alpha}} = (Z_{^6\text{Li}} / Z_{\text{alpha}})^2 = 2.25$  and according to the data in Figure 6.15 the ratio for the peak positions of  ${}^6\text{Li}$  and alpha particles is  $102 \text{ mV}/45 \text{ mV} \approx 2.27$ . Similarly, for  ${}^6\text{Li}$  and protons we obtain  $dE/dx_{^6\text{Li}} : dE/dx_{\text{proton}} = (Z_{^6\text{Li}} / Z_{\text{proton}})^2 = 9$  and according to the data in Figure 6.16 we find the ratio  $102 \text{ mV}/11 \text{ mV} \approx 9.3$ . Therefore, we may identify the peaks shown by the black (upper) line in Figure 6.15 as caused by protons, alpha particles and  ${}^6\text{Li}$  beam ions, respectively. The peak at 22 mV can be associated with twice the energy deposition of a proton. Around 55 mV we notice a shoulder which can be associated with a double hit of an alpha and a proton.

In order to confirm the nature of the peak at 22 mV (or at 55 mV) in the energy-deposition spectrum, the events with a more precisely defined time-stamp difference below 1 ns were selected, see Figure 6.16. In the resulting energy-deposition spectrum the peak around 22 mV (or 55 mV) is strongly suppressed, see Figure 6.15. Therefore, we conclude, that events producing this peak have a badly defined time correlation. This can happen e.g. for pile-up events, if simultaneously two protons (or a proton and an alpha particle) traverse the PWO crystal at different positions.

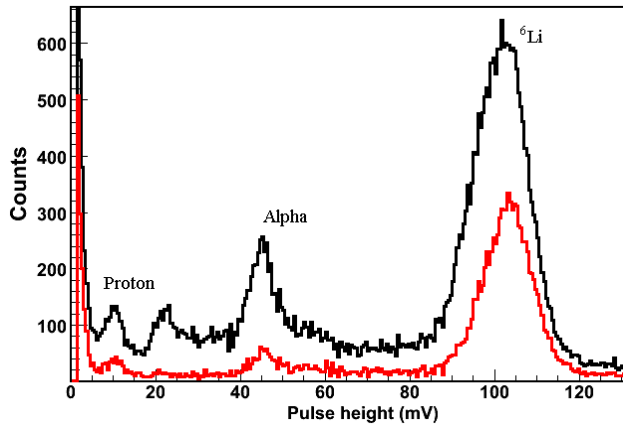


**Figure 6.15:** The energy deposition of 2 AGeV  ${}^6\text{Li}$  ions and beam fragment ions in the PWO crystal is shown by the black (upper) line. The red (lower) line shows the energy-deposition spectrum after the time-cut.

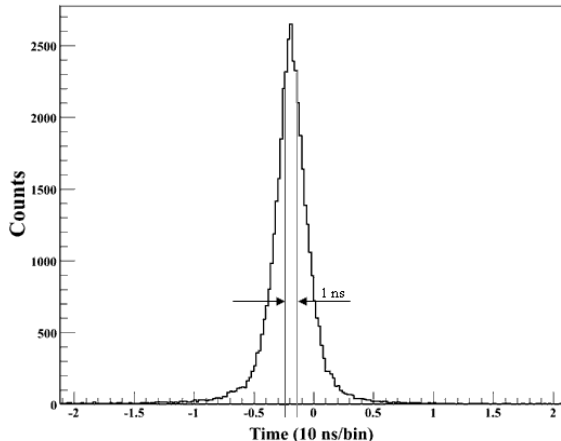


**Figure 6.16:** The distribution of time-stamp differences with vertical bars indicating the selected region of absolute time differences < 1 ns.

Figure 6.17 shows the correlation between the measured energy deposition in the PWO crystal and the deposited energy calculated using the SRIM software package [64]. This correlation was used as an energy calibration for the experimental setup. To obtain the time information, we used the digitally implemented CFT algorithm applied to the de-convoluted pulse. The time resolution is determined from the difference distribution of time-stamps of signals measured by two LAAPDs, which are coupled to both end faces of the PWO crystal. The time resolution becomes better than 1 ns for an energy deposition above 80 MeV, see Figure 6.18.

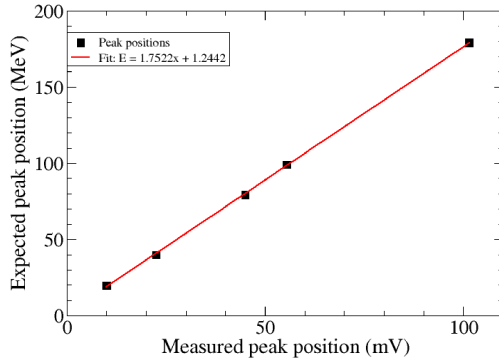


**Figure 6.17:** The calibration curve for energy deposition of the fragmented 2 AGeV  ${}^6\text{Li}$  ion beam impinging on the PWO crystal. The uncertainties for peak positions are smaller than the symbol size.

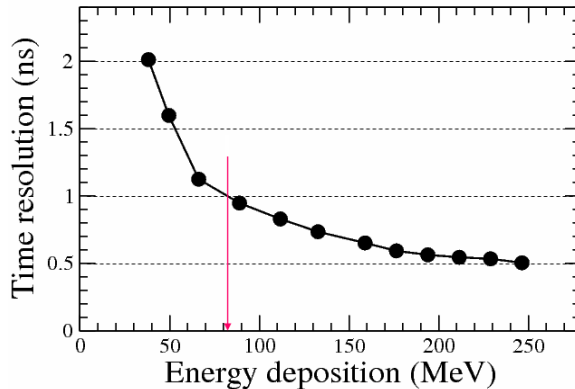


**Figure 6.18:** The dependence of the time resolution on energy deposition in PWO crystals. For energy deposition above 80 MeV the time resolution is less than 1 ns. The uncertainties in time resolution and energy deposition are smaller than the symbol size.

The time and energy resolutions measured for the Li ion-beam data were investigated for different sampling rates and resolutions of the SADC. Figure 6.19 shows the resulting energy and time resolutions for 100, 50 and 25 MHz sampling rates at 16-bit resolution, measured for 180 MeV energy deposition in the PWO crystal. The relative difference in the energy resolution at 100 and 50 MHz is about 0.9% and for the time resolution about 5%. However, comparing 50 MHz and 25 MHz sampling rates, the difference for the energy resolution increases to 13% and for the time resolution to 52%.

In order to study the influence of reduced bit-resolution on the precision of the time and energy information, we did investigations for 100 and 50 MHz sampling rates. Energy and time resolution were analyzed for 16, 14 and 12-bit resolutions. The obtained results are presented in Figure 6.20.

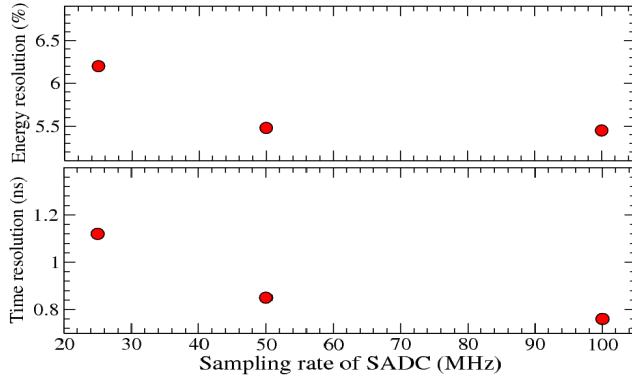


**Figure 6.19:** Energy and time resolution for 180 MeV energy deposited in the PWO crystal. The uncertainty in energy and time resolutions is smaller than the symbol size.

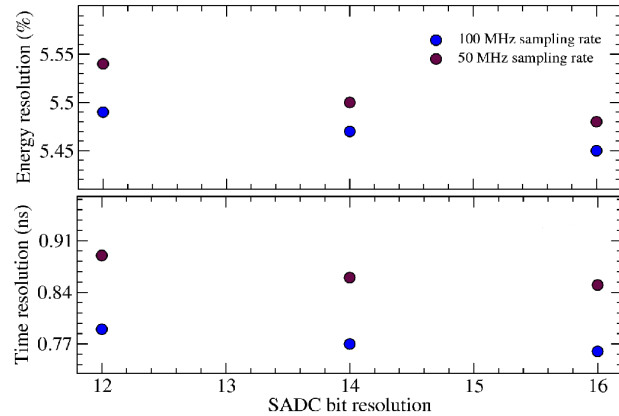


**Figure 6.20:** Energy and time resolutions for 180 MeV deposited energy of Li ions in a PWO crystal measured for 100 and 50 MHz sampling rates at different SADC bit resolutions. The uncertainty in energy and time resolution is smaller than the symbol size.

We observe only small differences in time and energy resolutions for 100 and 50 MHz sampling rates. By using an SADC with 14-bit instead of 16-bit resolution, the time and energy resolutions only slightly deteriorate. From these investigations we conclude, that 50 MHz sampling rate and 14-bit SADC resolution will be reasonable choices for the digitization electronics of the PANDA EMC.

## 6.3 Measurements with the EMC prototype

### 6.3.1 Proto60 setup

The Proto60 detector system consists of 60 PWO-II crystals and is a prototype of the PANDA Electromagnetic Calorimeter [7]. The mechanical structure is exactly the same as for one section of the Barrel EMC. The end face of each crystal is optically coupled to one  $10 \times 10 \text{ mm}^2$  LAAPD. Thin carbon fiber cases, called alveoli, are employed for holding groups of crystals together (Figure 6.21), fitting them to the preamplifier and preventing the brittle crystals in the calorimeter to receive mechanical strain. The surroundings of the crystal arrangement are foreseen with copper pipes for cooled alcohol flowing to allow the operation at a temperature of  $-25^\circ\text{C}$ . To prevent ice forming on the electronics the detector setup is continuously flushed with dry nitrogen. Together with the crystal and the attached LAAPD, the LNP preamplifier is placed in the cold part of the setup to minimize the electronic noise. To monitor the temperature stability the setup included 13 thermometers. During long measurement periods of several days the temperature variation remained in the range  $\pm 0.05^\circ\text{C}$  [7].



**Figure 6.21:** Left: Backside view of Proto60. There are 60 crystals, 3 groups of 4 crystals are covered by Al holders, 3 other groups of 4 are covered by a readout strip. Right: Photograph of carbon fiber alveoli (top) and a group of four crystals packed in reflective material (bottom) [7].

### 6.3.2 Experiment at the MAMI accelerator in Mainz

The performances of the readout of PWO crystals equipped with LAAPD sensor and LNP preamplifier was studied at the accelerator facility MAMI, Mainz University. The electron accelerator MAMI [65] consists of three cascaded racetrack microtrons with a 3.5 MeV injector linac, followed by a Harmonic Double Sided Microtron (HDSM). The maximum electron energy is 1508 MeV with a beam current of up to 100  $\mu\text{A}$ . The mono-energetic electrons from MAMI were guided on a Ni target (Figure 6.22) to produce bremsstrahlung radiation. Using a magnetic spectrometer to measure (tag) the momentum of the scattered electrons provided us with the energy of (tagged) photons up to a maximum photon energy of 1401 MeV with energy resolution 4 MeV [66]. The photon energy  $E_\gamma$  can be determined from the electron beam energy  $E_e$  and the energy  $E_{e'}$  of the scattered electrons

measured in the magnetic spectrometer:  $E_\gamma = E_e - E_{e'}$ .

In a first round of measurements, MAMI-C provided photon energies up to 1.4 GeV. Data were measured with 100 MHz sampling rate of the SADC and 10  $\mu\text{s}$  long preamplifier output traces were stored for the analysis. However, due to beam time constraints we were only able to gather data with low statistics at high energy. Therefore, a 2<sup>nd</sup> beam time was scheduled but the accelerator could only provide photon energies up to 0.6 GeV. In order to study the time resolution in the 2<sup>nd</sup> run, the photon beam was directed between two adjacent crystals. In this run we used SADC sampling rates of 100 and 50 MHz and we recorded 2  $\mu\text{s}$  long preamplifier output traces.

The signals from 16 selected tagger channels and from 23 detector crystals were connected to the data acquisition system (Figure 6.22). The tagger channels and their corresponding energy values are given in Table 6.1. The energy threshold for signals accepted by the data acquisition system was set  $3\sigma$  above the noise level where  $\sigma$  is the width of the noise level. The photon beam was hitting crystal number 35 as the “central crystal” (Figure 6.23). The signals from the tagger-channels were digitized by TDC units and the correspondingly filled histograms were used to monitor the energy distribution and the accumulated statistics (Figure 6.24). In Figure 6.25 calibrated single-crystal energy spectra on a logarithmic scale are shown for all crystals. When the photon beam perpendicularly hits the surface of one crystal, the photons initiate an electromagnetic shower that spreads over the surrounding modules. The deposited energy in the neighboring crystals depends on the photon energy and can be reduced due to dead material (for example Teflon foil) between the crystals.

Tagger channels	Energy (GeV) 1 <sup>st</sup> run	Energy (GeV) 2 <sup>nd</sup> run
1	1.44	0.686
2	1.36	0.651
3	1.26	0.602
4	1.16	0.579
5	1.06	0.509
6	0.96	0.443
7	0.86	0.387
8	0.76	0.339
9	0.66	0.269
10	0.56	0.201
11	0.46	0.152
12	0.36	0.107
13	0.26	0.094
14	0.16	0.084
15	0.12	0.062
16	not used	0.05

**Table 6.1:** Tagger channels and the corresponding tagged-photon energy values.

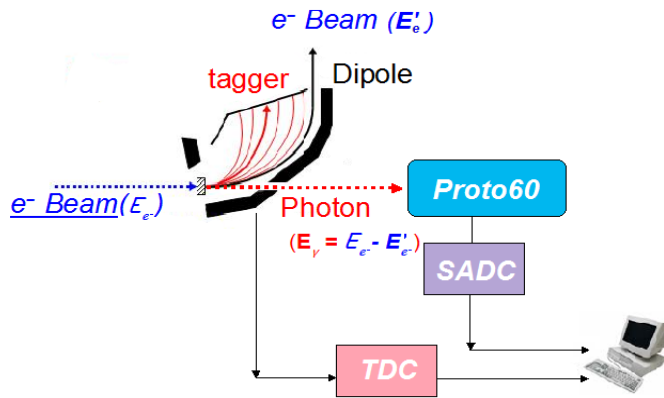


**Figure 6.22:** Experimental setup at the MAMI tagged-photon beam with Proto60 readout by Sampling ADC (SADC).

1	2	3	4	5	6	7	8	9	10
11	12	13	14	15	16	17	18	19	20
21	22	23	24	25	26	27	28	29	30
31	32	33	34	35	36	37	38	39	40
41	42	43	44	45	46	47	48	49	50
51	52	53	54	55	56	57	58	59	60

**Figure 6.23:** Crystal mapping for the Proto60 setup. For the data acquisition we only considered 23 crystals. Crystal number 35 was defined as the “central crystal”. For the determination of the cluster energy resolution the beam was centered on crystal #35 and for determining the time resolution the beam was guided between crystals 35 and 36.

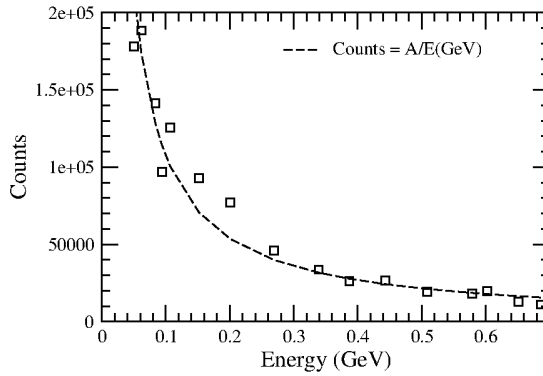


**Figure 6.24:** The tagged-photon event distribution as a function of the photon energy. The dashed line is a fit of the bremsstrahlung energy ( $E$ ) distribution with a function  $A/E$  and a fit parameter  $A = 10746 \pm 480$ .

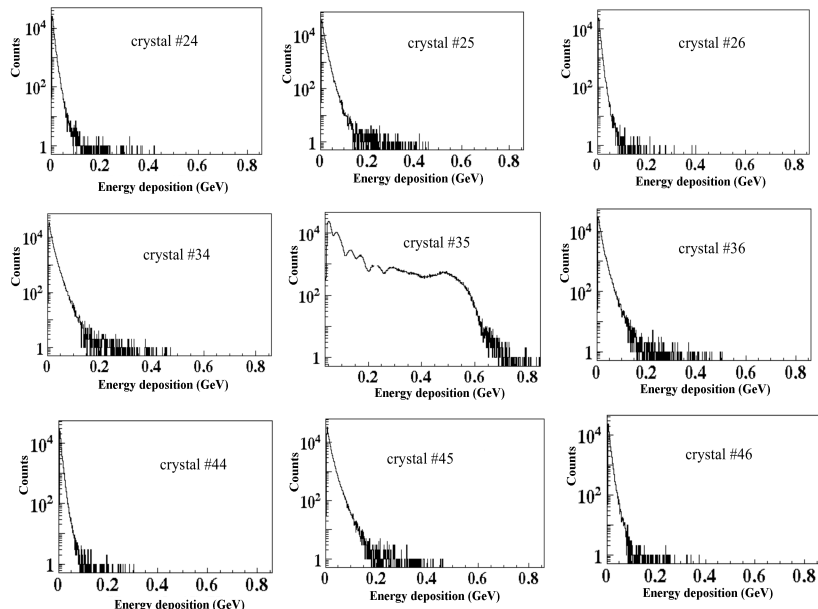


**Figure 6.25:** The distributions of tagged photon energy deposition on a logarithmic scale in a  $3 \times 3$  array of crystals with the beam centered on the middle crystal. The photon energies cover the bremsstrahlung spectrum in the range 0.05 - 0.685 GeV.

### 6.3.3 Readout Electronics of Proto60

For the data acquisition, we have used three STRUCK SIS3302 Sampling ADC units with 100/50 MHz sampling rate and 16-bit resolution and one CAEN v775AC TDC [67] module to obtain the time information from the tagger signals (see Figure 6.22). For triggering the data acquisition system we used the coincidence between the central crystal signal and the logic OR output signal of the 16 tagger channels. Figure 6.26 shows the scheme of the applied readout electronics.

The coincidence between the central crystal signal and the logic OR output signal (NIM signal from a coincidence module) of the 16 tagger channels is given as a trigger signal to the NIM-ECL converter to provide the signal for the trigger module Trivia (with ECL input) for the data acquisition system. The trigger module is connected via the trigger bus and takes care of the correct inhibition of ADC gates and TDC starts during the conversion and read-out period as well as the collection of corresponding sub-events. Another NIM-ECL output signal is fed to a timing filter amplifier (TFA) to gather timing information and still another is provided to the logic splitter FAN-IN-FAN-OUT. The logic splitter provides the Sampling ADC and the TDC with the identical stop signal. The first SADC clock was initialized via software to operate at 100 MHz or 50 MHz sampling frequency and the other two SADCs were synchronized according to the first SADC. The preamplifier signals from 23 crystals were connected to SADC channels and the remaining SADC channel was used to digitize the TFA signal for timing information. The energy and time information of each scintillator crystal together with the timing response of the relevant tagger channels were recorded event-by-event to data storage for further off-line analysis.

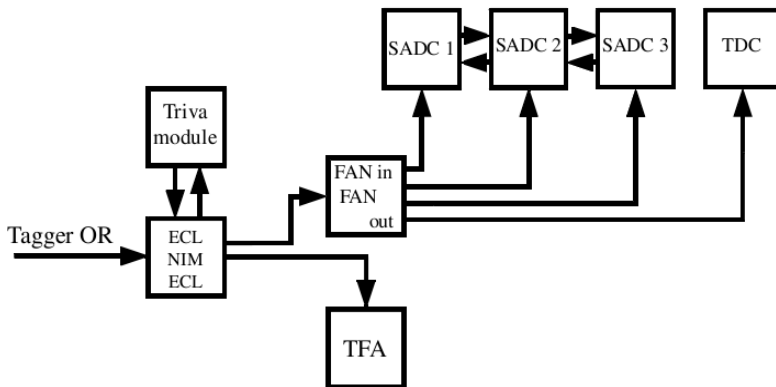


**Figure 6.26:** Scheme of the readout electronics of the Proto60 detector setup.

### 6.3.4 Cosmic muon calibration

To calibrate the measured energy spectrum we have used the cosmic muon energy deposition in PWO crystals. According to the information from the Particle Data Group [68] the mean energy loss of minimum ionizing particles in 1 cm PWO material is 10.2 MeV and this is to a good approximation valid also for cosmic muons. The calibration was performed

at a crystal temperature of -25 °C and at the same LAAPD gain as applied during the measurements with tagged photons. The Landau-fit tool provided by the ROOT [69] software package was used to associate the mean energy deposition of cosmic muons with the most probable value of the Landau distribution.

For the energy calibration, we have used two kinds of geometry of the Proto60 setup: the horizontal and the vertical positions as shown in Figure 6.27 and Figure 6.28, respectively. In the horizontal position, the cosmic muons traverse on average a length of 2.4 cm in PWO and the corresponding mean energy deposition is 24.5 MeV. For this measurement we placed a thin plastic scintillator ( $2 \times 45 \text{ cm}^2$ ) on top of the setup and we used as trigger signal the coincidence between this plastic scintillator and the row of crystals below. For the vertical position of the setup (Figure 6.28) the path length of cosmic muons in PWO is about 20 cm and the energy deposition is approximately 204 MeV. For this measurement the data were taken for 10 days. In this case we used as trigger signal the coincidence between a wide plastic scintillator and an array of  $5 \times 5$  crystals which were covered by the scintillator. The energy deposition was determined from the amplitude of the MWD-filter signal, called the MWD amplitude. For the vertical position of Proto60 the obtained spectrum of energy deposition is shown in Figure 6.29 and the spectrum for the horizontal position with Landau fit is shown in Figure 6.30.

The cosmic muon energy-deposition spectrum for the horizontal (Figure 6.27) and the vertical setup (Figure 6.29) are clearly different. As mentioned before, cosmic muons passing through the full length of the crystal must deposit about 204 MeV, but this is true only for exactly vertical incidence on the front face. In order to impose this “vertical selection” condition, events were selected in which only a single crystal was giving a signal and none of the neighboring crystals. The corresponding energy deposition spectrum is shown in the bottom panel of Figure 6.29. For the large length that the photons travel through the crystal in this case, a Gaussian distribution is most appropriate. The Gauss fit is shown in Figure 6.29.

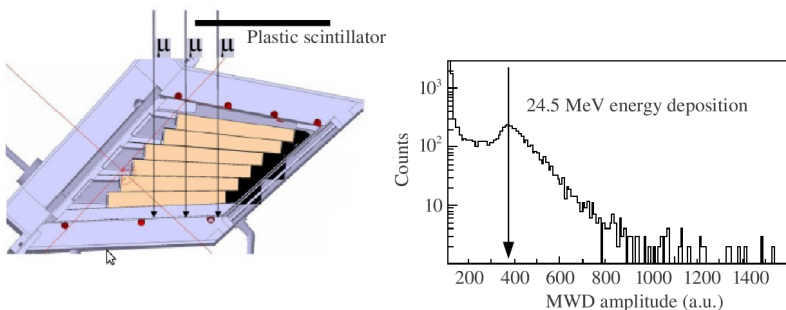


**Figure 6.27:** The Proto60 setup in horizontal position and the corresponding cosmic muon energy deposition spectrum with the peak value indicated by the vertical arrow. For this measurement, a thin plastic scintillator ( $2 \times 45 \text{ cm}^2$ ) was placed on top of the setup to derive a trigger signal from the coincidence with the row of PWO crystals below. The MWD amplitude corresponds to the pulse maximum of the MWD-filtered signal.

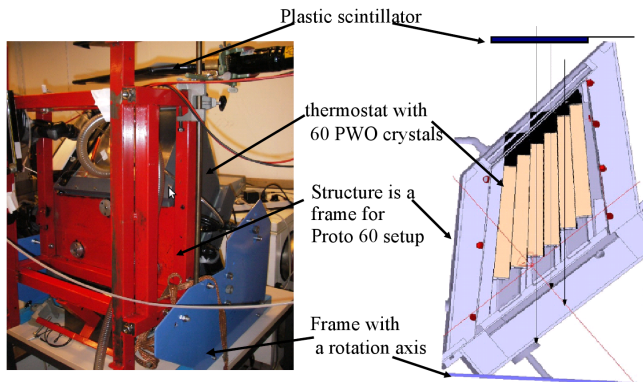


**Figure 6.28:** Left: photograph of the Proto60 setup in vertical position. The red-colored structure is a frame for holding the Proto60 setup and the blue frame houses the rotation axis. The gray box is the thermostat containing the 60 PWO crystals. The black-colored plate above the red frame is a plastic scintillator panel ( $20 \times 45 \text{ cm}^2$ ), used as a trigger. Right: Sketch of the Proto60 setup in vertical position.

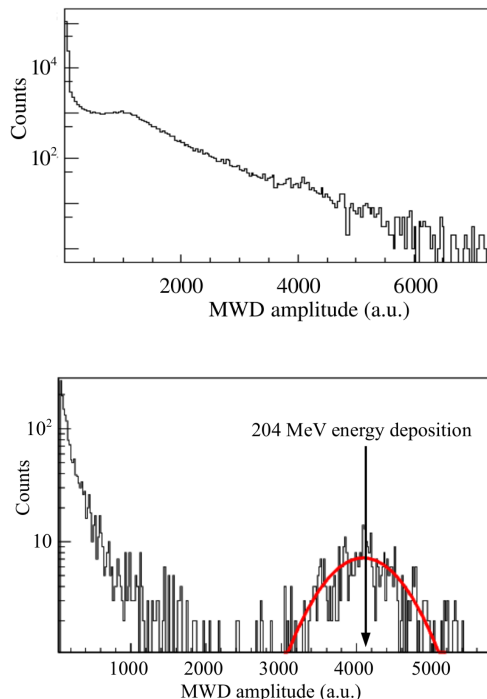


**Figure 6.29:** The cosmic muon energy-deposition spectrum for the vertical position of the setup. Top: the raw spectrum; Bottom: the spectrum after applying the “vertical selection” condition. A clear peak containing 422 events arises with a mean value of the Gauss fit at 4129 units; this value is associated with the energy deposition of 204 MeV.

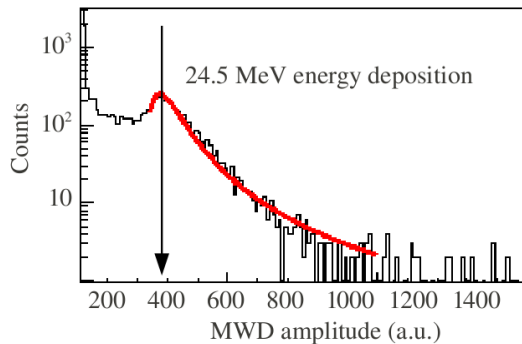


**Figure 6.30:** The cosmic muon energy-deposition spectrum as shown in Figure 6.27, but here with the Landau fit function for the horizontal detector position. From the most probable value of the Landau fit we obtain that the mean energy deposition of 24.5 MeV corresponds to 392 units in the MWD amplitude.

Using the two calibration points obtained in Figures 6.29 and 6.30 we can derive the calibration function for any of the 23 crystal detectors. Figure 6.31 shows the calibration of the MWD amplitude  $m$  in units of energy deposition for the central crystal.

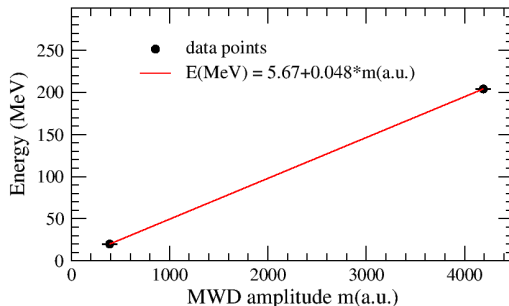


**Figure 6.31:** The energy calibration curve for the central crystal. The error bars given for the x-axis are determined from the widths of the corresponding amplitude distributions.

### 6.3.5 The results with high-energy photons

**The photon response function and cluster energy resolution:** During the measurements at MAMI, the tagged photon beam providing a bremsstrahlung spectrum of energies was directed to the central crystal (number 35) and simultaneously the signals of 23 crystals and 16 tagger channels were recorded. If the energy of the incoming photon is high enough it can cause an electromagnetic shower in the central crystal and the surrounding crystals. For the determination of the photon energy response or the line shape, we have to collect the sum of energy depositions in all neighboring crystals. The detector response for

low energy photons or gamma rays is well described by a Gaussian distribution [70]. However, for high-energy photons the shape of the response function may be different due to the photon leakage from the crystal array. Therefore, to determine the photon response for different incident photon energies, we study the energy deposition in a  $3 \times 3$  array of crystals. An example of photon responses for different incident photon energies is plotted in Figure 6.32.

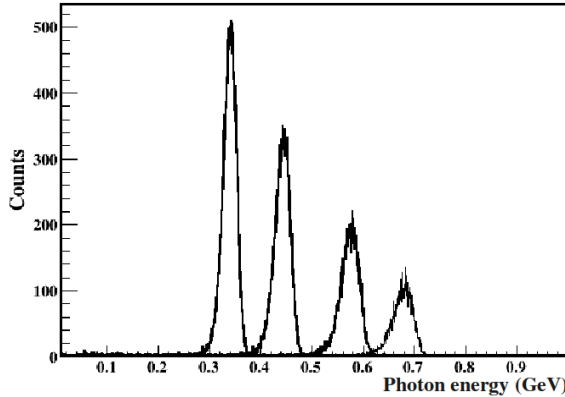


**Figure 6.32:** The photon response measured for a  $3 \times 3$  array of crystals for different incident photon energies of 0.39, 0.44, 0.6 and 0.69 GeV.

The experimental response function has been parameterized by two analytical functions valid below and above the most probable energy  $E_{peak}$  [71]:

$$y = \begin{cases} N \cdot G, & E > E_{peak} \\ N \cdot \left( G + \exp\left(-\frac{E - E_{peak}}{\lambda}\right) \cdot (1 - G) \right), & E \leq E_{peak} \end{cases}$$

where

$$G = \exp\left(-\frac{4 \cdot \ln 2 \cdot (E - E_{peak})^2}{FWHM^2}\right)$$

The parameter  $N$  is used for the normalization to the peak height and two different width parameters are introduced. The width  $FWHM$  of the Gaussian describes the high-energy side of the peak and  $\lambda$  describes the low energy tail.  $E_{peak}$  is the most probable detected photon energy. Figure 6.33 illustrates the quality of the analytical expression for a photon energy of  $E_\gamma = 0.685$  GeV.

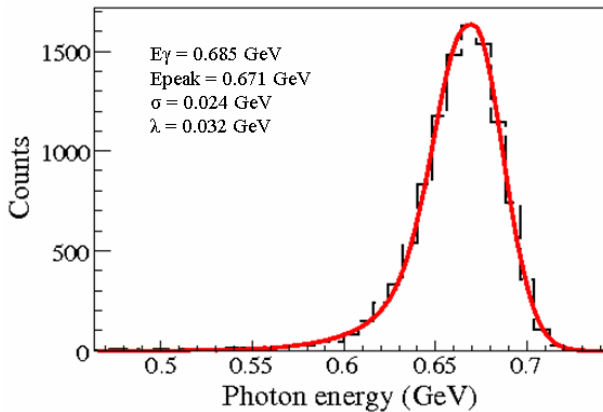


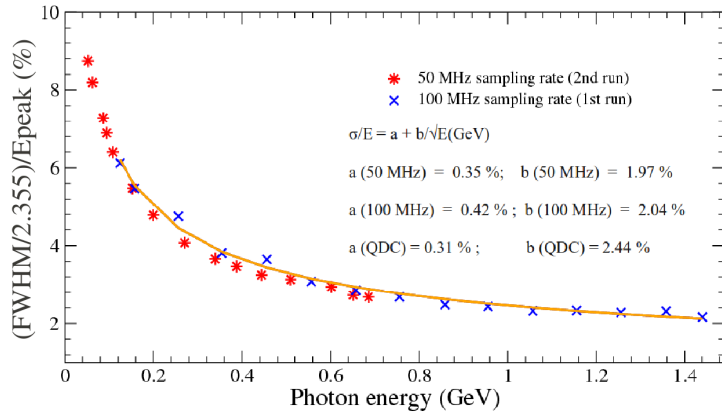
**Figure 6.33:** Experimental line shape measured at the incident photon energy  $E_\gamma = 0.685 \text{ GeV}$ .

For the determination of the energy resolution we have used the parameters of the response function after fitting. The observed energy resolution is calculated from the Full Width at Half Maximum ( $FWHM$ ) of the measured line shape:

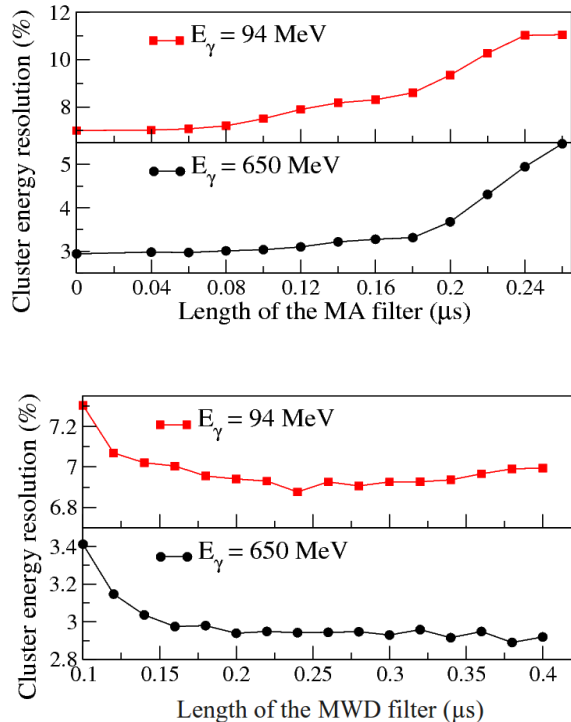
$$\sigma = \frac{FWHM}{2.355}$$

and the relative detector energy resolution  $\sigma/E_{\text{peak}}$  is calculated. Figure 6.34 presents the dependence of the energy resolution on the tagged photon energy for the Sampling ADC readout at 100 MHz and at 50 MHz sampling frequency. We observe that the energy resolution is nearly the same for 50 and 100 MHz sampling rates. From this observation, we conclude that we safely may apply the SADC with 50 MHz sampling rate and gain power consumption and digitization time at a reduced cost compared to a SADC with a higher sampling rate. The obtained result in energy resolution also compares well with the result obtained with a conventional charge integrating ADC [72]. The energy resolution as a function of the photon energy could be fitted with constant term and stochastic term, while the noise term had no influence. Figure 6.35 demonstrates the energy resolution analyzed for different smoothing length  $L$  (Moving Averaging length) and differentiation length  $M$  (Moving-Window Deconvolution length). The energy resolution has reached its optimum value at 200 ns differentiation time or MWD filter length. From the analysis of Proto60 data we concluded that optimal parameters for digital filters are  $M = 300 \text{ ns}$ , to be on the safe side, and  $40 \text{ ns} \leq L \leq 160 \text{ ns}$ , depending on the count rate due to changes of the pulse width.

**Time resolution study with Proto60:** To study the timing performance of the readout electronics in a realistic experimental situation we had used the 2 AGeV Li beam and the single crystal setup (see section 6.2.2). During that experiment, we had used a straight crystal, which has a different geometry than required in the TDR [7]. In addition, the covered energy range was not wide enough. Here we study the timing performance in a wider energy range of tagged photons with Proto60.

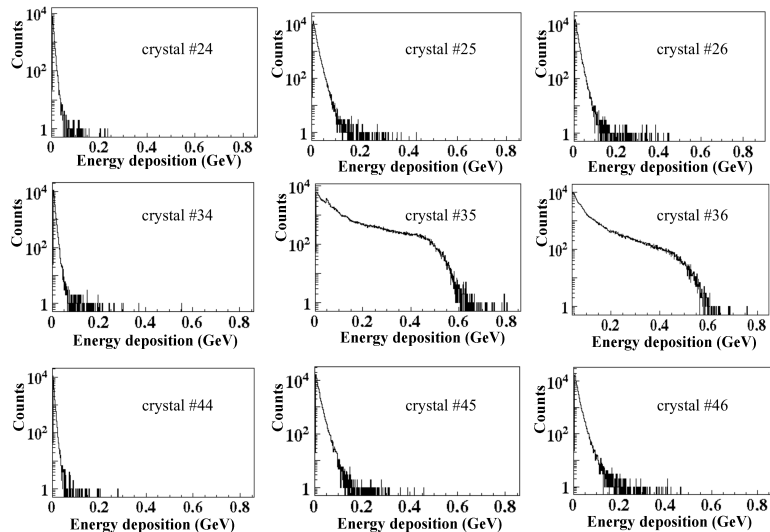


**Figure 6.34:** Energy resolution for a  $3 \times 3$  PWO crystal array as function of the tagged photon energy. The solid (yellow) curve indicates the result obtained with conventional QDC readout. The uncertainty in energy resolution is smaller than the symbol size.



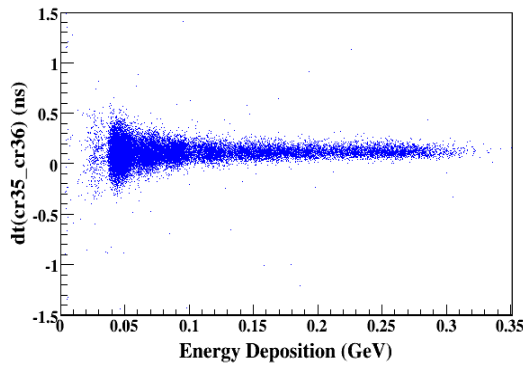
**Figure 6.35:** Cluster energy resolution for different lengths  $L$  of the MA filter (top) and  $M$  of the MWD filter (bottom) at low and high photon energy [56].

To study the timing performance of Proto60, the beam was directed between the central crystal and one of its neighboring crystals. According to the crystal map (Figure 6.23) the crystals number 35 and 36 receive about an equal energy deposition. Those two channels triggered the SADC readout. In order to avoid time walk, the corresponding preamplifier output signals were connected to the same SADC (channel 1 and 8 of the 1<sup>st</sup> SADC). Figure 6.36 shows the energy distributions measured in the 9 channels of the 3×3 crystal matrix.

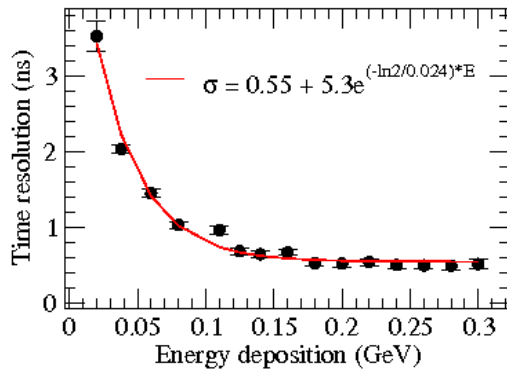


**Figure 6.36:** The distributions of tagged photon energy deposition on a logarithmic scale in a 3×3 array of crystals with the beam centered between crystal number 35 and 36. The photon energies cover the bremsstrahlung spectrum in the range 0.05 - 0.685 GeV.

To determine the time resolution for each tagged photon energy, we fill a two dimensional histogram (Figure 6.37) with the energy deposition on the horizontal axis and the difference of time stamps for crystal 35 and 36 on the vertical axis. For the calculation of the time resolution, we applied the condition that the energy depositions in both crystals for one event should not differ by more than 10%. This condition ensures that the results of both detectors are of comparable quality. From Figure 6.37 we extract time difference distributions in bins of deposited energy. From these distributions, we determine the time resolution in bins of energy deposition as  $\sigma/\sqrt{2}$  of a Gauss fit, as plotted in Figure 6.38. The time resolution is below 1 ns, when the energy deposition is higher than 80 MeV. The obtained time resolution is better than the sampling period of the SADC and comparable with the result obtained with the Li ion beam.



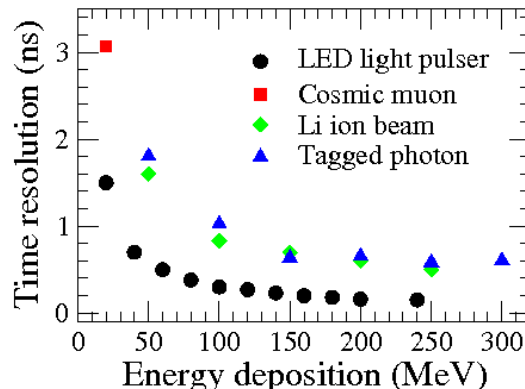
**Figure 6.37:** Difference in time stamp between the central crystal and its neighboring crystal for different values of the energy deposition.



**Figure 6.38:** Time resolution determined between two adjacent crystals receiving about an equal energy deposition, as a function of the energy deposition [56].

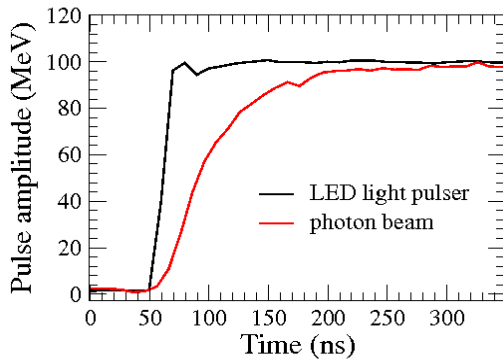
## 6.4 GEANT simulation study of timing properties

For optimum background reduction and clean event definition the best possible time resolution should be achieved. The time resolution was investigated with the LED light pulser, with cosmic muon energy depositions, with the Li ion beam, and with high-energy tagged photons. Figure 6.39 presents the dependence of the time resolution on the energy deposition for all different measurements (see Figures 6.2, 6.18 and 6.38). From this figure, we notice that there are large discrepancies between the time resolutions measured with the LED light pulser and the ion beam or the tagged photon beam. For instance, at the energy deposition of 100 MeV we observe a time resolution of 0.24 ns for the LED light pulser, and 0.8 ns and 1 ns for the ion beam and the high-energy photon beam, respectively. The time resolution  $\sigma_{time}$  is dependent [43] on the width  $\sigma_n$  of the noise level and the slope  $dV/dt$  of the signal as  $\sigma_{time} = \sigma_n / |dV/dt|$ . From this equation, we can see that the time resolution may get worse due to two reasons: an increasing noise level and a changing slope of the signal. In the experiments with the LED light pulser, the photon beam, and the ion beam, the main source of noise was the preamplifier. For all the measurements, we used the same type of preamplifier and the estimated noise level was about 1.4 MeV. The slope of the signal is different between a pulse generated by the LED pulser and that generated by the scintillating process in the crystal. To investigate the corresponding influence on the time resolution we performed GEANT simulations [73] and experiments with the LED light pulser.



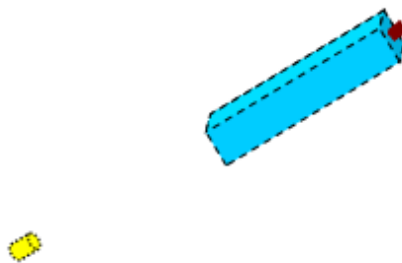
**Figure 6.39:** The dependence of the time resolution on the energy deposition in a single PWO crystal bar for different measurements. The uncertainty in time resolution is smaller than the symbol size.

Figure 6.40 shows the recorded trace from the charge-integrating preamplifier for a 100 MeV photon hitting the PWO crystal and, for comparison, the trace obtained with the LED light pulser. The rise time of the signal is about 100 ns for the photon beam and about 10 ns for light from the LED light pulser.



**Figure 6.40:** The recorded traces from a charge-integrating preamplifier for a 100 MeV photon entering and the LED light pulser injected to the PWO crystal, respectively.

In order to understand, why the pulse rise time is getting longer in the real case for the ion beam or the photon beam, GEANT simulations were studied for 1, 10, 100 and 1000 MeV incident photons on a PWO crystal with dimensions  $2 \times 2 \times 20 \text{ cm}^3$  (see Figure 6.41). The beam source was placed at a distance of 0.5 m from the front face of the PWO crystal. Photons with high energy hit the front face of the PWO crystal bar. The main light-transport properties as refraction index, density, energy of scintillation light and decay time of the PWO crystal are introduced to enable the realistic generation of scintillation light. The decay time of scintillating centers for PWO material was introduced into the simulation [7]. However, the exact value of this decay constant is not known. Therefore, this constant was considered as a variable that can be adjusted in order to reproduce the pulse-shape produced by the PWO crystal. The photo sensor is attached at the end face of the crystal. The arrival time of optical photons detected by the photo sensor is calculated. Figure 6.42 shows the arrival time distributions for different decay times at 100 MeV incident photon energy.



**Figure 6.41:** The geometry adopted for GEANT simulations to study the arrival time of optical photons at the LAAPD light sensor. The photon source (yellow dotted line) is placed at a distance of 0.5 m from the front face of the PWO crystal (blue dashed line) and the optical photons are detected at the light sensor (red).

The number of scintillation photons produced with decay time  $\tau$  at time  $t$  is described by the exponential decay law:  $N = N_0 e^{-t/\tau}$  with  $N_0$  the number of scintillation photons at the time

$t = t_0$  when the high-energy photon hits the crystal. From the generated arrival time distributions in Figure 6.42 we can determine the inverse slope parameters  $-0.19 \text{ ns}^{-1}$ ,  $-0.064 \text{ ns}^{-1}$ , and  $-0.029 \text{ ns}^{-1}$ , respectively, and calculate the effective decay times  $5.3 \text{ ns}$ ,  $15.6 \text{ ns}$ , and  $34.5 \text{ ns}$ , respectively. The calculated effective decay times are slightly larger than the simulated decay times used to generate the scintillation photons in the crystal. After emission, the scintillation photons may undergo multiple reflections in the crystal, which leads to larger effective decay times. The simulation was repeated for different PWO crystal decay times and different photon energies. To study possible differences between the response for various energies and for different decay times, the cumulative distribution of the number of photons as a function of the arrival time of optical photons was generated and normalized to 1 for asymptotic light collection times. This distribution represents the output signal after the charge-integrating preamplifier. The cumulative distributions for different incident photon energies and decay times are shown in Figure 6.43.

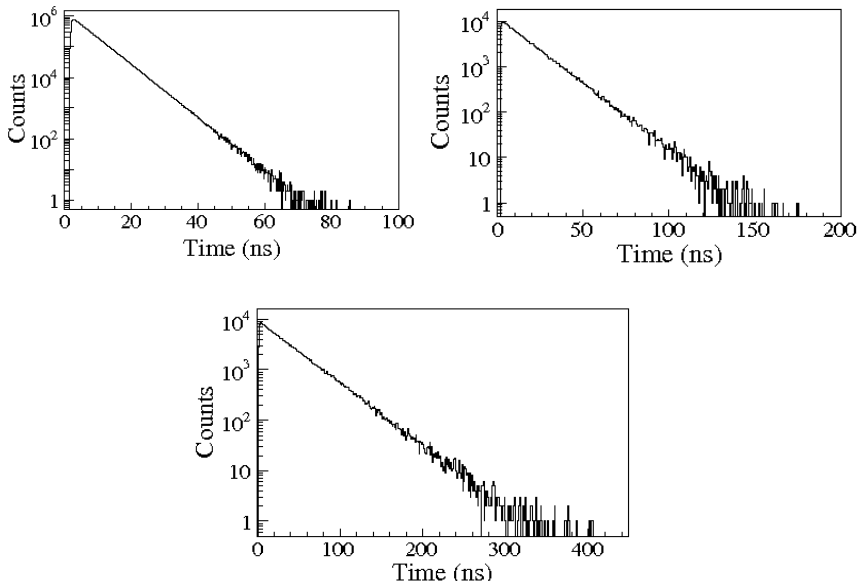


**Figure 6.42:** The result of GEANT simulations for 100 MeV incident photon energy. The arrival time distribution of optical photons are shown for different decay times [7] of the PWO crystal: 5 ns (top left), 15 ns (top right), 30 ns (bottom).

From the top figures one clearly recognizes, that the signal rise time slows down due to the scintillation mechanism. From the top right figure we can notice, that the slope of the signal rise time is getting wider due to longer decay times of the scintillation process in the crystal. To get approximately the same slope of the signal as for the measured pulse, the decay time had to be set to 30 ns. The resulting trace compares well in shape (see Figure 6.43 bottom right) with the trace from the LNP preamplifier for a 100 MeV photon impinging on the PWO crystal. The signal rise time is about 100 ns. From the shape of the additional curves for different decay times we conclude a sensitivity of better than  $\pm 5 \text{ ns}$  for the determination of the decay time of scintillation light inside the crystal. Recently, for PWO material decay times of 30 ns and 10 ns with relative yields of 80% and 20%,

respectively, were measured [74].

Once we can reproduce the pulse shape of the preamplifier signal, it is possible to check how stable the shape is, i.e. whether it depends on the incident photon energy. The simulation was repeated for low and high energies. The curves are almost overlapping and only small differences are seen in the zoom of a particular region, which is used to generate a time-stamp of the pulse, shown in Figure 6.43 bottom left.

It has been shown that for higher energies the time resolution is improving. However, the simulated distributions shift to longer collection times for higher energies. At a cumulative probability of 45%, the time shift amounts to about 500 ps for incident photon energies between 1 MeV and 1000 MeV. At energies below 10 MeV the shifts amount to 500 ps and the estimated time resolution is 5.8 ns. The time resolution is much larger than the shift of 500 ps, which is, therefore, negligible.

From the GEANT simulation, we understand that the rise time is getting longer due to the scintillation mechanism of the crystal. To confirm that the time resolution is getting

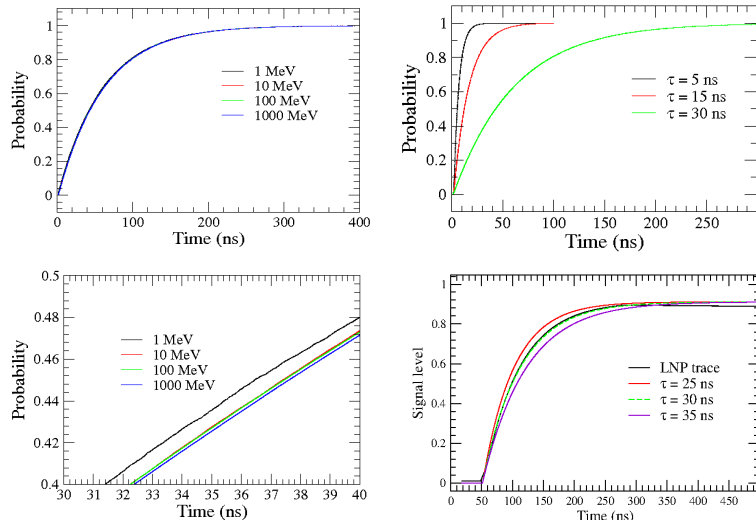


**Figure 6.43:** The cumulative distributions of the number of photons as a function of the arrival time of optical photons. Top left: the normalized distributions for different photon energies; Top right: the normalized distributions for different decay times at 100 MeV incident photon energy; Bottom left: the zoomed view of one part of the distributions for different photon energies; Bottom right: the recorded trace from the LNP preamplifier (black line, almost overlapped by the green dashed line for 30 ns) and the cumulative simulated distributions for 100 MeV energy deposition with different decay time constants.

worse due to rise time variations we performed another test experiment with the LED light pulser.

We note that the CFT method, used for the time stamp determination, is by design stable against amplitude variations. The signals were shaped after the LNP output by a filter network with different time constants. By varying the time constants, we observed that the time resolution deteriorates when the rise time is getting longer. Figure 6.44 shows the scheme of the electronics to study the influence of the pulse shape on the time resolution.

The signal from both LNP preamplifiers were shaped by the filter network and different rise times could be applied for both signals simultaneously. The pulse amplitude was 280 mV (equivalent to 300 MeV energy deposition).

Figure 6.45 shows traces with different rise times (top) and the corresponding graph of the time resolution as a function of the rise time (bottom). The time resolution is getting worse due to the slow rising edge of the pulse.

For a rise time of 100 ns, we obtain a time resolution of about 660 ps. This observation is in qualitative agreement with the result obtained for high-energy photons: From Figure 6.38 we estimate a time resolution of ~600 ps at 300 MeV energy deposition and a signal rise time of ~100 ns.

The experiment with the LED light pulser thus confirms that the observed discrepancies in time resolution for different light sources are caused by variations in signal rise time.

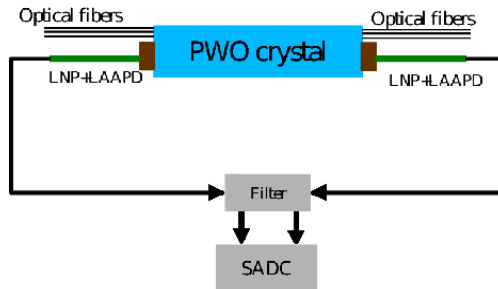


**Figure 6.44:** The scheme of the experimental setup to study the degradation of the time resolution due to rise time variations of the preamplifier pulse.

## 6.5 Conclusion

In this chapter, the performance of the PANDA EMC front-end readout system is investigated by applying the feature-extraction algorithm. Three different test measurements and their analysis results were presented.

The measurement with LED light pulser has shown that the time resolution improves for higher values of the collected charge at the LAAPD. The achieved time resolution is about 200 ps. A linear correlation was observed between the time values determined by the SADC using the CFT method and by the TDC. The precision of the time determination methods were studied for 50 MHz and 100 MHz sampling frequency and no significant differences were observed.

The performance study was done with a high-energy Li ion beam. The determined time resolution becomes better than 1 ns for an energy deposition above 80 MeV. The investigations were performed with different sampling frequencies and bit resolutions of the SADC. It was concluded that the 50 MHz sampling frequency and 14-bit SADC resolution are recommended choices for the digitizer of the PANDA EMC for the crystals equipped with LAAPD photo sensors.

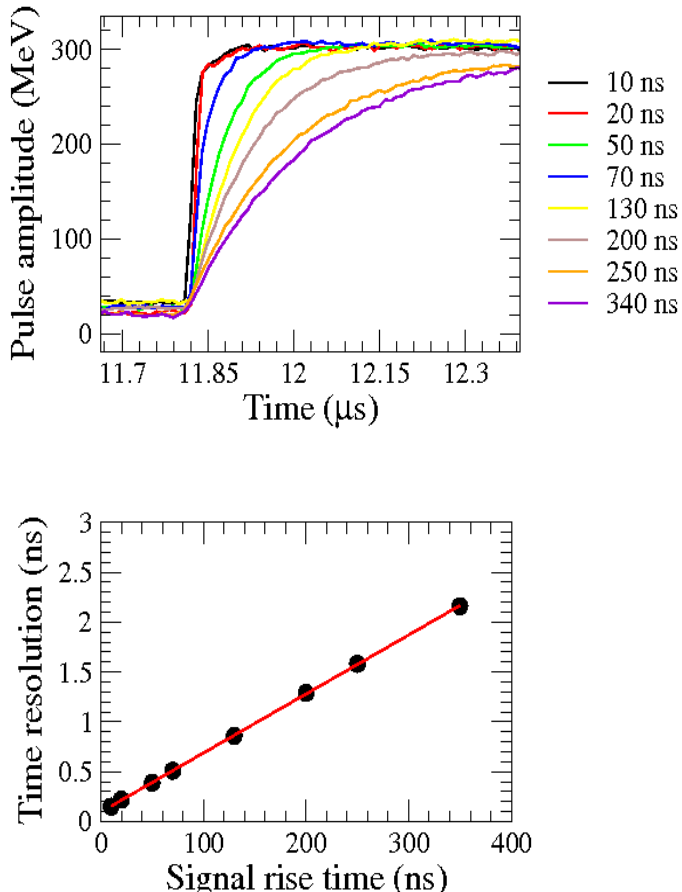


**Figure 6.45:** Top: LNP signal shapes for different rise times. Bottom: Dependence of the time resolution on the signal rise time. The time resolution gets worse due to the slow component on the rising edge of the pulse. The uncertainty in time resolution is smaller than the symbol size.

The performance of the readout electronics was further studied with the prototype of the PANDA EMC in a wider energy range with tagged photons. The energy depositions in a  $3 \times 3$  array of PWO crystals were investigated. The analysis was done again for 100 and 50 MHz sampling frequency of the SADC. The energy resolution is nearly the same for both sampling frequencies. The determined energy resolution was 2.4% at 1 GeV. The obtained result in energy resolution compares well with the result obtained with a conventional charge integrating ADC. The Technical Design Report for the PANDA EMC [7] requires that the constant term in the energy resolution  $a \leq 1\%$  and the stochastic term  $b \leq 2\%$ . The test results for the prototype of the PANDA EMC fulfill these requirements of the TDR by employing a charge-integrating preamplifier and SADC digitizer with the application of the feature-extraction algorithm. The timing performance was investigated in a wider energy

range. The achieved time resolution was below 1 ns when the energy deposition is higher than 80 MeV. The obtained results are in good agreement with the results obtained with the ion beam.

In order to understand the discrepancy in the time resolutions measured with the LED light pulser and for the ion beam or the tagged photon beam, systematic tests with the LED light pulser and GEANT simulations were performed. Due to the scintillation mechanism in the PWO crystal the slow signal component is enhanced in the rising edge of the signal. The arrival time of photons seen by the LAAPD was estimated to be longer than 100 ns. It was confirmed that the reason for the discrepancy in the measured time resolution for LED light pulser and photon or ion beams is the slower signal rise time due to the scintillation process.

---



## 7. Implementation of feature-extraction algorithm in FPGA

The feature-extraction algorithm was developed for processing of signals from the front-end electronics of the PANDA EMC. The results discussed in Chapter 6 were obtained by an off-line data analysis, where the feature-extraction algorithm written in C++ code was applied to the digitized values of the analog preamplifier (shaper) signal-trace.

During the experiment, the on-line information on energy and time of the current event is crucial for making decisions on storing or discarding the event. For this purpose the feature-extraction algorithm was also developed in VHDL (Very high-speed integrated circuits Hardware Description Language) code suited for the 100 MHz and 16-bit commercial Sampling ADC (SADC). This VHDL code was implemented into the Field Programmable Gate Array (FPGA) of the Xilinx family on the SIS3302 SADC. The performance of this FPGA implementation of the feature-extraction algorithm was tested on a Xilinx Spartan Development Board.

The chapter starts with a short introduction to the widely used FPGA circuit. Then the hardware of the Xilinx Spartan Development board will be briefly described and the block diagram of the signal processing implementation will be discussed. Thereafter the results of the on-line data processing, obtained with LED light pulser signals, will be presented. The results are compared with the results of the off-line (software) signal processing. Finally, the performance of the on-line pulse amplitude detection and the determination of the time resolution obtained with cosmic muons are shown.

### 7.1 Signal processing

Signal processing methods have been applied for a long time to transform or manipulate analog or digital signals. The Digital Signal Processing (DSP) integrated circuit is found in many applications, e.g. in: data communications, speech, audio, biomedical signal processing, instrumentation and robotics [75].

Since 1970, the development of programmable digital signal processors has started to accelerate the digital signal processing. One of the members of the programmable family is the FPGA developed in the beginning of 1990 [76, 77]. The FPGA is a semiconductor device that can be programmed.

Xilinx and Altera have become worldwide the main manufacturers of FPGAs due to flexibility, DSP libraries, and simple hardware development tools. Xilinx offers two different families of FPGAs, the Spartan and the Virtex series FPGAs. The Virtex FPGA has a high speed [76] but also a high price due to the high density of the logic blocks (see next section) and the large memory compared to the Spartan FPGA.

The SIS3302 SADC contains five Spartan FPGAs. The Spartan FPGA belongs to the 5<sup>th</sup> generation of the Xilinx family. The family consists of eight members offering densities ranging from 50 000 to five million system gates [78].

---

## 7.2 Xilinx Spartan-3A development board

In order to test the feature-extraction algorithm and its proper implementation in VHDL code, we first used the Xilinx Spartan-3A development board which contains a Xilinx Spartan 3 XC3S700 AN FPGA [78]. Communication with this test board was enabled by its RS-232 serial port for data input/output. Figure 7.1 shows a photograph of this board.

The Xilinx Spartan-3A FPGA is built of five programmable functional elements: configurable logic blocks (CLBs), input/output blocks (IOBs), block random access memories (RAMs), dedicated multipliers with two 18-bit complement (bitwise) operation and digital clock managers (DCMs).

The FPGA is an array of CLBs, which provide the user with the complete control over the functionality of the FPGA. Using a combination of CLBs in the FPGA will allow the user to program a gate with varying inputs, outputs and logic. The CLB is composed of look-up table (LUT), multiplexer (MUX) and 175 shift registers [78].

LUTs are used to implement function generators in CLBs. Four independent inputs are provided to each of two function generators which are used to realize Boolean functions.

The IOBs represent the physical pins of the FPGA and they are programmable to configure the interconnections of CLBs. For the implementation of the feature-extraction algorithm we used 232 IOBs out of 333 available, thus there is still room for extensions and refinements.

The Xilinx FPGA has an on-chip memory, called block RAM, up to 10 Mbits in 36 kbit blocks.

Digital clock managers (DCMs) provide advanced clock capabilities, which can eliminate a system clock skew. This feature eliminates a clock-distribution delay and improves the system performance [78].

The multipliers are located adjacent to the block RAM, making it convenient to store inputs in the block memory. The multipliers in the Xilinx Spartan-3A FPGA family are fast and efficient enough to implement a signed or an unsigned multiplication, basically a shift-add operation, with a precision up to 18 bits.

The Xilinx Spartan-3A development board has four binary switches, which are marked in the lower right corner of Figure 7.1. The switches allow to select a 16-level setting-word and are used to set different modes (see Table 7.1) of operation of the feature-extraction algorithm.

## 7.3 VHDL coding of the feature-extraction algorithm

The feature-extraction algorithm is implemented in an FPGA by coding in VHDL language. The algorithm was discussed in detail in Chapter 5. Figure 7.2 shows the block diagram of the signal-processing logic for the feature-extraction algorithm which is implemented in FPGA for LNP preamplifier signals. The MWDI functional block produces a trapezoidal shape from the LNP preamplifier pulse. The MWDII functional block is used to reduce the tail on the trailing edge of the MWDI pulse, thus it reduces the response time of the detector, which decreases the probability of signal pile-up at high rates. The Baseline functional block restores the correct baseline for precise energy determination. The output of the Baseline functional block is connected to three blocks, namely to CFT, MA and Energy readout functional blocks. The CFT functional block provides the time-stamp information. The MA functional block is used for smoothing and noise reduction leading to precise pulse

detection at lower thresholds. For the ASIC (or analog shaper) signal the MWDI and MWDII blocks are bypassed.

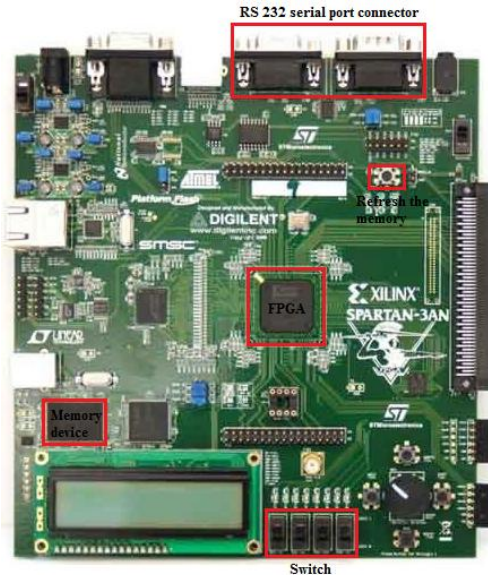


**Figure 7.1:** Photograph of the XILINX Spartan development board with XC3S700AN-FG484 FPGA and basic functions indicated [78].

<b>Switch Position and Modes</b>	
0	Copy of input data stream (echo mode)
1	MWD
2	MWD + MA
3	CFT (inverted and delayed triangle)
4	Smoothed pulse
5	Baseline level
6	MWD baseline
7	Zero-crossing
8	Suppression of baseline
9	Event energy measurement
10 – 15	10 bytes of event data or multiplexed data

**Table 7.1:** Event-data package format with the settings of binary switches.

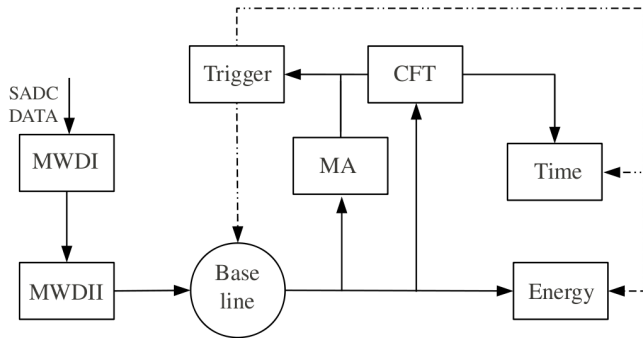


**Figure 7.2:** Block diagram of signal processing in FPGA for signals from the LNP preamplifier.

The VHDL code contains two parts, the feature-extraction algorithm and an input-output interface. The main module is called system container (see Figure 7.3). This module contains the clock management, I/O interfacing, and generic parameters. For debugging purpose, multiple busses are exported to present intermediate results. This feature is likely to be eliminated in the final version as it uses a lot of routing resources. Selection of output modes is done by means of an output select register.

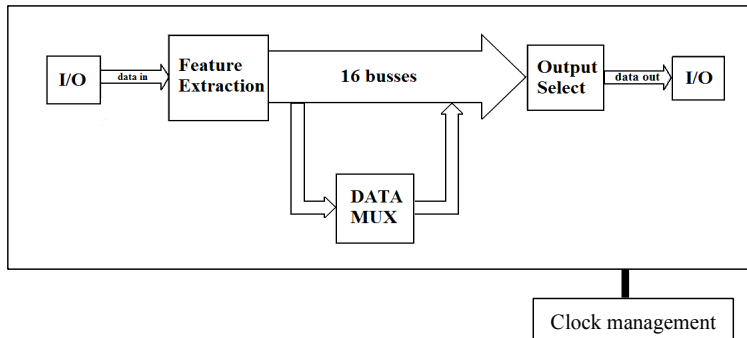


**Figure 7.3:** Block diagram of the system container.

The system container also contains the Feature-Extraction module which is used to process the data. The block diagram of the Feature-Extraction module is presented in Figure 7.4. This module consists of MWD and Constant Fraction (CF) sub-modules. Details of these modules are described below.

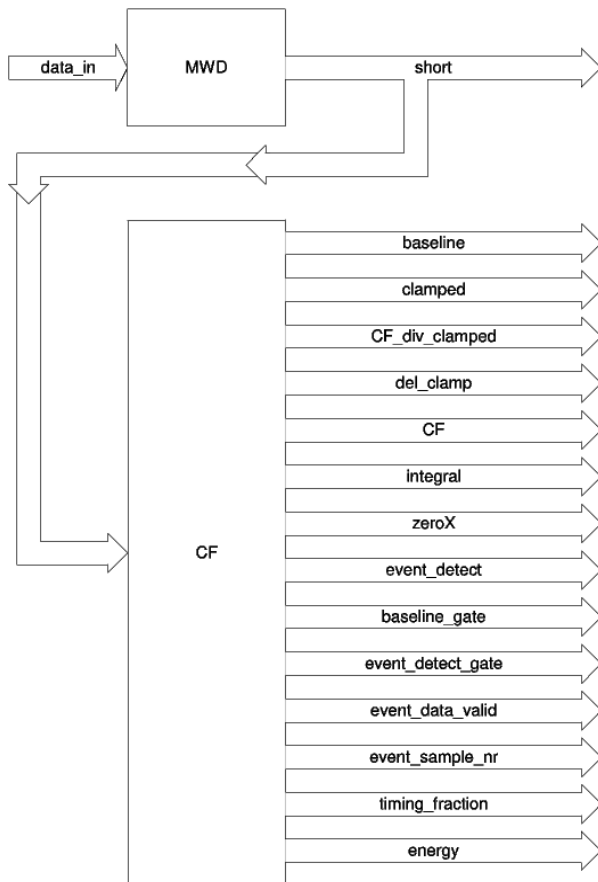


**Figure 7.4:** Block diagram of the Feature-Extraction logic.

**Mowing Window Deconvolution:** This function is taking the amplitude difference at two sampling points which are  $M$  sampling intervals apart ( $A[n] - A[n-M]$ ).  $M$  is the MWD differentiation filter length. The value of  $M$  can be set as an integer (2, 3, 4, 5, 6) power of two. The block diagram of the MWD function implemented in VHDL code is presented in Figure 7.5. The MWD logic consists of the Moving Sum and the Moving Difference blocks, which are briefly outlined in the following (see equation 5.8). The FPGA can perform binary operations only with integer numbers. However, the normalization constant  $1/\tau$  (see equation 5.8), expressed in units of the SADC sampling period  $T = 10$  ns, is a real number less than one and typically has the value  $1/2500$  for the LNP preamplifier decay constant of  $25\ \mu\text{s}$ . In order to make the FPGA implementation of the MWD filter algorithm possible, the sum term of equation 5.8 and the normalization constant are temporarily multiplied by the large value  $2^{24}$ , and after the multiplication operation, the result is divided by  $2^{24}$ .

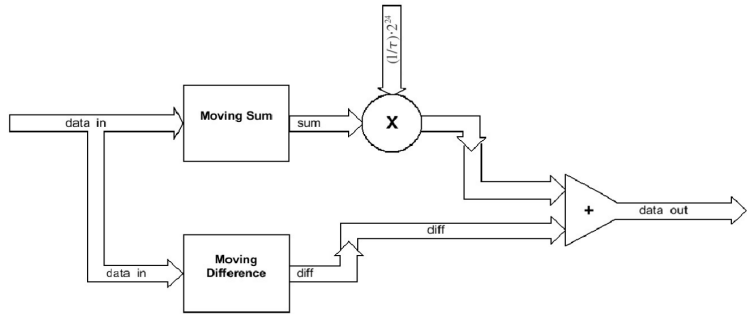


**Figure 7.5:** Block diagram of the MWD implementation in VHDL code.

**Moving Sum (MSUM)** also referred to as Moving average (MA): This function is implemented as a moving sum over  $M$  samples, where  $M = 2^n$  [79] and  $n$  is a natural number. A linear memory is needed to keep track of the current/last  $M$  samples. All samples are added to the moving sum and sample  $n-M$  is subtracted from it. Since the size of this moving sum is a power of two, a moving average is simply created by removing the  $n$  least significant bits. Figure 7.6 shows the block diagram of the Moving-Average implementation and indicates the addition (+) and subtraction (-) modules. In addition, a pipeline module has been implemented. The pipelining will help to increase the clock cycle for the process and is implemented as a dual-port memory with an integrated addressing mechanism. The dual-port RAM has the ability to simultaneously read and write different memory cells at different addresses [79]. This mechanism provides simultaneous read/write operations and automatic read/write pointer updating on each action. The difference between the read- and write-pointer addresses determines the effective length of the buffer, which remains constant as the pointers are updated simultaneously.

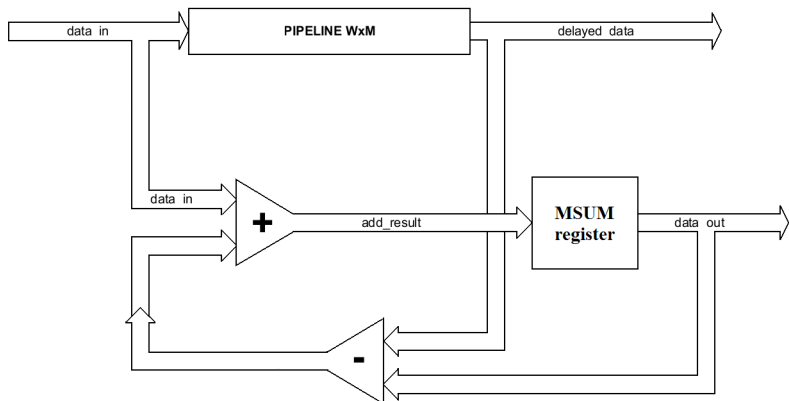


**Figure 7.6:** Block diagram of the Moving-Average implementation.  $W$  is a window size and  $W \times M$  represents the sum over  $M$  samples.

**Moving Difference (MDIFF):** This function is used in the MWD block-diagram; see Figure 7.5 [79]. The block-diagram in Figure 7.7 shows the features of “delaying” and “subtracting” the input data. This module does not require extra bits, because the input data is already signed integer.

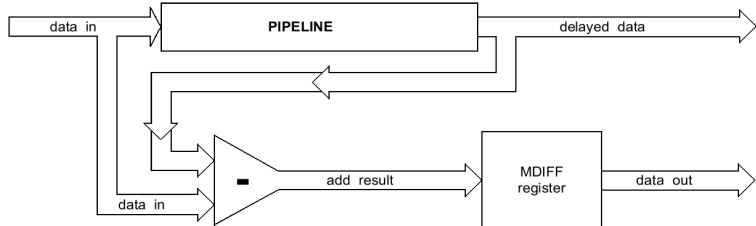


**Figure 7.7:** Block diagram of the Moving-Difference implementation.

**Constant Fraction Timing:** The CF Timing process will always have to deal with input signals on a non-zero baseline and therefore, requires a baseline-follower function resulting in “clamped data” (see Figure 7.8). Clamped data [79] can then be treated as “absolute” data values. The baseline calculation is, in principle, done only once but can be initialized on demand. In general, the baseline is estimated continuously. Only for test purposes, we created a possibility to use a constant value, estimated once at the start of the DAQ. For practical purposes, the CF-fraction =  $1/k$  (with  $k$  the attenuation coefficient defined in Eq. 5.12) is again a power of 2; in this case it is equal to 4. The CF signal is constructed to create a signal with a related zero-crossing to determine an exact time stamp. The zero-crossing function can also be used to detect an event. To be able to distinguish (positive-only) events from other (noise) zero-crossings the sum of original data is calculated. When a zero-crossing coincides with a sufficient integral value of an original baseline-subtracted pulse, an event is detected. In order to prevent false multiple-hits, an inhibition period is foreseen following each event. This is done by a ‘gate-generator’, which is constructed like a simple counter. The block diagram of the Event-detection implementation is presented in Figure 7.8.

The implementation of the feature-extraction algorithm in the FPGA required a certain number of CLBs, LUTs, and flip-flop memories. Table 7.2 presents the usage of the FPGA resources. For the feature-extraction algorithm 14%, 12% and 11% of the available CLBs, LUTs and flip-flops, respectively, were used [79].

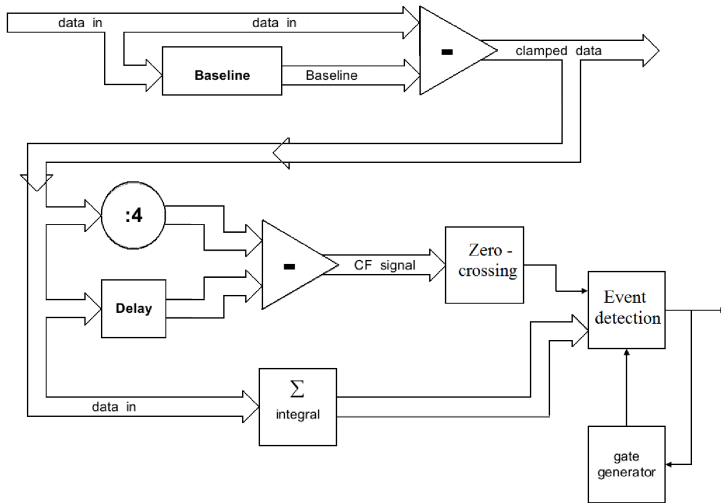


**Figure 7.8:** Block diagram of the implementations of Baseline follower and Event detection. The Event detection function is implemented as a zero-crossing detection and determines whether a smoothed (i.e. integrated) signal crosses a given threshold.

	Total Number	Feature-Extraction Algorithm	Constant Fraction	Baseline	Amplitude Detection
CLBs	15360	2166	219	130	47
LUTs	15360	1844	93	129	36
Flip-flop memories	15360	1686	158	111	33

**Table 7.2:** The available and required FPGA resources for the feature-extraction algorithm and some of its modules for 1 channel of the SADC readout.

## 7.4 Results obtained with the FPGA implementation

**Debug mode:** The FPGA implementation of the feature-extraction algorithm is designed to be user-friendly: one can monitor the processed pulse at different stages. Different output modes (Table 7.1) can be selected by binary switches for the Xilinx Spartan-3A development board (see Figure 7.1) or by output select registers for the SIS3302 SADC. The different debugging modes were tested with signals generated by the LED light pulser and the results are visualized in Figures 7.9, 7.10 and 7.11.

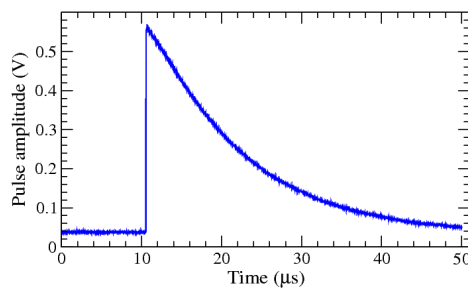


**Figure 7.9:** Debugging mode: Echo (copy) of the input data.

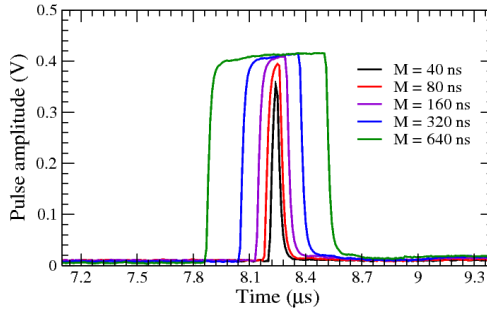


**Figure 7.10:** Debugging mode: MWD signal traces derived from input data for different MWD filter length  $M$ .

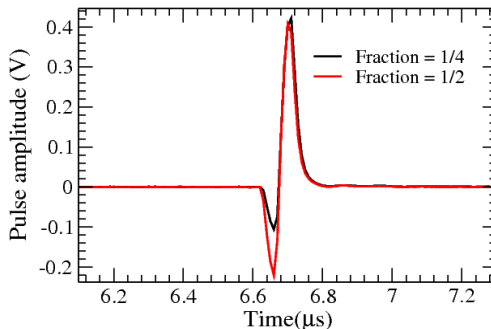


**Figure 7.11:** Debugging mode: CFT signal derived from input data for different CFT fractions.

**Xilinx Spartan Development Board:** The implementation of the feature-extraction algorithm was tested with signals from the LED light pulser. The test was performed semi-off-line, since the waveform of the analog preamplifier pulse was digitized and stored on disk. The recorded pulses were written into the memory of the development board via the RS-232 connector; the data were processed by the FPGA and simultaneously analyzed in software. The pulse amplitudes obtained by the semi-online analysis [fpga] and the software processing [soft] are compared in Figure 7.12. The corresponding results for the relative energy resolution  $\sigma/\mu$  and the time resolution  $\Delta t_{rms}$  are presented in Figure 7.13. Correlation coefficients of 99.9% are obtained for these two analyses.

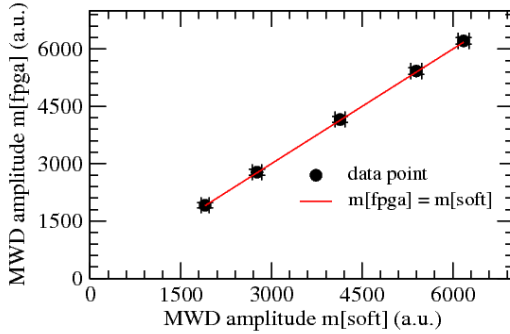


**Figure 7.12:** Comparison of pulse amplitudes obtained as MWD amplitude  $m[\text{soft}]$  and  $m[\text{fpga}]$  for the software analysis and the FPGA processing, respectively. According to the cosmic-ray calibration, the lower amplitude corresponds to 80 MeV and the higher one to 390 MeV. The correlation coefficient is 99.9%.

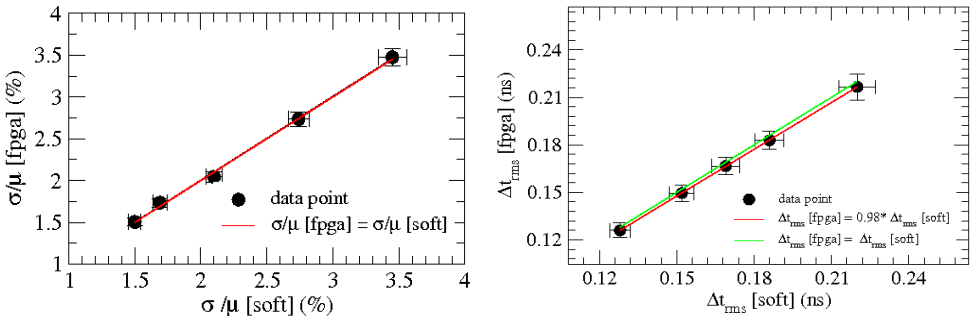


**Figure 7.13:** The correlation between energy resolution  $\sigma/\mu[\text{soft}]$  and  $\sigma/\mu[\text{fpga}]$  (left) and the time resolution  $\Delta t_{rms}[\text{soft}]$  and  $\Delta t_{rms}[\text{fpga}]$  (right) obtained for software analysis and FPGA processing, respectively. The correlation coefficient is 99.9%.

**SIS3302 Sampling ADC:** The commercial SIS3302 SADC (see Chapter 5), as mentioned above, disposes of 5 FPGAs from the Xilinx Spartan family. After satisfactory tests with the Xilinx Spartan-3A development board, the feature-extraction VHDL code was ported to the SADC. The firmware was loaded into the memory of the FPGA and thus

enabled the SADC to process the data on-line. The implementation can handle any sampling rate up to 100 MHz. The interfacing was also changed from serial port to VME-bus. To verify the performance of the SADC implementation, we compare the on-line pulse amplitude detection [on-line] with the software analysis [soft].

The performance measurements were carried out with the MWD filter length set to  $M = 320$  ns and the MA length set to  $L = 160$  ns. These values were optimal for the Proto60 data analysis (Chapter 6). The measurements were performed in two different modes: “store-traces” mode and “feature-extraction” mode. The measurements were done for different light intensities. At each fixed light intensity the preamplifier signal was recorded in parallel by one SADC using default firmware for off-line processing and was analyzed on-line by another SADC with our feature-extraction firmware implemented in FPGA, see Figure 7.14

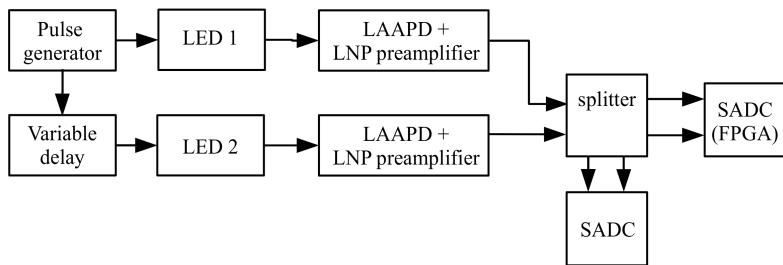


**Figure 7.14:** Scheme of the experimental setup with LNP preamplifier for the comparison of the timing measurements for the on-line and the off-line pulse processing in the Sampling ADC.

The relative energy resolution  $\sigma/\mu$  is calculated for different pulse amplitudes. The result is shown in Figure 7.15. The correlation coefficient is 99.9%. The slope obtained by linear regression is 1.03(2). In the case of the FPGA implementation, all the variables and operations are integer numbers and functions, respectively, but floating-point variables and operations are used in the off-line analysis. Therefore, it can be expected that the slope is not exactly 1.

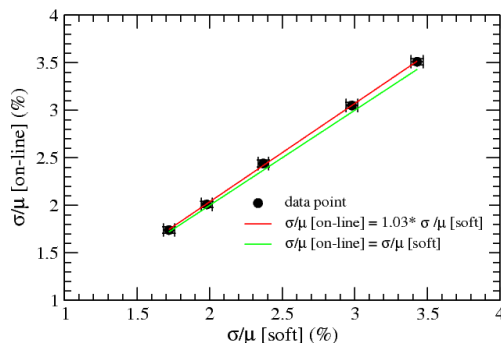


**Figure 7.15:** The comparison of the relative energy resolution  $\sigma/\mu[\text{on-line}]$  and  $\sigma/\mu[\text{soft}]$  for the on-line and the off-line (software) pulse processing obtained for different LED light intensities.

In order to observe the linear correlation between amplitude measurements in two SADC channels, the signals from both preamplifiers were fed into separate SADC channels. Light from the LED light pulser with about the same intensity was injected into both LAAPDs and the light intensity was varied. The on-line measured pulse amplitude correlation is shown in Figure 7.16.

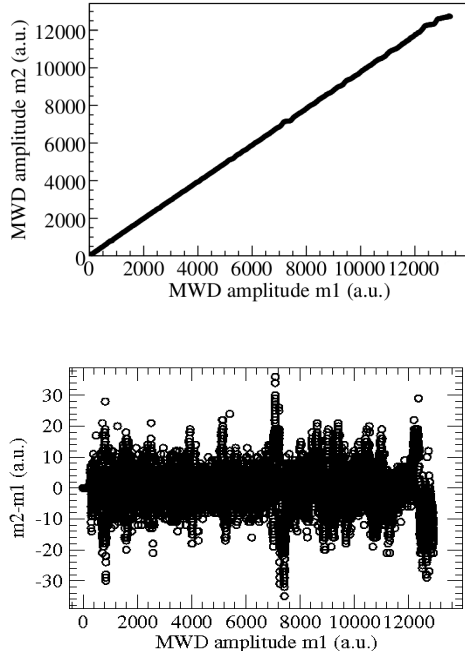


**Figure 7.16:** Top: The on-line detected pulse-amplitude correlation between two LAAPDs. Bottom: The difference of MWD amplitudes between two SADC channels. The difference is around zero, which confirms that both LAAPDs receive almost the same light intensity.

Time measurements were performed according to the scheme in Figure 7.14 and the results of the on-line pulse processing were compared with the results of the off-line analysis. The input pulse amplitude was kept constant and the CF timing parameters  $\text{delay} = 40 \text{ ns}$  and  $\text{fraction} = 0.5$  were chosen for both processes. The pulse generator was used to trigger both LED light pulsers. The pulse generator triggered the first LED light pulser promptly. The second LED light pulser was triggered with a delay, varied relative to the first pulse. The signals from both preamplifiers were split by a resistive impedance-matched splitter. The split signals were directed to two SADCs operated in “store-traces” and “feature-extraction” modes. The delay of the second pulse changes the time stamp of the coincidence time. The coincidence time was measured for different delays and the results are presented in Figure 7.17. We observe a linear correlation between the on-line and the off-line analysis with a slope of  $0.99(1)$  and a correlation coefficient of  $99.9\%$ .

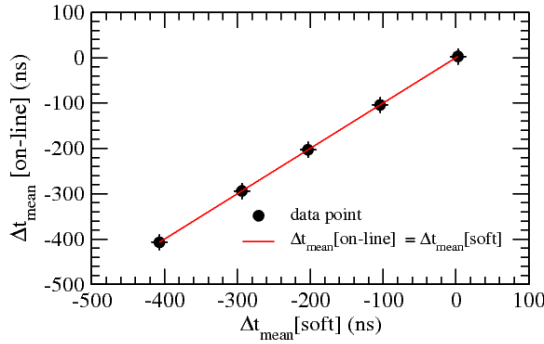


**Figure 7.17:** The comparison of the timing performance  $\Delta t_{\text{mean}} [\text{on-line}]$  and  $\Delta t_{\text{mean}} [\text{soft}]$  for the on-line and off-line (software) pulse processing, respectively, for constant LED light intensity and variable relative signal delay.

In order to study the linearity of the CF timing response, the time-stamp determination was compared with results obtained by a precision TDC in Figure 7.18. The experimental setup in this case was the same as described in Figure 7.14. The constant-fraction discriminator coupled with the TDC replaced the SADC with default firmware.

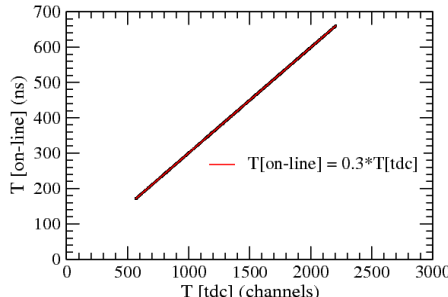


**Figure 7.18:** The correlation between the time differences  $T[\text{tdc}]$  and  $T[\text{on-line}]$  measured by TDC and SADC, respectively.

We observe a linear relation with slope 0.3. Using the fit equation ( $T[\text{on-line}] = 0.3 T[\text{tdc}]$ ), we can calibrate the TDC relative to SADC channels. Subsequently, we can check the difference of  $T[\text{on-line}] - 0.3 T[\text{tdc}]$ , which is measured by the SADC and TDC. The time differences obtained for different time positions determined by the TDC are shown in Figure 7.19. The time differences are closely spread around the zero line, which shows the precision of the on-line CFT method.

To evaluate the response of the CF timing obtained by the on-line pulse processing, the y-axis projection of the two-dimensional histogram in Figure 7.19 is shown in Figure 7.20 with the time axis calibrated in ns. The distribution can be described by a symmetric Gaussian function and after fitting we obtain a width  $\sigma = 0.4$  ns.

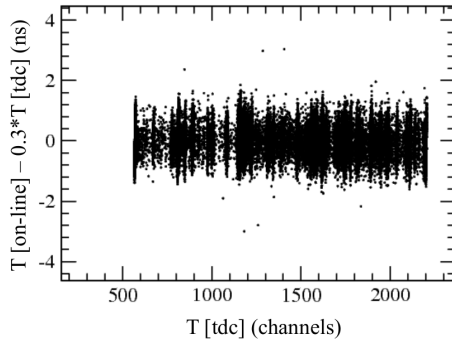


**Figure 7.19:** Scatter plot of time differences ( $T[\text{on-line}]-0.3 \cdot T[\text{tdc}]$ ) for each event as a function of the TDC time.

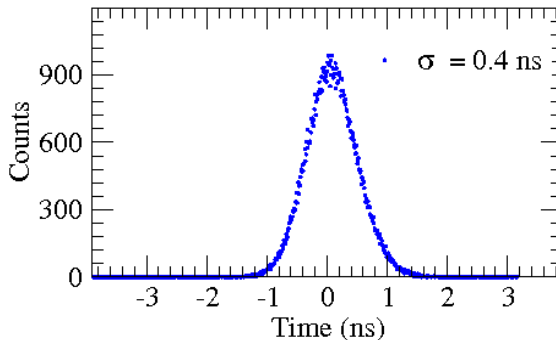


**Figure 7.20:** The y-axis projection of the scatter plot shown in Figure 7.19.

In addition to the LED pulser measurements, test results were obtained using signals from cosmic muons (see Chapter 6, setup with single crystal). The SADC was operated in a self-triggering mode. The incoming events were stored in memory and read out every 1 s to avoid memory overflow. Figure 7.21 shows the distribution of the detected pulse amplitudes. For this measurement the MWD filter length was set to  $M = 320$  ns (see Figure 6.35). The blue curve belongs to the raw spectrum for cosmic muon energy deposition in a single PWO crystal bar. Figure 7.22 shows the energy correlation between two SADC channels, where all events of the first channel, collected within a 1 s buffer, were combined with all events of the second channel, recorded within the same 1 s time window. In order to unambiguously determine events with two-channel correlations we inspect the differences of the time stamps. The differences  $dt$  of time stamps between two channels are shown in Figure 7.23 left. To select “coincidence” events, a time-cut of  $|dt| < 10$  ns was applied. The resulting histogram is shown in the lower panel of Figure 7.23. The corresponding energy-deposition histogram is shown in Figure 7.21 by the red curve.

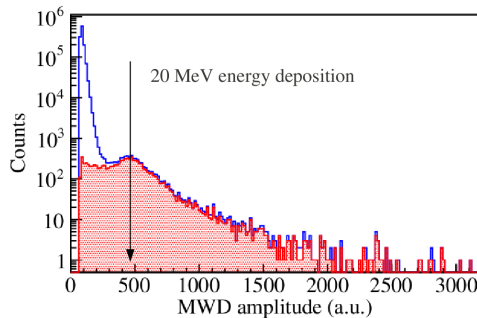


**Figure 7.21:** Spectrum of cosmic muon energy deposition. The data analysis is done on-line with our feature-extraction algorithm implemented in the FPGA of a commercial SADC. The blue curve indicates the raw spectrum of cosmic-muon energy deposition. The red curve shows the spectrum, when a coincidence is required between the signals from both end faces of the PWO crystal. The black arrow indicates the most probable energy deposition by cosmic muons.

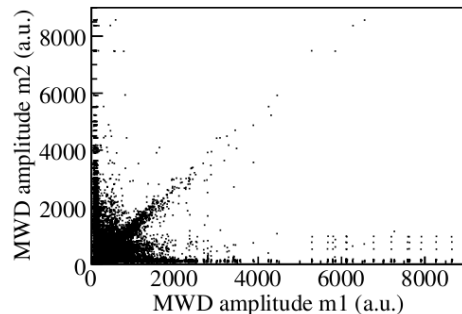


**Figure 7.22:** The on-line detected pulse-amplitude correlation for both SADC channels.

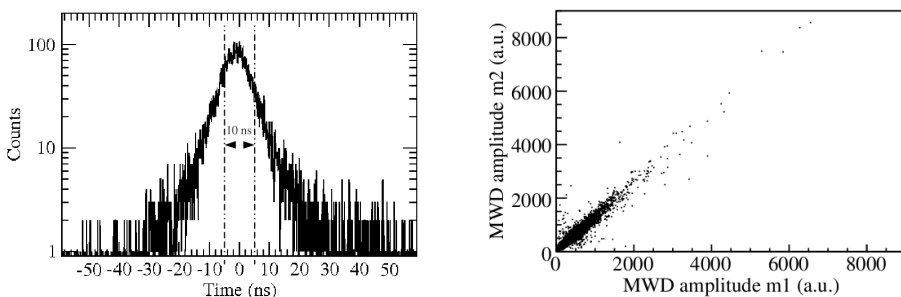


**Figure 7.23:** Left: Differences  $dt$  of time stamps between two channels for cosmic muon energy deposition. Right: Same as Figure 7.22, but showing the correlation between two channels after applying the time-cut  $|dt| < 10$  ns.

The time resolution is calculated using the time stamp difference between 2 LAAPDs (see Figure 7.24). For the estimation of the time resolution for 20 MeV energy depositions in the PWO crystal bar we have applied the condition, that the energy detected in the two channels differs by less than 10%. The calculated time resolution, obtained from the  $\sigma$  of the Gauss fit of the time stamp distribution divided by  $\sqrt{2}$ , is equal to  $3.16(3)$  ns for the on-line analysis. This result is very well comparable with the off-line determined value  $3.15(1)$  ns of the time resolution.

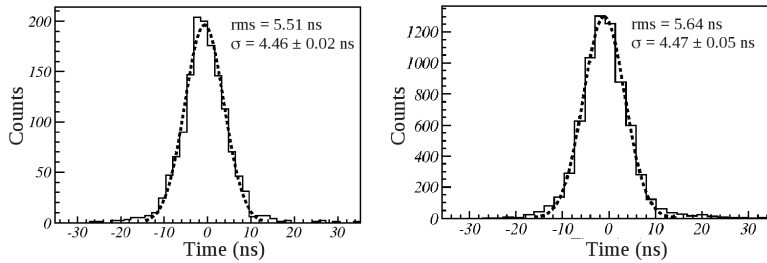


**Figure 7.24:** The distributions of time-stamp differences between two LAAPDs, optically coupled to a PWO crystal, for cosmic-muon energy depositions. The rms width of the peaks as well as the  $\sigma$  of the fits are included in the graphs for both analysis results. Left: Result from the off-line analysis. Right: Result from the on-line analysis.

## 7.5 Conclusion

The implementation of the feature-extraction algorithm in VHDL code into the FPGA was successfully tested with the LED light pulser and with cosmic-muon energy depositions in a single PWO crystal bar. The obtained results concerning energy and time resolution were compared with the software (off-line) analysis using the same algorithm and the same parameters. Linear correlations were observed between results from both pulse-processing procedures with correlation coefficients of 99.9% in all studied cases. Applying this data-acquisition (DAQ) concept, we proved an important element of the trigger-less readout concept in the case of measurements with cosmic muons. The trigger-less DAQ readout chain for the PANDA EMC will consist of a digitizer module, multiplexer and computer node (Chapter 5). The detected signal will be processed in order to extract the relevant information. Here, we presented the first-time application of a DAQ based on a commercial SADC with our newly developed feature-extraction algorithm implemented in FPGA. We demonstrated that this system allows reliable measurements based on on-line signal processing and event-feature extraction.

## 8. Evaluation of PANDA EMC performance

The rich PANDA physics program aims particularly at precise hadron spectroscopy. Whether the goals of the program can be reached depends crucially on the performance of the PANDA EMC. The Technical Design Report (TDR) [7] defined the requirements for the EMC readout electronics. The performance studies of the readout electronics, outlined in previous chapters, provided satisfactory results indicating that the requirements suggested in the TDR can be fulfilled.

In this chapter the performance results obtained from the Proto60 experiment will be used as input to basic simulations in order to assess the merits for physics results obtained with the PANDA EMC. Simulations are performed with PandaRoot [80], the general simulation and reconstruction software package developed for the PANDA experiment. Results will be discussed for single photons hitting a  $3 \times 3$  crystal array and for the decay of the  $h_c$  charmonium into  $7\gamma$  detected with the PANDA EMC. For the  $3 \times 3$  crystal array the energy resolution for single photons has been obtained and the influence of noise level and threshold on resolution and efficiency has been studied. In the study of the  $h_c$  charmonium state the simulation is performed for the entire EMC to demonstrate how the noise level and the cluster threshold affect the width of the reconstructed invariant mass.

### 8.1 Single photon simulations

In order to validate the Monte Carlo simulation setup, simulations were done with single photons of 200 MeV energy hitting the central crystal of a  $3 \times 3$  crystal array. The crystal shape is the same as used in the Proto60 setup. The rms width of the noise level for this simulation was 0.3 MeV and the threshold for individual crystals was set to 1 MeV, exactly as was done for the Proto60 experimental setup (Chapter 6). Figure 8.1 shows the experimental data and the simulated data for the electromagnetic shower shape detected in a  $3 \times 3$  PWO crystal array. The simulations agree with the experimental result except for small deviations in the corners of the crystal matrix. Such deviations are caused by the non-uniformity of the light collection inside the PWO crystal due to the tapered geometry of the crystals [81].

The deposited energy is summed up for all the crystals. In Figure 8.2 the line shape of the energy deposition spectrum fitted by an asymmetric Gauss function is shown. The obtained simulated resolution ( $FWHM/2.355)/E$  is 4.24%. The corresponding experimental resolution, parametrized in Figure 6.34 with the parameters  $a=0.35\%$  and  $b=1.97\%$ , is 4.76% and agrees with the simulated value within 11%.

Subsequently, for the same 0.3 MeV noise level and 1 MeV threshold, simulations were performed with photon energies up to 1.2 GeV energy. In Figure 8.3 top, the relative energy resolution determined as  $(FWHM/2.355)/E$  (%) is shown as a function of the photon energy  $E$ . In the bottom figure, the simulations and data from the PANDA EMC Technical Design Report [7] are shown for comparison. We observe good agreement of both simulations in the

low energy region, but a 23% difference at 1 GeV photon energy. The simulations in the TDR were done within a different framework using a different energy transport model than presently implemented in PandaRoot [82].

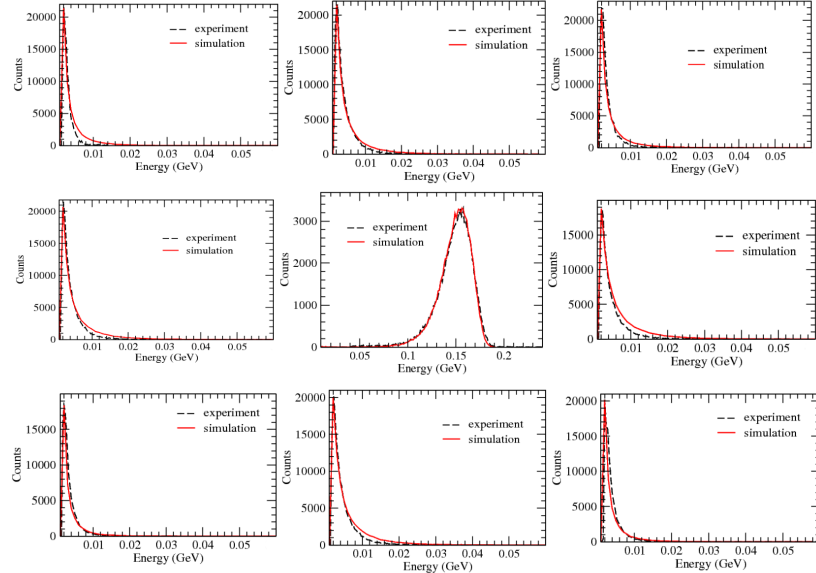


**Figure 8.1:** The electromagnetic shower shape for 200 MeV photons hitting the center of a  $3 \times 3$  PWO crystal array: the black dashed lines and the red solid lines represent the experimental data and the simulations, respectively.

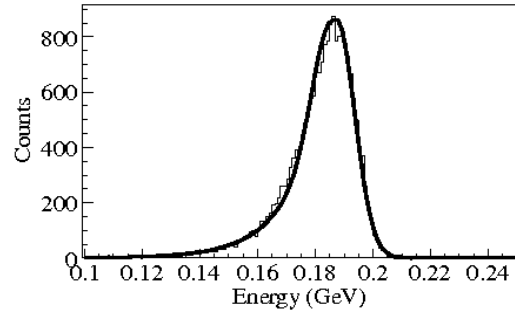


**Figure 8.2:** Simulated line shape of the energy deposition spectrum at the photon energy  $E_\gamma = 0.2$  GeV.

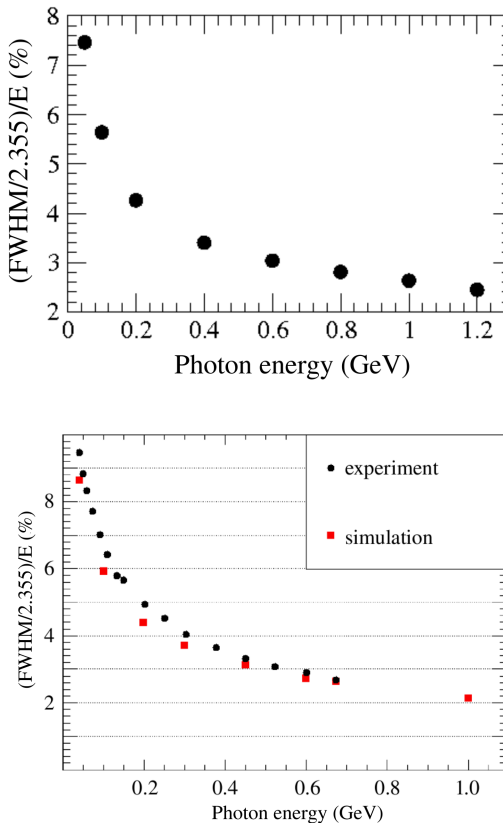


**Figure 8.3:** The simulated and experimental energy resolution  $(FWHM/2.355)/E$ . Top: the simulation performed for the  $3 \times 3$  crystal matrix. Bottom: The simulation with experimental data from the PANDA EMC TDR [7].

The energy resolution obtained in simulations for the interaction of 200 MeV photons with the  $3 \times 3$  crystal array agrees within about 10% with the experimental result for Proto60. Subsequently, the energy resolution of photon clusters is simulated for different noise levels and thresholds. In Figure 8.4 the dependence of the cluster energy resolution on the noise level of individual detectors is shown. The threshold was set to 1 MeV. We notice that the resolution worsens rapidly with increasing noise level of the readout electronics, i.e. by 25% for an increase of the noise level by a factor 5.

In order to avoid significant noise contributions to the summed cluster energy, the threshold for each individual detector should be set above the noise level, preferentially to a level equivalent to 3 times the RMS width of the noise level. The effect of the individual detector threshold on the energy resolution was investigated for simulations of 200 MeV photons hitting the  $3 \times 3$  crystal array. The RMS width of the noise level was fixed in this case to 0.3 MeV and the simulation was run for threshold values between 2 MeV and

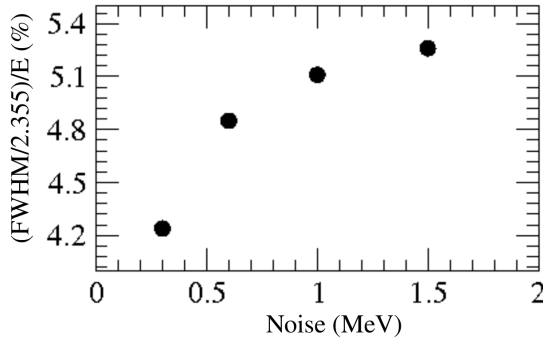


**Figure 8.4:** The cluster energy resolution for different noise levels of the readout electronics.

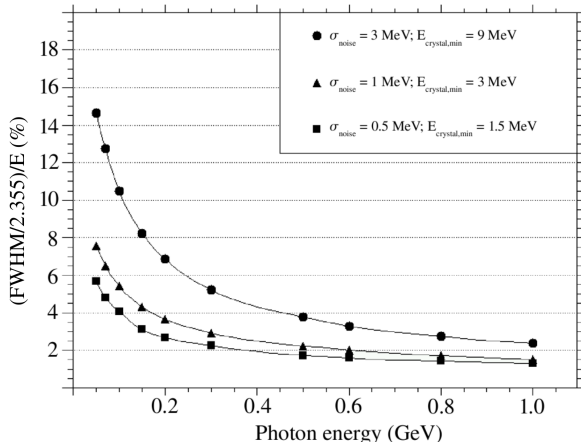
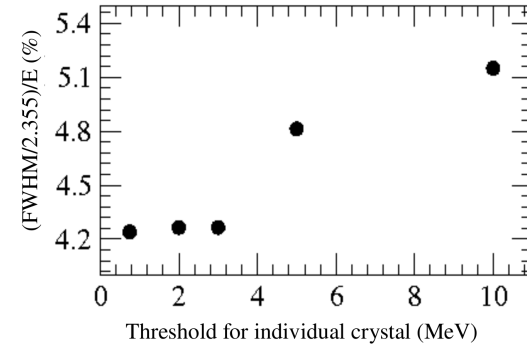


**Figure 8.5:** Top: The energy resolution for 200 MeV photons detected in a  $3 \times 3$  crystal array for different photon thresholds. Bottom: Simulation from the PANDA EMC TDR [7] with complete shower collection. The energy resolution is shown for photon energies up to 1 GeV and different noise levels corresponding to different photon thresholds.

10 MeV. The resulting dependence of energy resolution on the threshold value is presented in Figure 8.5. The energy resolution for photon clusters gets worse for a higher threshold on the energy deposition in each crystal, caused by reducing the number of detected photons. Most of the energy is deposited in the central crystal and the deposited energy in the neighboring detectors quickly drops below the threshold. For comparison to the present simulations, the results from the PANDA EMC TDR [7] are shown in the bottom part of Figure 8.5. The same trend in the dependence of energy resolution on noise level and threshold is observed but, at 200 MeV photon energy, our simulation predicts a worse resolution. The simulation presented in Figure 8.5, bottom panel, was performed for the PANDA EMC with complete shower collection in a dynamically-defined cluster of neighboring crystals. Due to the more complete shower collection, the energy resolution is improved in this case. Therefore, we observe the slight discrepancy between our simulation result and the simulation performed for the TDR [7]. The observed dependence of the energy resolution on the noise level emphasizes the need to keep the detector noise level as low as possible.

## 8.2 Simulations of the $h_c$ charmonium state

Based on the performance characteristics of the newly-developed electronics we demonstrate by Monte Carlo studies the ability of the PANDA EMC to detect and analyze charmonium states with the example of the  $h_c$  charmonium state. In addition, we show how the noise level, the threshold for individual detectors and the cluster threshold will influence the reconstructed mass and width of this state. For these studies the  $h_c$  state was chosen since its all-neutral decay channel depends crucially on the ability of the EMC to detect multiple photons with high resolution:

$h_c(^1P_1) \rightarrow \eta_c + \gamma \rightarrow \eta + \pi^0 + \pi^0 + \gamma \rightarrow 7\gamma$ . The invariant mass of this state will be reconstructed from the energy deposition of  $7\gamma$  in the EMC. The realistic simulation of this decay channel requires the response of the complete EMC.

The  $h_c$  state is the  ${}^1P_1$  charmonium state (Chapter 2) and according to the recent PDG table its mass is  $3525.42 \pm 0.29$  MeV [68]. Studies of the  $h_c$  state, in particular its precise width, will help to understand the hyperfine structure (or spin dependence) of QCD bound states. The  $h_c$  was observed first in the CLEO experiment in electron-positron annihilations:  $e^- + e^+ \rightarrow h_c \rightarrow \eta_c + \gamma$  [83]. The determined mass of the  $h_c$  state was  $3524.4 \pm 0.6 \pm 0.4$  MeV/c<sup>2</sup>. The mass and width of the  $h_c$  state was studied recently in the BES III experiment and the branching ratio for  $h_c \rightarrow \eta_c + \gamma$  is  $54.3 \pm 6.7 \pm 5.2\%$  [84]. The actual measured mass is  $3525.40 \pm 0.13 \pm 0.18$  MeV/c<sup>2</sup> and the width  $0.73 \pm 0.45 \pm 0.23$  MeV [84] is limited by the experimental accuracy. Due to the narrow width  $< 1$  MeV of the  $h_c$  state, a more precise experiment is required. For more detailed investigations, the anti-proton proton annihilation experiment PANDA will be able to measure the width of the state with much higher precision. The precision of the measurement with PANDA will be achieved by using the “resonance scanning” technique (see Chapter 2) exploiting the high-resolution HESR beam. The HESR will be run in two modes, the high-luminosity mode with a luminosity of  $10^{32}$  s<sup>-1</sup> cm<sup>-2</sup> and the high-resolution mode with  $10^{31}$  s<sup>-1</sup> cm<sup>-2</sup> [7]. For the high-luminosity mode of the HESR a production rate of the  $h_c$  charmonium state of 82 events/day is expected. In the high-luminosity mode the annihilation rate will be 20 MHz and each crystal in the Barrel EMC and the Forward Endcap EMC will produce an average signal (or event) rate of 100 and 500 kHz, respectively. This high rate will cause pile-up signals in individual detectors. The probability of pile-up of one signal with  $k$  other signals is described by the

Poisson distribution:

$P(k, \lambda) = (\lambda^k e^{-\lambda})/k!$  with the rate parameter  $\lambda = (\text{event rate}) \times (\text{pulse width})$ . For pile-up of two signals we have  $k = 1$ . From the Proto60 signal analysis (Chapter 6) we derived that the optimized width of the differentiated signal is >200 ns; as a worst case we assume 300 ns. For 500 kHz event rate the probability of pile-up will be 12.9%. In Table 8.1 the pile-up probability is shown for different event rates for the Barrel and the Forward Endcap EMC.

Annihilation rate (MHz)		20	30	50
Barrel EMC	Event rate (kHz)	100	150	200
	Pile-up Probability (%)	2.9	4.3	5.7
Forward Endcap EMC	Event rate (kHz)	500	750	1000
	Pile-up Probability (%)	12.9	17.7	22.2

**Table 8.1:** Pile-up probability for Barrel and Forward Endcap EMC for different annihilation rates (resulting in the given event rates).

As mentioned before, the envisaged average annihilation rate will be in the order of 20 MHz. However, the target structure in the PANDA experiment will not be uniform due to fluctuations in size and frequency of the frozen hydrogen pellets. Thus, the event rate in a single Forward Endcap detector is estimated to increase [85] from 500 kHz to a peak rate of about 750 kHz. In order to avoid pile-up due to high event rates, the detector response has to be short enough. The designed readout electronics with the newly-developed feature-extraction algorithm will help to reduce the pile-up probability to the lowest possible values. In addition, the concept of the trigger-less data acquisition, proven in this thesis, will allow reaching higher event-selection efficiency and thus the largest possible amount of good data events. If the average luminosity needs to be limited because of fluctuating data rates, PANDA will still be able to collect a large amount of high-quality data.

In addition, the performance of the readout electronics is playing a crucial role for the measured width of the reconstructed invariant mass. In the previous section we saw, that the energy resolution is sensitive to the noise level of the electronics, the threshold for the individual crystal, and the cluster threshold. To see how the performance of the readout electronics affects the reconstruction of the invariant mass, the PandaRoot simulations were performed for different noise levels, single-crystal thresholds and cluster thresholds. In these simulations a cluster is defined as the group of crystals which measure an energy deposition above a certain energy threshold. In Figure 8.6 the invariant mass distribution of the  $h_c$  charmonium state reconstructed from 7 photons is shown.

The detection of low-energy photons from the electromagnetic shower is important to obtain the optimal energy resolution. However, the detection threshold has to be set high enough to suppress noise and wrongly-reconstructed photons from statistical fluctuations of the electromagnetic shower [7]. Simulations were performed with photon cluster thresholds

in the range 20 MeV - 50 MeV. The noise level for each channel of the readout electronics was kept fixed at the lowest possible level of 0.3 MeV and the threshold for individual detectors was 1 MeV (Chapter 5). In addition, for comparison a simulation was performed with a higher noise level of 1 MeV and a corresponding energy threshold of 3 MeV. In Figure 8.7 the reconstructed width (top) and the reconstruction efficiency (bottom) for the  $h_c$  state are shown for different cluster threshold values obtained at two different noise levels of the readout electronics and the corresponding thresholds for the single crystals. We observe that the width gets larger with increasing noise level in the readout electronics, and, moreover, the efficiency drops with an increasing threshold in the single crystals.

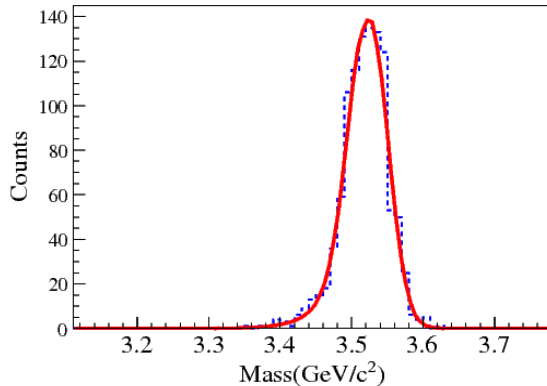


**Figure 8.6:** The invariant mass distribution reconstructed from 7 photons showing the  $h_c$  charmonium peak at  $3531 \pm 1.28 \text{ MeV}/c^2$ .

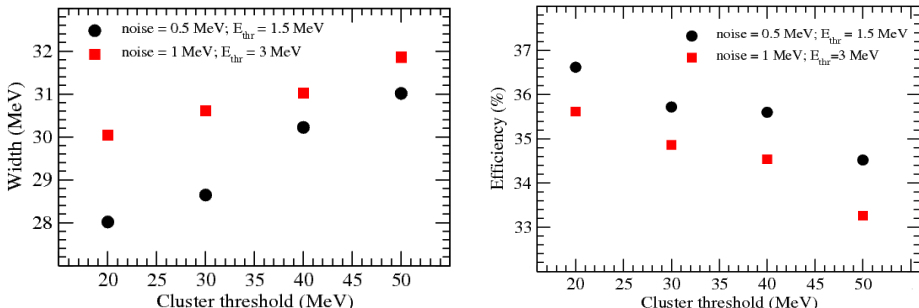


**Figure 8.7:** The width (left) and reconstruction efficiency (right) of the  $h_c$  charmonium state for different cluster thresholds.

In addition, we observe that the reconstructed width increases and the reconstruction efficiency decreases with increasing cluster threshold. In order to see the influence of the noise level, simulations were performed for noise levels between 0.5 MeV and 3 MeV for a photon cluster threshold fixed at 20 MeV. The results are shown in Figure 8.8. We observe that the simulated width of the  $h_c$  charmonium state is significantly influenced by the noise level in the readout electronics. It is, therefore, mandatory to put every effort into reducing

the noise level as much as possible.

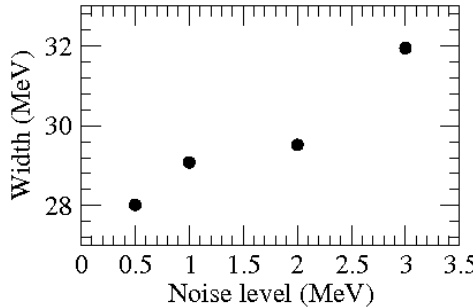


**Figure 8.8:** The simulated width of the  $h_c$  charmonium state for different noise levels of the readout electronics for the PANDA EMC.

### 8.3 Conclusion

The PandaRoot simulations are validated by comparison to measurements with single photons hitting a  $3 \times 3$  crystal array. The simulation and the experimental data show good agreement. The photon energy resolution is studied for different noise levels and single crystal thresholds. It has been shown, how the cluster energy resolution depends on the noise level and on the thresholds.

In order to demonstrate, how the performance of the EMC influences the reconstruction of charmonium states, the  $7\gamma$  decay channel of the  $h_c$  charmonium state was simulated.

The width of the  $h_c$  charmonium state was compared for different noise levels, thresholds of single crystals, and cluster thresholds. It has been shown that a high noise level in the readout electronics causes a worsening of the width estimation of the  $h_c$  charmonium state. Therefore, in our electronics development it was of key importance to keep the noise of readout electronics as low as possible.

To avoid a strong influence of the noise of the readout electronics on the measured signal, the single EMC detector threshold has to be adjusted accordingly. We have shown that the width of the  $h_c$  charmonium state gets worse at high threshold values and the efficiency decreases due to a reduction of the number of detected photons.

Low-energy photons and charged particles as well as noise can cause a wrong measurement of shower-energy and, therefore, a worsening of the reconstructed width of charmonium states. Thus, the width of the  $h_c$  charmonium state was investigated for different cluster thresholds. We observed that the width and the efficiency get worse for high cluster thresholds. Figure 8.7 shows that width and efficiency improve for a lower noise level at the same cluster threshold, which underlines the need for the discussed noise-reduction techniques.

The simulation study of the performance for the PANDA EMC has shown that the EMC has to have the best performance in terms of noise level and high-rate capability, in order to be able to study narrow resonances.

## Outlook and valorization

In this thesis, the concept of a trigger-less data acquisition is pursued and a prototype system based on a commercial Sampling ADC has been developed. It is shown, that such type of data readout allows to reach better performance in terms of noise level, energy and time resolutions. In this way the requirements described in the PANDA EMC Technical Design Report [7] could be met. In addition, the digitization and continuous on-line processing of the front-end preamplifier/shaper signals prevent dead time. This feature allows to run the DAQ at high rate.

In the future, the prototype of the trigger-less DAQ will be tested with high energy photon beams using the Proto60 EMC prototype. At present, the performance of the trigger-less DAQ is investigated by comparing the results with those from an off-line processing of data taken during test measurements.

We have shown, that the DAQ can on-line process pulses of different shapes, such as charge-integrating preamplifier pulses as well as shaped pulses. Therefore, the developed readout can be applied for a very wide range of experiments.

The VHDL code of the feature-extraction algorithm will be open under General Public License (GPL), which will allow the free use for other projects. The commercial company STRUCK [48] is interested in porting of our firmware to other modules [86]. STRUCK has already received one request from an experimental group at Darmstadt to have our newly-developed features implemented.

Another possible application of our DAQ concept is the construction and readout of a luminosity-monitor detector at the BESIII (Beijing Electron Spectrometer) experiment.

The luminosity achieved at the BEP-II accelerator [87] has reached  $3 \cdot 10^{32} \text{ cm}^{-2}\text{s}^{-1}$ . The on-line monitor of the luminosity is required for precise monitoring of the stability of the beam intensity in order to determine precisely the cross sections of physics processes. The main challenge of the on-line monitoring of luminosity is to overcome limitations due to dead time in the DAQ introduced by high interaction rates.

The trigger-less readout will provide the most efficient way of using the hit information with minimal losses. The setup will require only a few single crystals to detect the incoming electrons or positrons at high rates. To avoid pile-up of the incoming pulses, the width of the MWD pulses should be reduced as much as possible. The data acquisition concept developed at the *Kernfysisch Versneller Instituut* can be used at different experimental setups operated at various event rates.

---



## Bibliography

- [1] T. Morii, C.S. Lim, and S.N. Mukherjee, The Physics of Standard Model and Beyond, World Scientific Publishing Co. Pte. Ltd., ISBN 981-02-4571-8 (2004)
  - [2] W.N. Cottingham and D.A. Greenwood, An Introduction to the Standard Model of Particle Physics, 2<sup>nd</sup> edition, Cambridge University Press, ISBN 978-0-521-85249-4 (2007)
  - [3] LHC Guide, <http://cdsweb.cern.ch/record/1092437/files/CERN-Brochure-2008-001-Eng.pdf>
  - [4] Fermilab Lattice Collaboration, <http://lqcd.fnal.gov/physics.html>
  - [5] C.T. Davies et al., Phys. Rev. Lett. 92, 022001 (2004)
  - [6] Physics Performance Report for PANDA: Strong Interaction Studies with Antiprotons, The PANDA Collaboration, arXiv:0903.3905v1 [hep-ex]
  - [7] PANDA EMC Technical Design Report, The PANDA Collaboration, arXiv :0810.1216v1 [physics.ins-det] ; [www-panda.gsi.de](http://www-panda.gsi.de)
  - [8] J. J. Aubert et al., Phys. Rev. Lett. 33, 1404 (1974)
  - [9] CLEO Experiment, [http://www.lepp.cornell.edu/Research/EPP/CLEO/#CLEO\\_s\\_Physics](http://www.lepp.cornell.edu/Research/EPP/CLEO/#CLEO_s_Physics)
  - [10] BELLE Experiment, <http://belle.kek.jp/belle/transparency>
  - [11] BES III Experiment, <http://bes.ihep.ac.ch/>
  - [12] C.M. Kiesling, Results on charmonium from Crystal Ball, SLAC Publication 2386 (1979)
  - [13] M. Ablikim et al., Phys. Rev D 71, 092002 (2005)
  - [14] M. Andreotti et al., Nucl. Phys. B 717, 34 (2005)
  - [15] J. Ritman, Charmonium Physics with PANDA at FAIR, arXiv: 0702013v1 [hep-ex]
  - [16] S.K. Choi et al., Phys. Rev. Lett. 89, 102001 (2002)
  - [17] C. Edwards et al., Phys. Rev. Lett. 48, 70 (1982)
  - [18] W. M. Yao et al., J. Phys. G: Nucl. Part. Phys. 33, 1 (2010)
  - [19] BABAR Experiment, <http://www.slac.stanford.edu/BFROOT/>
  - [20] R. Gupta, Introduction to Lattice QCD, arXiv: 9807028v1 [hep-lat]
  - [21] P. Chen, X. Liao and T Manke, Nucl. Phys. B (Proc. Suppl.) 94, 342 (2001)
  - [22] K. Peters, Charmed hybrids in proton antiproton annihilation, Nucl. Instr. and Meth. in Phys. Res. B 214, 60 (2004)
  - [23] V. Crede and C.A. Meyer, The Experimental Status of Glueballs, arXiv: 0812.0600v3 [hep-ex]; Prog. Part. Nucl. Phys. 63, 74 (2009)
-

- [24] C. Morningstar and M. Peardon, Phys. Rev. D 60, 34509 (1999)
  - [25] R. Jones, Joint Jefferson Lab/Institute for Nuclear Theory, Workshop on Gluonic Excitations, Jefferson Lab, Newport News, Virginia, May 14-16, 2003; <http://www.int.washington.edu/PROGRAM/program03.html>
  - [26] D. Acosta et al., Phys.Rev. Lett. 93, 072001 (2004)
  - [27] D. Bettoni, Physics with the PANDA detector at GSI, Journal of Physics: Conference Series 9, 309 (2005)
  - [28] PANDA Technical Progress Report, The PANDA Collaboration; <http://www-panda.gsi.de>
  - [29] C. Ekström et al., Hydrogen pellet targets for circulating particle beams, Nucl. Instr. and Meth. in Phys. Res. A 371, 572 (1996)
  - [30] PANDA Detector Overview, [http://www-panda.gsi.de/framework/Det\\_iframe.php?section=Full View](http://www-panda.gsi.de/framework/Det_iframe.php?section=Full%20View)
  - [31] PANDA Magnets Technical Design Report, The PANDA Collaboration, arXiv:0907.0169v1 [physics.ins-det]; <http://www-panda.gsi.de>
  - [32] CMS Collaboration. CMS: The electromagnetic calorimeter. Technical design report. CERN-LHCC-97-33
  - [33] ALICE Collaboration. ALICE technical design report of the photon spectrometer. CERN-LHCC-99-04
  - [34] R. Novotny, Fast and compact lead tungstate based electromagnetic calorimeter for the PANDA detector at GSI, IEEE Transactions on Nuclear Science, 51, 6 (2004)
  - [35] F. Sauli, Instrumentation in High Energy Physics, 2<sup>nd</sup> edition, World Scientific, ISBN 978-9-810-21473-9 (1993)
  - [36] G.R. Gilmore, Practical Gamma-Ray Spectrometry, 2<sup>nd</sup> edition, John Wiley and Sons Ltd., ISBN 978-0-470-86196-7 (2008)
  - [37] Physics Letters B 667, Review of Particle Physics, 304 (2008)
  - [38] Electromagnetic shower image, [http://www-zeus.physik.uni-bonn.de/~brock/feynman/vtp\\_ws0506//chapter02/em\\_shower.jpg](http://www-zeus.physik.uni-bonn.de/~brock/feynman/vtp_ws0506//chapter02/em_shower.jpg)
  - [39] R. Novotny et al., High resolution calorimetry with PWO, IEEE Nuclear Symposium, Puerto-Rico, Conference record, ISBN 0-7803-9222-1, N12-4 (2005)
  - [40] S.M. Sze, Physics of Semiconductor Devices, John Wiley and Sons, 2<sup>nd</sup> edition, ISBN 0-471-09837-X (1981)
  - [41] Hamamatsu, Photonics, [http://jp.hamamatsu.com/products/sensor/ssd/pd078/index\\_en.html](http://jp.hamamatsu.com/products/sensor/ssd/pd078/index_en.html)
  - [42] G.F. Knoll, Radiation Detection and Measurement, John Wiley and Sons, 3<sup>rd</sup> edition, ISBN 0-471-07-338-5 (2000)
  - [43] W.R. Leo, Techniques for nuclear and particle physics experiments, Springer-Verlag, ISBN 0-387-17386-2 (1994)
-

- [44] W. Erni and M. Steinacher, Univ. Basel, in PANDA Technical Progress Report, <http://www-panda.gsi.de/framework/documents.php> (2005)
  - [45] P. Wieczorek and H. Flemming, Advancement of a low noise preamplifier ASIC for the PANDA EMC, GSI Scientific Report 2007, 30, GSI Report 2008-1
  - [46] P. Wieczorek and H. Flemming, Low noise preamplifier ASIC for the PANDA EMC, GSI Scientific Report, 2006, 4, GSI Report 2007-1
  - [47] S. Braun and N. Müller, Report on scientific internship at KVI, Groningen, August-September 2010
  - [48] SIS3302 SADC, <http://www.struck.de/sis3302.html>
  - [49] MBS framework, <http://www-win.gsi.de/daq/>
  - [50] RIO-3 processor, <http://www.ces.ch/technology/backward-compatible>
  - [51] GO4 package, <http://www-win.gsi.de/go4/>
  - [52] F.S. Goulding and D.A. Landis, Signal Processing for Semiconductor Detectors, IEEE Transactions on Nuclear Science, 29 (1982)
  - [53] A. Georgiev and W. Gast, Digital pulse processing in high resolution, high throughput, gamma-ray spectroscopy, IEEE Transactions on Nuclear Science, 40, 770 (1993)
  - [54] A. Georgiev, W. Gast and R.M. Lieder, An analog-to-digital conversion based on a moving window deconvolution, IEEE Transactions on Nuclear Science, 41, 1116 (1994)
  - [55] G.P. Westpfahl, Adaptive Digital Filter for High-Rate High- Resolution Gamma Spectroscopy, IEEE Transactions on Nuclear Science, 48, 3 (2001)
  - [56] M. Kavatsyuk (E. Guliyev) et al., Performance of the prototype of the electromagnetic calorimeter for PANDA, Nucl. Instr. and Meth. in Phys. Res. A 648, 77 (2011); DOI:10.1016/j.nima.2011.06.044
  - [57] A. Fallu-Labruyere, H. Tan, W. Hennig, W.K. Warburton, Time resolution studies using digital constant fraction discrimination, Nucl. Instr. and Meth. in Phys. Res. A 579, 247 (2007)
  - [58] W.A. Kielek, Calculation of time resolution of scintillation counters with constant fraction discriminators, Nucl. Instr. and Meth. in Phys. Res. A 368, 392 (1996)
  - [59] B.C. Robertson, The influence of charge collection characteristics on HPGe detector timing performance, Nucl. Instr. and Meth. 169, 465 (1980)
  - [60] J.S. Kapustinskiy et al., Nucl. Instr. and Meth. in Phys. Res. A 241, 612 (1985)
  - [61] H. Baumeister et al., Design and performance of the saphir lead glass calorimeter, Nucl. Instr. and Meth. in Phys. Res. A 292, 81 (1990)
  - [62] M. Lopategui, Report on scientific internship at KVI Groningen, May-November 2010
  - [63] T.R. Saito et al., The HypHI Phase 0 experiment, Nucl. Phys. A 835, 110 (2010)
  - [64] James F. Ziegler, Nucl. Instr. and Meth. in Phys. Res. B 219–220, 1027 (2004)
  - [65] MAMI accelerator, <http://www.kph.uni-mainz.de/B1/accelerator.php>
-

- [66] J.C. McGeorge et al., Upgrade of the Glasgow photon tagging spectrometer for Mainz 19 MAMI-C, *Europ. Phys. Journal A* 37, 129 (2008)
- [67] CAEN V775AC TDC, <http://www.caen.it/nuclear/product.php?Mod=V775>
- [68] Particle Physics Booklet, *Journal of Physics G* 37, 075021 (2010)
- [69] ROOT package, <http://root.cern.ch>
- [70] A.R. Gabler et al., *Nucl. Instr. and Meth. in Phys. Res. A* 346, 168 (1994)
- [71] T. Matulewicz et al., *Nucl. Instr. and Meth. in Phys. Res. A* 289, 194 (1990)
- [72] D. Bremer et al., Performance of Proto60, XXX. PANDA Collaboration Meeting, 9 September 2009
- [73] GEANT4 package, [www.geant4.org](http://www.geant4.org)
- [74] Rihua Mao et al., *IEEE TNS* 55 No. 4, 2425, August 2008
- [75] U. Meyer-Baese, Digital Signal Processing with Field Programmable Gate Arrays, 3<sup>rd</sup> edition, Springer publication, ISBN 978-3-540-72612-8 (2003)
- [76] Pong P. Chu, FPGA Prototyping by VHDL Examples, Xilinx Spartan-3 Version, Pong Cleveland State University, Wiley-Interscience publication, ISBN 978-0-470-18531-5 (2008)
- [77] D. Ibrahim, Microcontroller Based Applied Digital Control, John - Wiley and Sons Ltd., ISBN 978-0-470-86335-0 (2006)
- [78] Spartan-3A FPGA Starter Kit Board User Guide, June 2008
- [79] P.J.J. Lemmens, private communication, KVI Groningen, March-April 2011
- [80] PandaRoot package, <http://panda-wiki.gsi.de/cgi-bin/view/Computing/WebHome#PandaRoot>
- [81] O. Lundberg, Measures to improve the light yield uniformity of tapered PWO crystals, Master thesis: Stockholm University, 28 February 2011
- [82] J. Messchendorp, private communication, KVI Groningen, May-June 2011
- [83] J. Rosner et al., *Phys. Rev. Lett.* 95, 102003 (2005)
- [84] M. Ablikim et al., Measurements of  $h_c(1P1)$  in  $\Psi'$  decays, *Phys. Rev. Lett.* 104, 132002 (2010)
- [85] D. Prasuhn, News from HESR, XXXII. PANDA Collaboration Meeting, 10 March 2010
- [86] E. Guliyev, M. Kavatsyuk et al., VHDL Implementation of Feature-Extraction Algorithm for the PANDA Electromagnetic Calorimeter, *Nucl. Instr. and Meth. in Phys. Res. A* (2011) (*submitted for publication*)
- [87] Luminosity measurement at BESIII, [http://bes.ihep.ac.ch/bes3/phy\\_book/book/phy/lumbes3.pdf](http://bes.ihep.ac.ch/bes3/phy_book/book/phy/lumbes3.pdf)

## List of abbreviations

ADC	Analog to Digital Converter
ALICE	A Large Ion Collider Experiment
APFEL	ASIC for PANDA Front End Electronics
ASIC	Application-Specific Integrated Circuit
BEPC	Beijing Electron Positron Collider
BES	Beijing Spectrometer
CFT	Constant Fraction Timing
CLB	Configurable Logic Block
CLEO	CLEOpatra
CMS	Compact Muon Spectrometer
CN	Computer Node
COSY	COoler SYnchrotron
CSA	Charge Sensitive Amplifier
DAQ	Data AcQuisition
DCM	Digital Clock Manager
DSP	Digital Signal Processor
EMC	ElectroMagnetic Calorimeter
ENC	Equivalent Noise Charge
FAIR	Facility Antiproton Ion Research
FPGA	Field Programmable Gate Array
FWHM	Full Width at Half Maximum
GEM	Gas Electron Multiplier
GO4	GSI Object Oriented On-line Off-line system
GPL	General Public License
GSI	Gesellschaft für SchwerIonenforschung
HDSM	Harmonic Double Sided Microtron
HESR	High Energy Storage Ring
IOB	Input Output Block
IP	Internet Protocol
JETSET	JET cluStEr Target
LAAPD	Large Area Avalanche Photo Diode
LEAR	Low Energy Antiproton Ring
LED	Light Emitting Diode
LHC	Large Hadron Collider
LNP	Low Noise low Power (preamplifier)
LQCD	Lattice Quantum ChromoDynamics
LUT	Look Up Table
MA	Moving Average
MAMI	MAinzer MIkrotron
MBS	Multi Branch System
MUX	MUltipleXer
MVD	Micro Vertex Detector
MWD	Mowing Window Deconvolution

---

PANDA	antiProton ANnihilation at DArmstadt
PCB	Printed Circuit Board
PDG	Particle Data Group
phe	photo electron
PHOS	PHOton Spectrometer
PID	Particle IDentification
PWO	PbWO <sub>4</sub>
QCD	Quantum ChromoDynamics
QE	Quantum Efficiency
QGP	Quark-Gluon Plasma
RAM	Random Access Memory
RT	Room Temperature
SADC	Sampling ADC
SM	Standard Model
SRIM	Stopping and Range of Ions in Matter
STT	Straw Tube Tracker
TCP	Transmission Control Protocol
TDC	Time to Digital Converter
TDR	Technical Design Report
TFA	Timing Filter Amplifier
TOF	Time Of Flight
TPC	Time Projection Chamber
VHDL	VHSIC Hardware Description Language
VHSIC	Very High Speed Integrated Circuits
VME	Versa Module Europa
VPT	Vacuum Photo Triode
WASA	Wide Angle Shower Apparatus

## Summary

The Standard Model of particle physics has been very successful in identifying three generations of quarks, leptons, and various bosons as the fundamental and elementary building blocks of matter. It remains a challenging puzzle to understand the underlying mechanisms that are responsible for the properties of nucleons, protons and neutrons, which are the building blocks of atomic nuclei. Hadrons containing charm quarks are the most promising laboratories that may reveal the secrets of the strong interaction on the long-distance scale which is relevant for the structure of hadrons. Precision measurements of mass, width and decay branches of all charmonium states will provide information on the quark-confining potential and its spin dependence (see Figure 1, left panel). The charmonium states above the  $D\bar{D}$  thresholds are poorly explored.

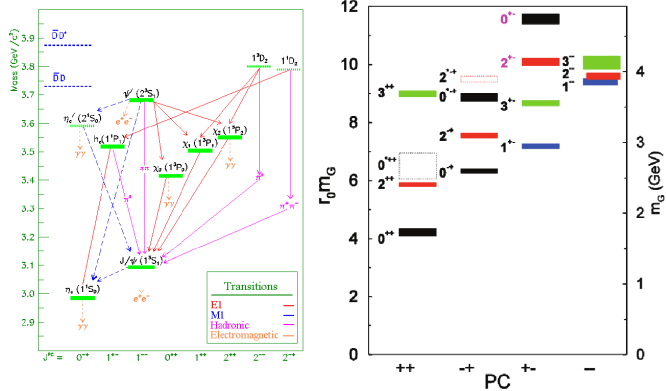


**Figure 1:** Left: Spectrum of charmonium states and transitions according to the given legend. Right: Glueball predictions from LQCD calculations.

Calculations using the discretized strong interaction (QCD) on a space-time lattice (LQCD) predict yet unobserved composite particles like glueballs (see Figure 1, right panel). Light glueballs are experimentally hard to identify since they may mix with ordinary mesons. Therefore, heavy glueballs with exotic quantum numbers would be narrower and easier to detect.

In order to study the strong interaction in the non-perturbative regime of QCD, the PANDA experiment for proton-antiproton annihilations has been designed. With anti-proton beams in the momentum range 1.5 - 15 GeV/c, provided by FAIR Darmstadt, states with exotic quantum numbers, as predicted by LQCD, can be excited. PANDA aims to study hadrons containing a charm quark or consisting of a charm ( $c$ ) and anti-charm ( $\bar{c}$ ) quark. The physics program of the PANDA experiment focuses on charmonium spectroscopy and the search for hybrid states and glueballs (see Figure 2). Moreover, a large variety of other

physics topics such as the study of hypernuclei, in particular those with two  $\Lambda$  hyperons, and measurements of the timelike form factor of the proton [6] will be addressed.

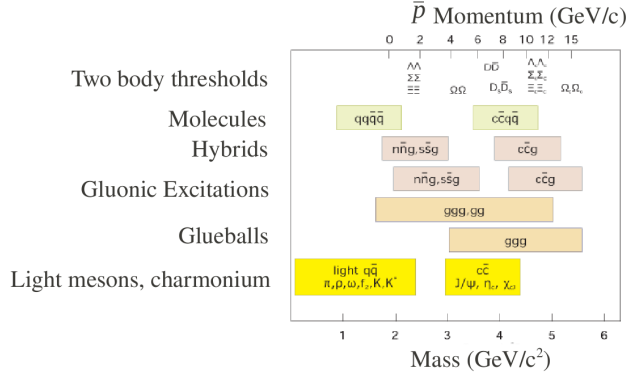


**Figure 2:** Mass range of hadrons that will be accessible by the PANDA experiment. The upper scale indicates the corresponding antiproton momenta.

The broad physics program requires a compact and multi-purpose detector system with a high-resolution Electromagnetic Calorimeter (EMC). This thesis focuses on optimizing the EMC for most sensitive and high-rate studies. High precision studies of rare processes require a fast, complex and safe selection of promising events. Thus, the readout electronics should be able to provide high-level triggering information, like the invariant mass of neutral mesons or decay vertices. The first and most important stages of such readout electronics for the PANDA EMC have been developed, tested and evaluated in the context of this thesis.

## PANDA Detector

The PANDA detector (Figure 3) will be installed at the High-Energy Storage Ring (HESR) at FAIR to detect the various types of particles after the annihilation of anti-protons. The detector can operate at high annihilation rates up to  $2 \cdot 10^7$  annihilation/s, will have a good particle identification, high momentum resolution, excellent vertex reconstruction and high-resolution calorimetry. Moreover, a new approach for event selection will be employed in order to increase efficiency and quality of data collection. In this approach all detector channels will be self triggering entities, providing all information to the data acquisition system. This information will be used for the selection of events based on the physics properties of particles, such as reconstructed invariant mass or a detected secondary vertex. This approach is named a trigger-less data acquisition [28].

## Calorimetry for PANDA detector

A crucial component of the PANDA detector is the Electromagnetic Calorimeter (EMC). The EMC will detect high-energy electrons, positrons and photons in the final state with high time and energy resolutions. The EMC was designed to achieve an almost  $4\pi$  coverage in the target spectrometer (see Figure 3).

The calorimeter will be able to detect electromagnetic particles in a wide dynamic energy range, from 10 MeV up to 10 GeV. This range is dictated by the physics program of the PANDA experiment. For high annihilation rate a fast-response calorimetry is required. On the other hand, precision spectroscopy requires high granularity of the calorimeter. For this purpose the PbWO<sub>4</sub> (PWO) material has been chosen to construct the calorimeter. The placement of the detector in a high 2 T magnetic field prevents the use of photomultipliers as a photo sensors. Therefore, large-area avalanche photo diodes will be used. The EMC will be operated at -25 °C temperature in order to increase the light yield of PWO crystals and to improve the EMC performance.

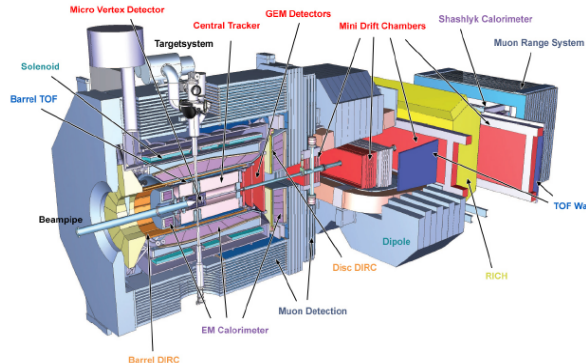


**Figure 3:** The Target Spectrometer (left part) and the Forward Spectrometer (right part) of the PANDA detector. The various sub-detector components are indicated.

## Feature-extraction algorithm

In order to fulfill the requirements for a trigger-less data acquisition system, the preamplifier signals will be continuously digitized by Sampling ADCs and the resulting data will be processed on-line by the feature-extraction algorithm in FPGA. For the hit-detection and the determination of energy and arrival time of the incoming events the feature-extraction algorithm has been developed in this work. The algorithm consists of different functions, such as Moving-Window Deconvolution (MWD) for pulse filtering, Moving Average (MA) for noise reduction and Constant Fraction Timing (CFT) for determination of the time stamp. The maximum of the MWD filtered signal provides the energy information; the zero-crossing of the bipolar constant fraction timing signal provides the time-stamp information.

The developed algorithm was verified by experiments with EMC prototypes [56]. The obtained results indicate that the EMC equipped with such electronics will fulfill the requirements for the physics program of the PANDA experiment. The feature-extraction

algorithm was applied for off-line data taken with Proto60, the prototype of the PANDA EMC. The experiment was performed with high-energy photons impinging on an array of 60 PWO crystals. The resulting energy and time resolutions are satisfying and are shown in Figure 4. The obtained energy resolution is 2.4(1)% for 1 GeV photon energy and the time resolution is less than 1.0(1) ns for an energy deposition above 100 MeV.

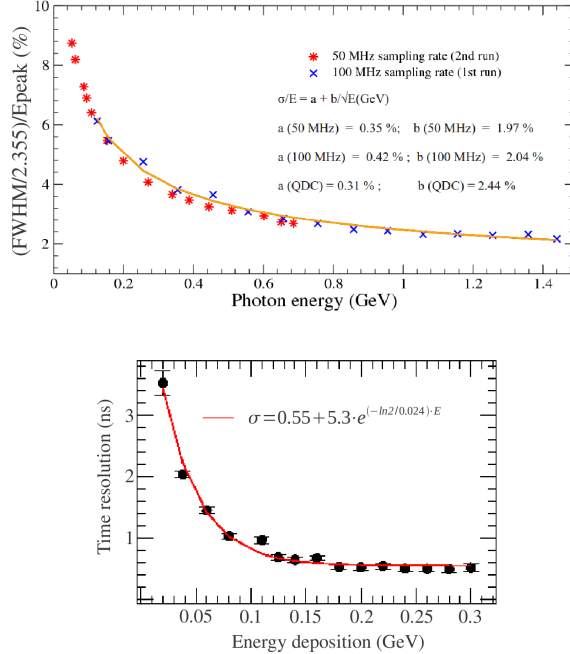


**Figure 4:** Top: The energy resolution for a  $3 \times 3$  array of PWO crystals as a function of the photon energy. Bottom: The time resolution for different energy depositions.

In addition, the developed digital shaping allows to shorten the hit response of the detector and, therefore, to reduce the pile-up probability.

### Performance test of the on-line feature-extraction

The developed feature-extraction algorithm was implemented in VHDL, the language used for FPGA programming. The test of the FPGA implementation for the on-line data analysis was done with an LED light pulser and for cosmic-muon energy depositions using a single-crystal test setup. The resulting values of energy and time resolutions for the on-line and off-line data analysis were compared. In both cases the analysis parameters, such as differentiation and integration for the digital filters, delay and fraction for CFT, were kept the same. The obtained correlation between the resulting values from off-line and on-line data processing was 99.9% (see Figure 5). The time resolution of 3.16(3) ns is measured using cosmic muons, which corresponds to 20 MeV energy deposition in the PWO crystal

and this result compares well with the resolution of 3.15(1) ns obtained by the software (off-line) analysis.

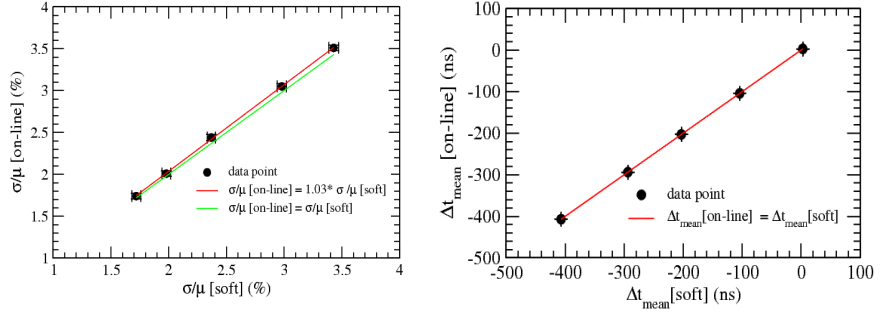


**Figure 5:** The comparison of the energy resolution  $\sigma/\mu$  (left) and timing performance  $\Delta t_{\text{mean}}$  (right) for the on-line and off-line (software) pulse processing. The correlation coefficient in both cases is 99.9%.

## Evaluation of PANDA EMC performance

The rich PANDA physics program aims particularly at precise hadron spectroscopy. The width of the reconstructed invariant mass of narrow resonances plays an important role for the interpretation of such states. To investigate how strong the influence of the readout electronics is on the performance of the detector, Monte Carlo simulations were performed for the  $h_c$  charmonium state. To validate the simulations, the response of a  $3 \times 3$  crystal array to a single photon with 200 MeV was investigated. The simulation results overlap rather well the experimental results obtained with the Proto60 setup.

After validating the simulation model, the  $h_c$  charmonium state was studied for different readout electronics noise, single crystal threshold and cluster threshold values. As an example, in Figure 6 the analysed width of the  $h_c$  charmonium state is given for different cluster thresholds. The width of the  $h_c$  charmonium state is getting larger at higher cluster thresholds. Additionally, we observe that the width is getting larger due to increasing noise in the readout electronics.

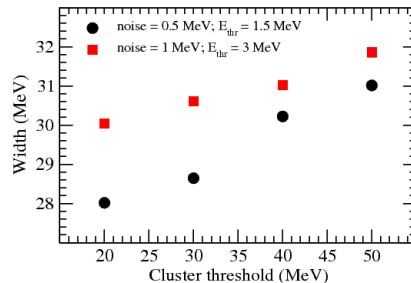


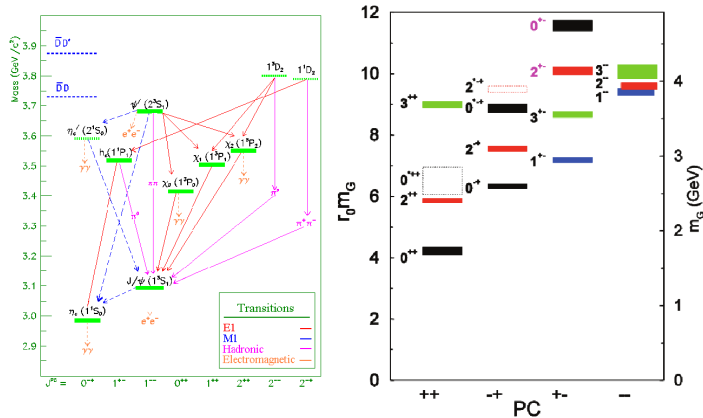
**Figure 6:** The width of the  $h_c$  charmonium state for different cluster thresholds.

The simulation study of the performance of the PANDA EMC has shown that the EMC has to have the best performance in terms of noise level and high-rate capability, in order to be able to study narrow resonances. The methods developed in this thesis thus lead to optimized performance of the detector system. They can also be applied in various other experimental situations where high rate capabilities are required.

## Samenvatting

Het Standaard Model van de deeltjesfysica is zeer succesvol gebleken in het identificeren van drie generaties van quarks, leptonen en verscheidene bosonen als de fundamentele en elementaire bouwstenen van materie. Het blijft een uitdagende puzzel om de onderliggende mechanismen te begrijpen die verantwoordelijk zijn voor de eigenschappen van hadronen, zoals protonen en neutronen, de bouwstenen van atoomkernen. Hadronen die charm quarks bevatten zijn veelbelovende laboratoria, die de geheimen kunnen onthullen van de sterke interactie op grote afstanden. Deze interactie is relevant voor de structuur van hadronen. Van groot interesse is het spectrum van charmonium, bestaande uit een charm  $c$  en een anti-charm  $\bar{c}$  quark, Nauwkeurige metingen van de massa, de breedte en vervaltakken van alle charmonium staten zullen informatie geven over de quark-beperkende potentiaal en zijn spin-afhankelijkheid (zie Figuur 1, linker paneel). De charmonium staten boven de  $D\bar{D}$  drempels zijn slecht onderzocht.

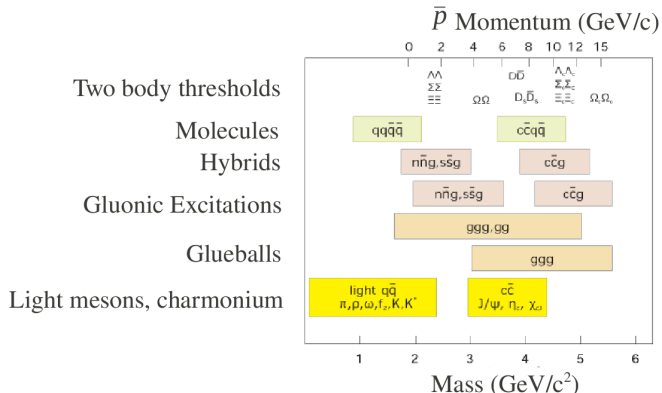
Berekeningen met de gediscretiseerde sterke interactie (QCD) op een ruimte-tijd rooster (LQCD) voorspellen de aanwezigheid van nog niet waargenomen samengestelde deeltjes, zoals “glueballs” (zie Figuur 1, rechter paneel). Lichte glueballs zijn experimenteel moeilijk te identificeren, omdat zij kunnen mengen met de gewone mesonen. Daarom zouden zware glueballs met exotische kwantumgetallen gemakkelijker op te sporen zijn.



**Figuur 1:** Links: Spectrum van charmonium staten en overgangen volgens de aangegeven legenda. Rechts: Voorspellingen uit LQCD berekeningen van de massa  $m_G$  van glueballs met verscheidene PC kwantumgetallen.

Om de sterke interactie in het niet-perturbatieve regime van QCD te bestuderen, is het PANDA experiment voor proton-antiproton annihilaties ontworpen. Met anti-proton bundels

in het impuls bereik van 1.5 tot 15 GeV/c, beschikbaar gesteld door FAIR Darmstadt, kunnen staten met exotische kwantum getallen worden aangeslagen, zoals voorspeld door LQCD. Het fysica programma van het PANDA experiment richt zich op charmonium spectroscopie en de zoektocht naar hybride-staten, dat zijn mesonen met charm quarks en een sterke gluon bijdrage, en glueballs (zie Figuur 2). Bovendien zal een grote verscheidenheid aan andere fysica onderwerpen [6], zoals de studie van hyperkernen, in het bijzonder die met twee hyperonen, en metingen van de tijdsachttige form factor van het proton worden bestudeerd.



**Figuur 2:** Massa bereik van hadronen die toegankelijk zullen zijn met het PANDA experiment. De bovenste schaal geeft de bijbehorende antiproton impulsen aan.

Het ruime fysica programma vereist een compact en multifunctioneel detectorsysteem met als hoofdcomponent een elektromagnetische calorimeter (EMC) met hoge resolutie. Dit proefschrift richt zich op het optimaliseren van de EMC voor de meest gevoelige studies bij een hoge frequentie van geobserveerde gebeurtenissen (events). Hoge precisie studies van zeldzame processen vereisen een snelle, complexe en veilige selectie van veelbelovende events. Daarom moet de uitleeselektronica, met bijbehorende logische componenten, in staat zijn, om in korte tijd gevoelige informatie te verstrekken, zoals de invariante massa van neutrale mesonen of de vertices van vervallende mesonen. De eerste en belangrijkste stadia van deze uitleeselektronica voor de PANDA EMC zijn ontwikkeld, getest en geëvalueerd in het kader van dit proefschrift.

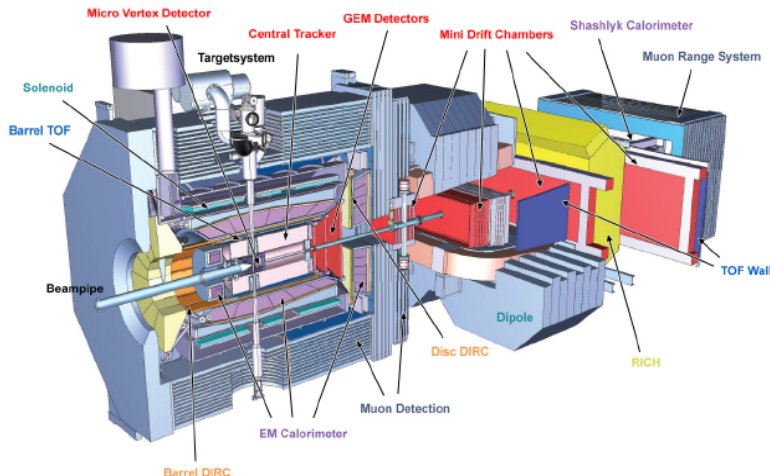
## PANDA Detector

De PANDA detector (Figuur 3) zal worden geïnstalleerd bij de High-Energy Storage Ring (HESR) van FAIR om verscheidene types deeltjes te detecteren na de annihilatie van anti-protonen. De detector moet functioneren bij hoge annihilatie frequenties tot en met  $2 \cdot 10^7$  annihilaties/s, zal goed in staat zijn om deeltjes te identificeren, een hoge impuls resolutie hebben, en moet uitstekend werken voor vertex reconstructie en hoge-resolutie calorimetrie. Bovendien zal een nieuwe aanpak voor de event selectie worden gebruikt, om de efficiëntie en de kwaliteit van de dataverzameling te verhogen. Alle detectorkanalen

zullen namelijk in “free-running” mode opereren waarbij een goede tijdsmarkering de data-events gaan bepalen die alle nodige informatie bevatten. Deze informatie zal worden gebruikt voor de selectie van events op basis van de fysica eigenschappen van de deeltjes, zoals de gereconstrueerde invariante massa of een gedetecteerde secundaire vertex. Deze aanpak wordt een “triggerloze data-acquisitie” genoemd [28].

## Calorimetrie voor de PANDA detector

Een cruciaal onderdeel van de PANDA detector is de elektromagnetische calorimeter (EMC). De EMC zal hoog-energetische elektronen, positronen en fotonen in de eindstaat detecteren met een hoge tijds- en energieresolutie en in een groot dynamisch energiebereik van 10 MeV tot 10 GeV. De EMC is ontworpen om een vrijwel  $4\pi$  bedekking te bereiken in de target spectrometer (zie Figuur 3). Voor hoge annihilatie frequentie is calorimetrie met een snelle respons vereist. Aan de andere kant vereist precisie-spectroscopie een hoge granulariteit van de calorimeter. Voor dit doel is het PbWO<sub>4</sub> (PWO) materiaal gekozen om de calorimeter te bouwen. De plaatsing van de detector in een hoog 2 T magnetisch veld verhindert het gebruik van fotomultiplicator buizen als lichtsensoren. Daarom zullen avalanche fotodiodes met een groot oppervlak worden ingezet. De EMC zal worden gebruikt bij een temperatuur van -25 °C om de lichtopbrengst van PWO kristallen te verhogen en de EMC prestatie te verbeteren.



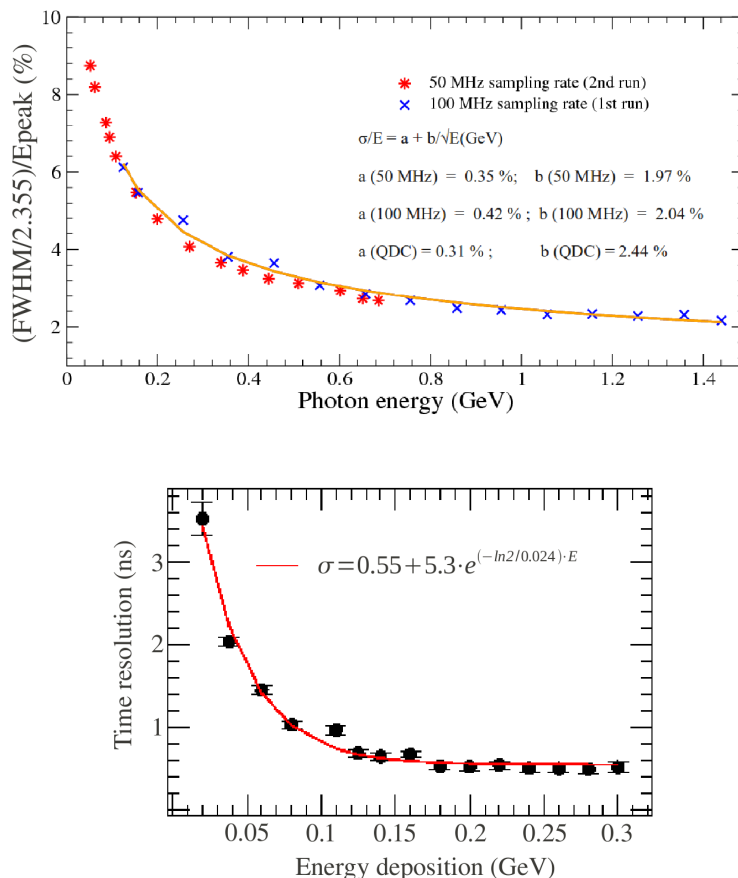
**Figuur 3:** De Target Spectrometer (linker deel) en de Voorwaartse Spectrometer (rechter deel) van de PANDA detector. De verscheidene sub-detector componenten zijn aangegeven.

## Feature-extraction algoritme

Om aan de vereisten van een triggerloos data-acquisitie systeem te voldoen, zullen de voorversterkersignalen continu worden gedigitaliseerd door sampling ADC's en de resulterende data on-line worden verwerkt door een feature-extraction algoritme in een

FPGA: dat is een flexibele processor voor on-line data bewerkingen. Voor de hit-detectie en de bepaling van de energie en aankomsttijd van de inkomende events is het feature extractie algoritme ontwikkeld in dit proefschrift. Het algoritme bestaat uit verschillende functies, zoals Moving-Window Deconvolution (MWD) voor puls filtering, Moving Average (MA) voor ruisreductie en Constant Fraction Timing (CFT) voor de bepaling van het tijdstoemoment van een gemeten signaal.

Het ontwikkelde algoritme werd geverifieerd door experimenten met EMC prototypes [56]. De verkregen resultaten geven aan, dat de EMC, uitgerust met dergelijke elektronica en logica, aan de eisen van het fysica programma van het PANDA experiment zal voldoen. Het feature-extractie algoritme werd toegepast voor de off-line data genomen met Proto60, het prototype van de PANDA EMC. Het experiment werd uitgevoerd met hoog-energetische fotonen vallend op een reeks van 60 PWO kristallen. De resulterende energie- en tijdsresoluties voldoen aan de vereisten en zijn weergegeven in Figuur 4. De verkregen energie resolutie is 2.4(1)% voor een fotonenergie van 1 GeV en de tijdsresolutie is minder dan 1.0(1) ns voor een energieafgifte boven de 100 MeV. Daarnaast maakt de ontwikkelde digitale shaping procedure het mogelijk om de hit-respons van de detector te verkleinen. De resulterende kortere signalen verminderen de kans op overlappende pulsen (pile-up).

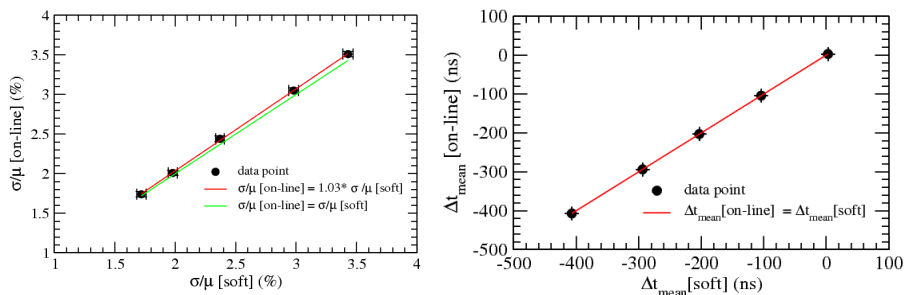


**Figuur 4:** Boven: De energieresolutie voor een  $3 \times 3$  matrix van PWO kristallen als functie van de fotonenergie. Onder: De tijdsresolutie voor verschillende energieafgiftes.

## Performance test van de on-line feature-extractie

Het ontwikkelde feature-extractie algoritme werd geïmplementeerd in VHDL, de taal die wordt gebruikt voor het programmeren van de FPGA. De test van de FPGA implementatie voor de on-line data-analyse werd uitgevoerd met licht signalen van een LED pulser en voor energieafgiftes door kosmische muonen. Hiervoor werd een testopstelling met een enkelvoudig kristal gebruikt.

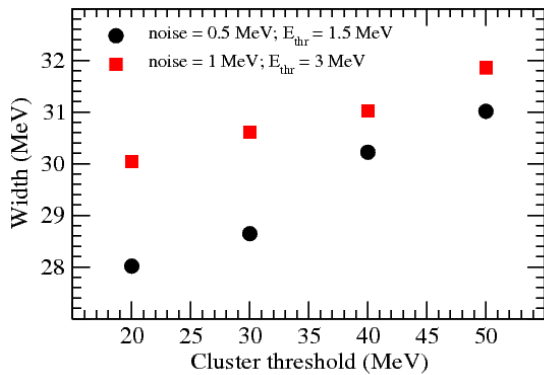
De resulterende waarden van de energie- en tijdsresoluties voor de on-line en off-line data-analyse werden vergeleken. In beide gevallen werden de analyseparameters, zoals de differentiatie en integratie van de digitale filters, vertraging en CFT fractie, constant gehouden. De verkregen correlatie tussen de resulterende waarden van de off-line en on-line dataverwerking was 99.9% (zie Figuur 5). De tijdsresolutie van 3.16(3) ns werd gemeten met kosmische muonen, corresponderend met 20 MeV energiedepositie in het PWO kristal, en dit resultaat komt goed overeen met het resultaat verkregen door de software (off-line) analyse van 3.15(1) ns.



**Figuur 5:** De resultaten voor energieresolutie  $\sigma/\mu$  (links) en tijdsprestatie  $\Delta t_{mean}$  (rechts) zijn met elkaar vergeleken voor de twee manieren van pulsverwerking: on-line (in de FPGA) en off-line (via software). De correlatiecoëfficiënt is in beide gevallen 99.9%.

## Evaluatie van de PANDA EMC-prestaties

Het rijke PANDA fysica programma is voornamelijk gericht op nauwkeurige hadron spectroscopie. De breedte van de gereconstrueerde invariante massa van smalle resonanties is een belangrijke factor voor de interpretatie van dergelijke staten. Om te onderzoeken hoe sterk de invloed van de uitleeselektronica is op de prestaties van de detector, werden Monte Carlo simulaties uitgevoerd voor de  $h_c$  charmonium staat. De kwaliteit van de simulaties werd getoetst door de respons van een  $3 \times 3$  kristal reeks op een enkel foton van 200 MeV te onderzoeken. De simulatieresultaten overlappen vrij goed met de experimentele resultaten verkregen met de Proto60 setup. Vervolgens werd de  $h_c$  charmonium staat onderzocht voor verschillende niveaus van elektronische ruis, enkelvoudige kristal drempels en cluster drempelwaardes. Als voorbeeld staat in Figuur 6 de onderzochte breedte van de  $h_c$  charmonium staat aangegeven voor de verschillende cluster drempels. De breedte van de  $h_c$  charmonium staat wordt significant groter bij hogere cluster drempels evenals door de toenemende ruis in de uitleeselektronica.



**Figuur 6:** De breedte van de  $h_c$  charmonium staat voor verschillende cluster drempels.

De simulatiestudie van de prestatie van de PANDA EMC heeft aangetoond dat maximale prestaties vereist zijn op het gebied van ruisniveau en snelle signaal verwerking, om smalle resonanties efficiënt te kunnen bestuderen. De in dit proefschrift ontwikkelde methoden zullen dus bijdragen tot optimale prestaties van het gehele PANDA detectorsysteem. Bovendien kunnen de voorgestelde methoden in verscheidene andere experimentele situaties, waar een hoog ruisniveau aanwezig is en hoge signaal frequenties vereist zijn, zeer voordelig toegepast worden. Mogelijke toepassingen worden door een commercieel bedrijf en andere experimentele groepen al bestudeerd.

---

## Acknowledgment

I would like to express my gratitude to all the persons who have made the completion of my PhD work possible.

First, I would like to thank my promotor Prof. H. Löhner for inviting me to the KVI and making it possible for me to do research in the field of Hadron Physics. I learned a lot from you. I will always remember your kind support, valuable suggestions, careful reading, and thorough corrections during my thesis writing.

I am very thankful to my supervisor Dr. M. Kavatsyuk for making things easy during my work. I will never forget your efforts in making me a skilled researcher. I will remember the way you taught me the basic steps of programming, to work with electronics, and to do data analysis. I have always enjoyed your company during our travels to Germany.

Also, I would like to thank Dr. J. Messchendorp for his advice during the PandaRoot simulations, which helped me to end up with a reasonable result in such a short period of time. I enjoyed your subatomic physics course.

My special thanks go to electronic engineer P.J.J. Lemmens for many valuable discussions during the VHDL implementation in the FPGA of the Struck SADC.

I am very thankful to the Giessen group members for all their support during the Proto60 beam time at Mainz. Specially, I thank Dr. V. Dormenov for his guidance to do simulations in GEANT.

My special thanks go to Ganesh, Ali and Qader for all kind of discussions and to Ruud for his help in preparing the Nederlandse samenvatting. For making my stay warm at KVI, I would like to thank all the personnel, engineers, PhD students and staff. Because of your very kind hospitality and the very nice relationships I enjoyed working at KVI. Thank you very much to all of you.

I would like to thank, the members of the reading committee for their valuable time they spent reading my thesis and giving me important comments.

I would like to thank my uncle Yusif and my wife Ravana for all their support and understanding during the past four years.

---